Titre: Title:	Forward and Inverse Modelling of Magnetic Induction Tomography (MIT) for Biomedical Application
Auteur: Author:	Amir Ahmad Roohi Noozadi
Date:	2017
Type:	Mémoire ou thèse / Dissertation or Thesis
Référence: Citation:	Roohi Noozadi, A. A. (2017). Forward and Inverse Modelling of Magnetic Induction Tomography (MIT) for Biomedical Application [Thèse de doctorat, École Polytechnique de Montréal]. PolyPublie. https://publications.polymtl.ca/2536/

UNIVERSITÉ DE MONTRÉAL

FORWARD AND INVERSE MODELLING OF MAGNETIC INDUCTION TOMOGRAPHY (MIT) FOR BIOMEDICAL APPLICATION

AMIR AHMAD ROOHI NOOZADI
DÉPARTEMENT DE GÉNIE PHYSIQUE
ÉCOLE POLYTECHNIQUE DE MONTRÉAL

THÈSE PRÉSENTÉE EN VUE DE L'OBTENTION
DU DIPLÔME DE PHILOSOPHIÆ DOCTOR
(GÉNIE PHYSIQUE)
MARS 2017

UNIVERSITÉ DE MONTRÉAL

ÉCOLE POLYTECHNIQUE DE MONTRÉAL

Cette thèse intitulée :

FORWARD AND INVERSE MODELLING OF MAGNETIC INDUCTION TOMOGRAPHY (MIT) FOR BIOMEDICAL APPLICATION

présentée par : ROOHI NOOZADI Amir Ahmad
en vue de l'obtention du diplôme de : Philosophiæ Doctor
a été dûment acceptée par le jury d'examen constitué de :

M. FRANCOEUR Sébastien, Ph. D., président
M. YELON Arthur, Ph. D., membre et directeur de recherche
M. MÉNARD David, Ph. D., membre et codirecteur de recherche
M. LEBLOND Frédéric, Ph. D., membre
M. ADLER Andy, P. Eng., membre externe

DEDICATION

To my Mom, Dad and My dearest Ely

ACKNOWLEDGMENT

I would like to thank my advisers, Arthur Yelon and David Ménard, for their consistent support and inspiration. It was a pleasure working with these two brilliant scientists.

I would also like to thank Hervé Gagnon for fruitful discussions, technical consultant and helpful suggestions. Hervé expertise had a noticeable effect on the progress rate of this research.
I thank the members of the jury Sébastien Francoeur, Frédéric Leblond, and Andy Adler for evaluating this thesis and for their constructive comments.
I would like to thank my former supervisors Reza Jafari and Shahram Jalalzadeh for their supports and fruitful discussions since I started studying physics till the day this thesis was submitted.

I thank all my colleagues and friends, especially Nima Nateghi, Saeed Bohloul,
Mehran Yazdizadeh, Antoine Morin, Nicolas Teyssedo, Sahar Fazeli and Saman Choubak, for their support and helpful discussions.

And finally I thanks my wonderful Mom, Dad, and my sister Ely for their continuous support and endless love.

RÉSUMÉ

Cette thèse développe un outil de simulation destiné au design d'instruments de tomographie par induction magnétique (MIT pour Magnetic Induction Tomography). Ce simulateur permet d'investiguer la possibilité d'utiliser la méthode d'imagerie par tomographie par induction magnétique afin de faire la conception d'un dispositif sans-contact capable de détecter une hémorragie à l'intérieur du crâne humain. La méthode spécifique de calcul numérique utilisée pour la simulation du dispositif de même que le calcul de la sensibilité avec la méthode directe (introduite dans cette thèse) et la résolution du problème inverse, qui reconstruit une carte de la conductivité à partir des résultats de simulation, sont optimisés afin de simuler un dispositif opérant à 50 kHz. Ce dispositif est capable de détecter le changement de la conductivité dans une gamme se rapprochant de celle des tissus biologiques.

Le fonctionnement de base de la tomographie par induction magnétique repose sur les mesures des propriétés électromagnétiques dites passives telles que la conductivité. L'utilisation d'une telle méthode pour détecter les hémorragies cérébrales se justifie par le fait que la conductivité du sang est plus élevée que la conductivité des autres tissus constituant le cerveau. Une autre application potentielle de cette méthode est le suivi en temps réel, de manière non invasive, de l'altération des tissus qui peut s'observer à partir d'un changement de conductivité, par exemple les problèmes respiratoires, la guérison de plaies ainsi que les processus ischémiques.

Les bobines d'induction dans le dispositif de tomographie par induction magnétique produisent un champ magnétique primaire dans la région d'intérêt (ROI pour Region of Interest) et ce champ alternatif induit des courants alternatifs (courants de Foucault) dans les régions conductrices. Ces courants induits produisent à leur tour un champ magnétique secondaire dans la région d'intérêt. Ce champ magnétique secondaire produit un champ aux bobines de réception qui est utilisé pour reconstruire la distribution de la conductivité dans la région d'intérêt.

Un défi important concernant l'état de l'art de ces dispositifs est la détection du signal secondaire en présence du signal primaire, qui est plusieurs ordres de grandeur plus fort. Le dispositif présenté utilise une géométrie pour l'induction et la détection spécialement conçue pour opérer dans les basses fréquences avec un ratio signal sur bruit acceptable de même qu'une configuration du détecteur qui est moins sensible au champ primaire. La méthode directe du calcul de la matrice de sensibilité introduite dans cette thèse nous fournit une méthode numérique robuste pour la reconstruction d'images, ce qui résulte en une qualité d'image supérieure par rapport aux autres méthodes proposées dans la littérature.

Les configurations du système que nous présentons impliquent une forme cylindrique avec

6 bobines d'excitation concentriques qui sont placées à différentes hauteurs sur la surface externe. Ces bobines produisent un signal primaire dont la majorité des lignes de champ sont parallèles à l'axe principal du cylindre où est placé l'objet d'intérêt. Ce champ induit alors des courants de Foucault (courants de conduction et courants de déplacement) dans les régions conductrices, ce qui génère un champ magnétique secondaire. Ce champ secondaire est détecté par 80 bobines de réception (16 rangées de détecteurs placés à 5 hauteurs différentes) qui sont placées sur les parois du cylindre de manière perpendiculaire au plan des bobines d'excitation.

La simulation de ce dispositif nécessite un modèle mathématique comprenant le problème direct et le problème inverse. Le problème direct est la simulation mathématique du système, qui résout les équations de Maxwell dans la région d'intérêt avec les conditions frontière adéquates.

Le problème impliquant les courants de Foucault est résolu par l'utilisation d'un modèle connu sous le nom d'équations de Maxwell complètes (traduction libre de full Maxwell's equations). Ce problème est résolu par la méthode des éléments finis (éléments en périphérie, traduction libre de edge elements) en considérant les fonctions de Whitney de premier ordre. Le modèle est comparé à des solutions analytiques connues pour des géométries simples. Le problème direct nous permet d'obtenir l'amplitude des champs magnétiques et électriques qui sont détectables, la distribution et l'ordre de grandeur des courants de Foucault ainsi que le changement de phase du champ magnétique détecté qui est causé par la partie conductrice de la région d'intérêt.

À partir du problème direct, la matrice de sensibilité peut être extraite, ce qui est nécessaire afin de résoudre le problème inverse. Les méthodes disponibles pour extraire la matrice de sensibilité, par exemple le théorème de réciprocité de Geselowitz, sont généralement des formulations indépendantes du problème direct considéré. Cependant, pour notre modèle, la sensibilité est calculée directement par la différentiation numérique de l'équation d'Helmholtz par rapport aux propriétés électriques. Cette méthode pour calculer la matrice de sensibilité (la méthode directe) est introduite dans cette thèse et les résultats de la reconstruction pour cette méthode sont comparés avec ceux provenant du théorème de réciprocité appliqué aux problèmes de tomographie par induction magnétique. La matrice de sensibilité peut révéler à quel point la sensibilité d'une partie de la région d'intérêt peut être affectée par un changement quelconque de courant ou de conductivité (de même que pour d'autres propriétés). De plus, extraire la matrice de sensibilité permet de calculer la direction de sensibilité maximale à un changement de conductivité dans une certaine partie de la région d'intérêt, ce qui permet de déterminer le meilleur arrangement et emplacement des détecteurs. L'extraction de la matrice de sensibilité par la méthode directe, à partir des outils permettant de résoudre

ce modèle, n'est pas une tâche simple. Ainsi, le modèle direct doit être développé dans son entièreté dans MATLAB.

Le problème inverse (la description de la structure interne du système fournie par des données indirectes) est ensuite résolu à l'aide de la matrice de sensibilité et des méthodes disponibles dans la littérature (ces méthodes sont courantes pour la tomographie par impédance électrique). Pour le problème inverse, résolu par la méthode du maximum a posteriori, les approches linéaires et non linéaires ont été utilisées afin de reconstruire la conductivité. L'approche linéaire est prometteuse pour l'imagerie différentielle afin de confirmer l'apparition d'une lésion si nous disposons au préalable d'informations concernant la conductivité normale de la tête et du crâne. Cependant, l'approche linéaire amène à des valeurs erronées de la conductivité. L'approche non linéaire a également été implémentée afin de permettre le calcul de la valeur absolue de la conductivité sans aucune information préalable. Toutefois, l'approche non linéaire est coûteuse au point de vue des ressources computationnelles et donc faire la tomographie par induction magnétique en utilisant notre méthode n'est pas envisageable pour calculer la valeur absolue de la conductivité.

La configuration des senseurs adoptée pour notre dispositif, dont le positionnement des capteurs est perpendiculaire aux bobines d'excitation, amène un avantage au point de vue de la soustraction du champ primaire, ce qui est un défi constant dans l'opération des autres dispositifs de ce type. Les signaux ont été simulés pour différentes hauteurs de disque dans le cylindre et différentes locations de la lésion à l'intérieur du disque. La distribution de la conductivité est ensuite reconstruite à partir du changement de voltage induit dans les senseurs.

Les résultats du problème de reconstruction concernant le modèle du disque dans le dispositif proposé, en considérant que le niveau de bruit est constant et vaut 1% du signal maximal détecté, montrent un ratio de signal sur bruit de 40 dB. Les capteurs magnétiques utilisés pour construire ce dispositif devraient être capables de détecter des champs de 10 pT avec ce même ratio signal sur bruit.

ABSTRACT

This thesis develops a simulation package for the design of Magnetic Induction Tomography (MIT) instruments and exploit the simulator to investigate the possibility of using the magnetic induction tomography imaging method to design a non-contact device capable of detecting a blood hemorrhage inside the skull. The specific numerical method (full Maxwell's equation) used for simulation of the device, followed by calculation of the sensitivity with the direct method (introduced in this dissertation) and a regularized inverse solver which reconstruct the conductivity map from the simulation outputs (magnetic field), are optimized to simulate a device operating at 50 kHz. This device is capable of detecting the change in conductivity in ranges close to biological tissues.

MIT operates based on the measurement of passive electromagnetic properties such as conductivity. The rationale behind using this method for detecting cerebral stroke is based on the fact that the conductivity of the blood is larger than that of the other tissues in the head. Other potential medical applications for this device are real-time, non-invasive monitoring of tissue alterations which are reflected in the change of the conductivity, e.g. ventilation disorders, wound healing and ischemic processes.

The inductive coils in the MIT device produce a primary magnetic field in the region of interest (ROI) and this alternating magnetic field induces alternating (eddy) currents in the conductive regions. These eddy currents, in turn, generate a secondary magnetic field in the ROI. This secondary magnetic field generates a field at the receivers, which is used to reconstruct the conductivity distribution of the ROI.

An important challenge in the state of art devices is the detection of the secondary signal in the presence of the primary signal, which is orders of magnitude stronger. The device uses a geometry in induction and detection designed to operate in low frequencies with acceptable SNR and detector configuration that is least sensitive to the primary field. The direct method of calculating the sensitivity matrix introduced in this thesis provides us with a robust numerical method for image reconstruction which results in superior image quality compared to other proposed methods in the state of the art.

The proposed configurations involves a cylindrical shape device with 6 concentric excitation coils which are located at different heights on the outer surface of the cylinder. These coils produce a primary magnetic field with majority of the field lines parallel to the main axis of the cylinder, where we position the object of interest. This primary field induces eddy currents (conduction and displacement current) in the conductive regions of the ROI, which generate a secondary magnetic field. The secondary magnetic field is detected in 80 sensors

(16 arrays of sensors at 5 different heights), which are located on the cylinder walls perpendicular to the plane of excitation coils.

The simulation of this device requires a mathematical model consisting of a forward and an Inverse problem. The forward problem is the mathematical simulation of the device, which solves Maxwell's equations in the ROI with the appropriate boundary conditions.

The problem is known as the eddy current problem is solved using a model known as *full Maxwell's equations*. The eddy current problem is solved using a finite element method (edge basis) considering the first order Whitney functions. The model is bench-marked with available analytic solutions for known geometries. The forward problem provides us with the magnitude and direction of the detectable magnetic and electric field, eddy current size and distribution and also the phase change in the detected magnetic field, which is caused by the conductive area in the ROI.

From the forward problem, the sensitivity matrix is extracted that is used in solving the reconstruction problem. Methods available for extracting the sensitivity matrix, like using the Geselowitz reciprocity theorem, are mainly independent formulations regardless of the method used in solving forward problem. However, in our model, the sensitivity is directly calculated by the rigorous numerical differentiation of the governing equation (Helmholtz) in the forward problem, with respect to the electrical properties. This method of calculating the sensitivity matrix (the direct method) is introduced in this thesis and the results of reconstruction for this method are compared with results from the reciprocity theorem. The sensitivity matrix shows how sensitive is the secondary field of an area in ROI to any change in current or conductivity of other areas (as well as other properties such as permittivity). Furthermore, extracting the sensitivity matrix could allows one to systematically investigate the most sensitive direction to the conductivity change in certain area, at any position in the region of interest to find the the best arrangement and alignment for the sensors. Extracting the sensitivity matrix with the direct method, from available packages which are capable of solving the forward model, is not a straightforward task. Therefore, the forward model is fully developed in MATLAB.

The inverse problem (the description of the internal structure of a system given by indirect data) is then solved using the sensitivity matrix and available methods known for solving inverse problems in the literature (These matrix inversion methods are common with Electrical Impedance Tomography). In the inverse problem, which is solved using the *maximum a posterior method*, both the linear and non-linear approach were taken to reconstruct conductivity. The linear approach is promising for differential imaging performed on a head modelled as a disk with different conductivity layers to confirm the appearance of the lesion, if we have prior information about the conductivity of the background (the head and the

skull). However, the linear method will produce an inaccurate conductivity values. The non-linear approach has also been implemented to calculate the absolute value of the conductivity without prior information. However, the non-linear method is not computationally cost-wise and therefore performing Magnetic Induction Tomography with using the method is not suitable for calculating the absolute value of the conductivity.

The configuration of the sensors adopted in this device, which is positioning the receivers perpendicular to the excitation coils, makes it advantage in subtraction of the primary signal which has been a main challenge in operation of such devices. The signals were simulated for different height of the disk in the cylinder and different locations of the lesion in the disk model. The conductivity distribution is then reconstructed from the corresponding voltage changes induced in the sensors.

The results of the reconstruction problem performed on the disk model using the proposed device for a constant noise level, which is considered to be 1% of the maximum detected signal, shows a SNR of 40 dB. Magnetic sensors used for building this device should be able to detect 10 pT fields at this SNR.

TABLE OF CONTENTS

LIST OF TABLES

LIST OF FIGURES

LIST OF APPENDICES

NOMENCLATURE

Abreviations

EIT	Electrical impedance tomography
ECT	Electrical capacitance tomography
MIT	Magnetic induction tomography
ROI	Region of interest
MRI	Magnetic resonance imaging
CT	Computerized (or computed) Tomography
SNR	signal-to-noise ratio
FEM	Finite element method
BC	Boundary condition
PDE	Partial differential equation
NOSER	Newton-one-step reconstructor
TSVD	truncated singular value decomposition
VU	variance uniformization
MLE	Maximum likelihood estimation
MAP	Maximum a posteriori estimation
RAM	Random access memory
SAR	Signal Absorption Rate

Symbols

V	Voltage, Electrical potential
I	Applied current
V_i	Volume
σ	Conductivity
μ	Permeability
ϵ	Permittivity
σ_0	Conductivity of free space
μ_0	Permeability of free space
ϵ_0	Permittivity of free space
ω	Angular frequency
$\mathbf{A}$	Magnetic vector potential
W_m	Whitney function (weighting function)
e_m	Edge vectors

α_{ti}	Simplex coordinates
L_m	Edge lengths
$a_{ti}, b_{ti}, c_{ti}, d_{ti}$	Cofactors
A_{xm}, B_{xm}, C_{xm}	Whitney function coefficient
$\mathbf{D}$	Electrical displacement
$\mathbf{B}$	Magnetic field
$\mathbf{E}$	Electrical field
$\mathbf{H}$	The auxiliary field
J, J_s	Current density
ρ	Charge density
δ	Skin depth
Z_{el}, T_{el}, J_{el}	Structural matrices for each element
$\mathbf{J}$	The global current density matrix
$\mathbf{Z}$	The global structural matrix
$\mathbf{T}$	The global structural matrix
$\mathbf{e}$	The global edge matrix
$\mathbf{S}, \mathbf{S}_\sigma$	Sensitivity matrix (direct method)
$\mathbf{GS}_\sigma$	Sensitivity matrix (Geselowitz)
$\mathbf{S}_{\sigma\mathbf{B}}, \mathbf{S}_{\sigma V}$	Sensitivity matrix (wrt $\mathbf{B}$ or V)
$\mathbf{I}$	Identity matrix
λ	Regularization parameter

CHAPTER 1 INTRODUCTION

Prelude

The fundamental laws necessary for the mathematical treatment of a large part of physics and the whole of chemistry are thus completely known, and the difficulty lies only in the fact that application of these laws leads to equations that are too complex to be solved.

Paul Dirac

1.1 Introduction to tomographic impedance techniques

Tomographic techniques for imaging passive electromagnetic properties such as conductivity, permittivity and permeability of materials have been active research fields over recent decades. The oldest of these techniques, Electrical Impedance Tomography (EIT) involves a series of contact electrodes for injecting the currents in a region of interest (ROI) and detecting the resulted voltage (Adler et Guardo, 1996). Pairs of electrodes, in different configurations, are used to excite a current inside the conductive medium and other pairs are used to detect the voltages. The voltages are used for the determination of the conductivity and permittivity values of the medium. The EIT image reconstruction problem can be modelled by numerical treatment of the Laplace equation (Kobylianskii *et al.*, 2016). Dynamic EIT (the measurement of conductivity change) has been suggested because of its increased sensitivity and the ability to compensate unknowns. Dynamic EIT may be applied in studying the physiological process which modify the electrical conductivity of biological tissue (Adler *et al.*, 1998).

Another technique is known as Electrical Capacitance Tomography (ECT) (Yang et Peng, 2002). It is very similar to EIT, but it measures the resulting capacitance. This technique is suggested for imaging of materials with low permittivity and negligible conductivity.
The most recent of the tomographic techniques, Magnetic Induction Tomography (MIT), is a non-invasive imaging technique, which is sensitive to all passive electromagnetic properties, such as conductivity, permittivity and permeability of the ROI (Holder, 2004 ; Soleimani et Lionheart, 2006 ; Merwa *et al.*, 2004). This imaging technique requires a combination of coils for inducing eddy currents in the ROI and magnetic field sensors for recording their responses. In contrast with EIT, which requires electrodes contacting on the object of interest, the measurement of magnetic field is contactless, and therefore it is more advantages to the EIT

techniques. In addition, MIT can be performed to reconstruct the conductivity of a medium within insulating boundaries (brain within the skull) in contrast to EIT which is not plausible for such applications, as contact electrodes can not inject currents inside the medium (Brown, 2009).

In a MIT imaging device, excitation coils are used to induce alternating magnetic field inside the ROI. This magnetic field will produce currents in conductive areas inside the ROI, which produce secondary magnetic field detectable at sensors. The pattern and size of the detected secondary field for various excitation patterns is used to measure the absolute or differential value of conductivity in the ROI. In most MIT setups reported so far, the field is measured inductively using the same coils used for excitation. The basics of extracting the conductivity map from electrical measurements and its resolution is discussed in Appendix (A).

Industrial interest in this type of non-invasive imaging method includes applications in control or visualization of pipelines (Griffiths, 2001 ; Borcea, 2002). More recent interests are applications of this method in medical monitoring areas, where EIT or MIT devices are used to take a cross sectional images of properties of human body tissues (Wei *et al.*, 2012). The fact that MIT devices have lower design and operational cost compared with other imaging techniques, such as Magnetic Resonance Imaging (MRI) and Computerized (or computed) Tomography (CT scan), makes this technique an attractive alternative (Griffiths, 2001).

In addition, MIT devices are capable of real time imaging, which makes them good candidates for medical monitoring purposes, as this task is associated with measuring the change in properties of the biological tissues rather than their absolute measured values. After finding the sensitivity matrix of the device, the image is reconstructed with a matrix multiplication which does not require considerable amount of time.
Potential medical applications usually aim at the characterization of biological tissues by means of detection of a change in their complex conductivity. The motivation for measuring the electrical properties is their characteristic dependence on the (patho-) physiological state of tissues, especially hydration and membrane disorders. Medical applications so far suggested include imaging of limbs or of the brain, e.g. for the monitoring of brain edema, measurement of human body composition, and monitoring of wound healing (Griffiths, 2001 ; Holder, 2004).

The possibility of using a MIT device as a tool for diagnosis rather than monitoring has not yet been verified and is still a subject of active research with multi-frequency MIT devices. In the state of the art MIT devices, this imaging technique has not produced images

with sufficient resolution for diagnoses (Rosell-Ferrer *et al.*, 2006). However, in principle non-linear calculations may be done to reconstruct the absolute conductivity values, from the detected field with a MIT device (although with a high computational cost).
There are still challenges in magnetic tomographic measurements, such as finding an efficient method for subtraction of the primary magnetic field in the sensors to enhance the detection of the secondary field. Also, the low density of eddy currents in the ROI specially at the center, which is farther from the induction coils, result in low secondary magnetic field in those regions. These challenges have been addressed but not overcame in the state of art MIT which will be discussed in Chapter (2).
Furthermore, Biomedical MIT is constraint by the low absolute value of the conductivity of biological tissues, which produces very small secondary magnetic field compared to the primary applied field. In order to make this secondary magnetic field stronger and relatively easier to detect, as this field inductively detected by coils is proportional to the square of frequency, most biomedical MIT devices in the state of the art are proposed to operate in MHz frequency. However, such devices have not been applied in practice, as their performance is limited by crosstalk, since the secondary magnetic field signal produced at MHz by the tissue falls below the noise level. This noise is largely due to the capacitive crosstalks of the electronics operating in MHz frequency. This practical problem has not been addressed in the state of the art of MIT and a resolution for it is addressed in this dissertation by investigation of the feasibility performing the imaging in radio frequency regime. It is also worth mentioning that recent progress in giant magneto impedance sensors (Dufay *et al.*, 2013a), offering the possibility of vector magnetometery with much higher spatial resolution and significantly less crosstalk than inductive coils, have not yet been explored for MIT.

1.2 Objectives

The general objective of this dissertation is to develop a general platform that calculates the secondary magnetic fields for any given configuration of currents and electrical properties of the ROI. Therefore the governing equations (Helmholtz) of such platform will not consider any simplifications and can be used to investigate any MIT design. The platform will also be able to reconstruct the conductivity map of ROI using the value of the secondary magnetic field at the sensors. More specifically, I will :

1. *Develop the general solution to the forward Helmholtz equation and implement it in a numerical package.*

In order to calculate the magnitude of the secondary magnetic field produced by the conductive area in the ROI at the sensors, in other words simulation of this device performance, we solve the Helmholtz boundary value problem Eq.(3.15). The answer to the Helmholtz equation is the primary and the secondary magnetic vector potential given all the currents and the electrical properties everywhere in the ROI. The answer to this boundary value problem is unique for every device given the specifications of the induction currents position and properties of the medium. The magnitude of secondary magnetic field at the operation frequency of the device is useful in terms of specification of the required sensors. As previous devices suffer for capacitive crosstalks of the electronics operating high frequency, we try to lower the frequency provided the secondary magnetic field signal is still large enough for detection.
Commercial solvers are available capable of this task. However, our second objective requires the formulation to be fully developed. We have developed the formulation in MATLAB to tackle the numerical calculations.

2. *Calculate the Jacobian matrix using the direct method by variational formulation of the Helmholtz equation.*
We reconstruct the conductivity map of ROI using the secondary magnetic field calculated with finite element solver. In order to do so, we have to address the inverse Helmholtz equation which is, given the magnetic potential everywhere in the ROI, what is the conductivity distribution of the medium. The inverse Helmholtz equation in MIT, like the inverse Poisson equation in EIT, usually involves finding the Jacobian matrix of the system. The Jacobian matrix of any system is a measure of sensitivity of the solutions of the differential equation to the change of the the equation parameters. Then the inverse Helmholtz problem for finding the distribution of parameter (conductivity) is solved by finding the inverse of the Jacobian matrix. Therefore, calculating a more accurate Jacobian matrix provides us with more accurate calibration of the device. The detected magnetic field is converted to the conductivity map by a matrix multiplication of the values with the inverse of Jacobian matrix.
There exist several methods in calculating the Jacobian matrix of this device which are discussed in following section. We implement the direct method for calculation of the Jacobian matrix, which involves direct differentiation of the Helmholtz equation for discrete values. This method has not been used in MIT. As the performance of any linearized model depends on the accuracy of the of the linear modeling, we show that the direct method of sensitivity calculation improves the overall performance in reconstruction (less artifacts). There are more advantages in using the direct method

for calculation of the Jacobian which will be discussed in Chapter (6).

3. *Reconstruct the conductivity map of the ROI using the detected field at the sensors.*
   Once the Jacobian matrix is calculated, we have to find the inverse of this matrix to calculate the conductivity map. The Jacobian matrix calculated with any method suffers from the fact that the inverse Helmholtz equation is ill-posed. That is when the conductivity of a certain region in the space is altered, the alteration of secondary magnetic field is not considerable. In mathematical terms, the Jacobian matrix has a large conditioning number and therefore can not be inverted using regular methods. Each row of the matrix provides a linear equation, while the conditioning number is measure of dependency of the rows (equations). A large dependency number will result in a close to zero determinant, and therefore the matrix cannot be normally inverted. Therefore, we use regularization methods to lower this conditioning number, and then we use the maximum a posterori method to calculate the inverse of the Jacobian.

4. *Test the developed numerical MIT imaging package to perform contrast imaging on a simple model*
   It has been shown that EIT responds linearly to many physiological processes involving movement of a fluid of a constant conductivity into the ROI, resulting in an enlargement of the area covered by fluid (Adler et Guardo, 1996). Cerebral edema is brain swelling caused by excess fluid inside the skull. In this dissertation, as a model to study the performance of the calculation, we investigate the possibility of monitoring the development of cerebral edema, an alteration in the conductivity of brain tissue, using a MIT device proposed to function at a frequency of 50 kHz. In this step, a rather crude model of the tissues inside the head is adopted, along with a relatively modest array of exciting coils and detectors. The objective here is to test the simulator and to assess the feasibility of the approach using a targeted biomedical application. The rationale behind using the MIT imaging technique for such application is that the conductivity of blood is comparatively large with respect to tissues in the head and thus the signal produced by the blood lesion is comparatively larger with respect to other biological constituents. In addition, this magnetic field signal can be detected in the presence of the insulating skull, where contact electrodes of EIT may not perform well in detection (Merwa *et al.*, 2004).

1.3 Methodology

In the following chapters, the method for numerical calculation of the excitation and the detected field for a device is presented. The general methodology involves the numerical solution of a partial differential equation (inhomogeneous Helmholtz equation) by the finite element method (FEM). The steps involved to achieve the reconstructed map of the conductivity are as follows :

1. The formulation of the differential equation describing the general magnetic induction boundary value problem.
2. The variational formulation of the differential equation as implied by the FEM method.
3. Discretization of the ROI and and the choice of appropriate basis functions.
4. Computer programming and solution of the numerical problem (MATLAB)
5. Calculation of the sensitivity matrix (Jacobian) by finding the derivative of the magnetic field or voltage with respect to electrical properties
6. Reconstruction of the conductivity map using the secondary magnetic field and sensitivity matrix
7. Graphical representation of the results in 2D and 3D

Steps (1)-(4) are what is called the forward problem, and are treated in Chapter (3). After step (4), the formulation derived in previous steps is implemented in MATLAB and numerical calculations results are used in the following steps. Steps (5) and (6) are covered in Chapters (4) and (5), respectively. The graphical representations and a detailed discussions of the results are presented in Chapter (6). The forward problem, sensitivity matrix calculation and inverse problem (Steps (6) and(7)) constitute the three main sub-problems of this simulation and each can be addressed in various ways.

1.3.1 The forward problem

To assess and design an MIT system, simulation results are very informative beforehand. For the given geometrical configuration of induction coils and detectors introduced in the next chapter, the associated forward problem is solved to simulate the experiment results. The forward problem provides us with the values of the primary and the induced magnetic field in the entire ROI.

There exist several methods in the literature for formulating the forward problem such as finite element and finite volume (Hollaus *et al.*, 2004b ; Adler et Guardo, 1996 ; Gençer et

Tek, 2000 ; Gencer et Tek, 1999 ; Tanguay *et al.*, 2007 ; Watson *et al.*, 2008). The choice of the forward problem approach along with appropriate boundary conditions (BC), which is well formulated to be numerically robust is the first step. In MIT, the Maxwell's equations, with the applicable BC, govern every electrical and magnetic activities inside the ROI. The four Maxwell's equations can be combined into one inhomogeneous Helmholtz equation, to be solved in the quasi-static regime with specific boundary conditions.

There are several approaches to solve this boundary value problem in the literature. Simplified versions of mathematical formulation are more widely used for MIT compared to other methods, as the computational costs are high in order to develop a full model. The simplifications are mainly neglecting the displacement current term effects which is much smaller in magnitude than the conduction current in biological tissues. Neglecting the displacement current reduces the problem to solving the magnetostatic problem outside of a conductor. However, with the discussion in chapter 2, we see that this is no longer true for frequencies above 1 MHz.

In order to find solutions for differential equations in arbitrary geometries, which do not have very special symmetry or which consist of many interacting components, numerical methods like finite elements are classic approaches. In this method, the ROI is divided into small unit cells of rectangular or tetrahedron shapes in 3D. Then the vectorial Helmholtz equation is solved by finding the weight factor that can be assigned to a set of basis functions, defined on the edges of these unit cells (when ROI is divided into tetrahedrons, the basis set has six members, each defined in the direction of one edge). The fact that the basis functions are defined on the edges of the voxels (tetrahedron elements), simplify the implementation of the boundary conditions between unit cells and the boundary cylinder to the form of vector identities. These conditions should be imposed on this basis functions for the numerical calculation of this vectorial equation.

The method presented here for the forward problem does not exclude the effects of the displacement currents, and is accompanied by an appropriate choice of gauge and the calculation of the sensitivity matrix using direct differentiation. The method used for calculation of the sensitivity matrix proposed in this dissertation leads to a more accurate reconstructed conductivity map, compared to the widely used method in the state of art MIT devices.

Commercial finite element solver packages are available which are able to solve the inhomogeneous Helmholtz equation numerically. However, calculation of the sensitivity matrix using the direct method requires pieces of information from the source code which is not accessible or hard to extract from commercially available FEM packages such as COMSOL. Therefore formulation for the forward problem is developed fully in a MATLAB.

In Chapter (3), we solve the eddy current(forward) problem using full Maxwell's equations.

This method will help us to explore the theoretical limits of the problem without simplifications. The eddy current problem is solved using the finite element method (edge elements) with first order Whitney functions as the basis for the vector field for a proper gauge. Our numerical calculations are verified using available analytic solutions.

1.3.2 The sensitivity matrix (Jacobian)

The magnetic field **B** at the position of the sensors is sensitive to all passive electromagnetic properties. Quantification of such a dependence is obtained by the sensitivity analysis. It specifies the answer to the following question : if you make a small change in the electrical properties of one element, what happens to the field on all the other elements (interaction is considered with n other neighbouring elements). The changes in the values of the **B** field in all the ROI are given by the the product of the sensitivity matrix and the changed value of the conductivity.
There are several methods available in the literature for calculation of the Jacobian (Hollaus *et al.*, 2004b ; Scharfetter *et al.*, 2006). In EIT, adjoint field method is used as a fast method for calculation of the sensitivity (Gómez-Laberge et Adler, 2007 ; Polydorides et Lionheart, 2003 ; Aghasi et Miller, 2012). The method uses variational form of Poisson equation to find an approximation for the sensitivity matrix. The fast calculation method for the sensitivity matrix in MIT, uses the Geselowitz reciprocity theorem (Mortarelli, 1980) and variate the Eq.(4.25) to find an approximation to the sensitivity matrix (Corson et Lorrain, 1962). Both methods consider only the linear terms in their variational formulation, and the sensitivity matrix calculation using these method requires simulation of two forward problem (See chapter (4)). Therefore, calculation of the sensitivity matrix using the adjoint field method in EIT and the Geselowitz reciprocity theorem in MIT can be done independent of the forward problem formulation that is used for calculating the secondary field (the two required fields values can be calculated using any method).
We introduce the direct method in calculating the sensitivity matrix, and show that it performs better than the reciprocity theorem. The direct method extracts the sensitivity matrix from the numerical forward problem applied for the simulation. This sensitivity analysis may be used to find the most sensitive orientation for the sensors around the ROI. The sensitivity matrix calculated using this novel method, developed in Chapter (4), is implemented in the inverse problem in Chapter (5). The sensitivity matrix is calculated using two different methods (reciprocity theorem and our direct method) and the reconstruction results are compared in Chapter (6).

The calculation of the sensitivity matrix is the original contribution of this thesis. Methods for forward and the inverse problem have been around for decades and have been widely discussed in the literature.

1.3.3 The inverse problem

The inverse of Helmholtz problem is determining the conductivity distribution of the medium given the magnetic potential everywhere in the ROI. If we could specify the values of the primary and secondary magnetic potential as a continuous function with a well-defined first derivative everywhere in ROI, an accurate solution would be expected for the inverse problem using the Green's function of Helmholtz equation.
In practice input data are discrete magnetic field values around the ROI. In the numerical models, the maximum number of points for the magnetic vector calculated in the space corresponds to the number of elements used in the calculation. These points may not be expressed in terms of a continuous function with a well-defined first derivative. However, If the field for all these points are used, the inverse Helmholtz might converge to a conductivity distribution with some numerical treatments, and higher number elements improve the chances of convergence of the numerical method. But in practice, the magnetic field can only be measured on the boundary of ROI and for considerably fewer position of elements. Therefore solution to the practical problem deals with a considerable numerical instability.
The solution of the inverse problem converts the field detected by the sensors into a 3D conductivity map. The complete inverse problem is a non linear problem. However, a linear approximation of the problem may be used for finding the change in conductivity (monitoring), considering a priori information about the conductivity of the background. For finding the absolute value of conductivity, it is possible to solve the inverse problem iteratively. The linear and non-linear calculation are done in Chapter (6). However, the high computation costs suggests that MIT is not suitable for absolute imaging (non-linear reconstruction).
There exist extensive attempts and methods to find numerical solution. Different inverse methods for reconstruction are available in the literature (Scharfetter *et al.*, 2006 ; Rosell-Ferrer *et al.*, 2006 ; Soleimani et Lionheart, 2006). Some methods are known not to be applicable for medical use. These methods include the weighted back projection, as a results of the low contrast in conductivity in biological tissues (The best algorithm for a particular situation depends on the exact nature of the problem).
For example, there are statistical training methods like the genetic algorithm in which the system is trained with results from known ROI. However, these methods are very sensitive to the conditions under which the system is trained. Therefore, the method lacks being re-

producible, for instance if the device is moved into another room with different conditions. Therefore, it is not a robust method for our application.
The inverse reconstruction methods that have been used in EIT, including the Newton-one-step error reconstructor (NOSER) or more recent ones, such as the truncated singular value decomposition (TSVD) or Variance uniformization (VU), may also be used in MIT (Scharfetter *et al.*, 2006) as the EIT inverse problem is more ill-posed compared to the MIT inverse problem (the sensors position are fixed in MIT while not in EIT).
Other examples involves Iterative methods such as the Gauss-Newton approach are suggested for linearization of this kind of nonlinear problem, along with an appropriate regularization method. This method can be very time consuming when the number of elements increases. Hence a complete iterative run requires significant computing power, as the sensitivity matrix should be extracted in each iteration. However, in practice, most features of a differential image can already be recognized very satisfactorily after the first iteration, which is a linear approximation. This fact has led to the development of the so-called NOSER method. This method is especially appropriate for dynamical imaging where only the change in the conductivity between two different states of the object under investigation (e.g. lung ventilation) are of interest (Borges *et al.*, 1999) compared to the absolute conductivity values.
Generally, as the inverse problem in the case of EIT has been extensively done in the literature, we can safely say that it is possible to use the same inverse reconstruction method for MIT, as the challenges and conditioning number of the matrices are the same. The feasibility of solving such inverse problems have been shown for similar problems in the literature (Tanguay *et al.*, 2007 ; Casanova *et al.*, 2004 ; Borges *et al.*, 1999 ; Soleimani et Lionheart, 2006 ; Adler et Guardo, 1996). In Chapter (5), the inverse problem is solved using the NOSER method.

1.3.4 Performing differential imaging of the conductivity

We will use this numerical package to perform contrast imaging using a MIT device, which is introduced in next chapter, on a simplified model of the head tissues. We use a disk model with radii of a average sized head and three conductivity layers which represent the main three biological tissues in the head (skull, white or gray matter, and blood). The cylindrical device has dimensions that can perform this imaging on a real head size. In order to investigate the calculate images, we will fix some performance factors such as the number and position of the induction and detection coil (according to the size of the ROI to perform enough measurements) and the operation frequency, which are discussed in section.(2.4). We use this device to detect a fixed volume and value of a conductivity contrast (between the

blood and white matter) at three different positions of the ROI.

We use following criteria to study the reconstructed images : The reconstruction error (normalized error of reconstructed conductivity of mesh cells) for the image. The point spread function (PSF) which describes the response of an imaging system to a point source and quantifies the spread of the point size. This merit is then used to extract the resolution (1/mm) of the image.

We have calculated these criteria and used it to compare the reconstructed conductivity using two sensitivity calculation methods, *the direct method* that is introduced in this thesis in chapter (4) and the other known as the *reciprocity theorem* (Scharfetter *et al.*, 2006).

In following chapter, we discuss the state of art biomedical MIT devices and investigate the possible improvement that can be made to the devices.

CHAPTER 2 STATE-OF-THE-ART IN MIT DEVICES AND POSSIBLE IMPROVEMENT OF THE PERFORMANCE

2.1 State-of-the-art in biomedical MIT devices

Various setups have been proposed and designed for MIT and various configurations of excitation and detection coils have been implemented. The first experimental measurement and picture provided by MIT is reported by *Korjenevsky*'s group from objects with conductivities of 7 Sm^{-1} at 20 MHz (Korjenevsky *et al.*, 2000). Even though electromagnetic screening was done by the means of a metal sheet, the images are not informative for biological applications as a result of of the noise level of the electronics of the device operating at this frequency.
Scharfetter's group (Scharfetter *et al.*, 2006) have reported low resolution near the center of ROI, regardless of the inverse method used in producing the picture. It was reported that these low resolutions at the center are associated with the lack of induced eddy currents around the center of ROI (geometrical constraints). The group has used gradiometry at frequencies near 250 kHz and produced images in the case of conductivity of 0.8 Sm^{-1} of the target (around biological conductivity range) (Igney *et al.*, 2005).
In any design, the detection of the secondary induced field in presence of the stronger primary field is a challenge, as the primary magnetic field masks the secondary field. There is agreement among groups working in the field that gradiometry (subtraction of the signals in a pair of differential coils) is a good approach for detection of the secondary signal, as removing the primary signal is not an experimentally easy task (See Section (2.2)). However, there are other methods for subtraction of the primary field such as positioning the sensors in a direction less sensitive to this field.
In order to obtain a larger secondary signal, it was proposed that bio-medical MIT systems should use higher frequencies (Holder, 2004), as they are investigating materials with low conductance. However, the limitations in the electronics at higher frequencies such as parasitic capacitance crosstalk (Guardo, 2013) prevent high frequency imaging from being practical. For example, a reasonably good wire of one meter has capacitance of some pF, at the relatively high frequency of 10 MHz. The detected signal at this frequency can be mixed with a considerable amount of noise (parasitic capacitance) signal according to this effect in the wire (detection constraints).
A recent apparatus proposed by (Zolgharni *et al.*, 2009b,a) was used to develop a model which is able to detect hemorrhagic cerebral strokes. This model, which is simulated at 10 MHz (not favorable in terms of practical electronics), is used to detect development of a

reasonable size lesion within the skull. Blood has a relatively high conductivity 1.097 Sm^{-1} at 10 MHz compared to other brain main tissues like gray or white matter (0.18 Sm^{-1} on average at 10 MHz), and will provide a relatively high contrast in the resulting image, which makes it detectable in its background. However, performing and building a device operating at 10 MHz has not yet been tested considering the electronic limitations which affects the secondary magnetic field signal detection.

Models so far developed in MIT for bio-medical applications have not been successful in modeling a practical device due to various constraints which will be discussed in following sections. In order to elaborate more on practical modeling of such device, in the following sections, we discuss various opportunities for improvement.

In the following sections, we discuss the physical properties of biological tissues that fundamentally affect the performance. We show that potential improvement in the performance of the device can be achieved by geometrical modifications, alternative detection methods, and a suitable configuration of sensors.

2.2 Estimation of eddy currents in biological tissues

Properties of biological tissues directly influence the design of the MIT system. Furthermore, even methods in the inverse problem are affected by the properties of biological tissues. For example, as the contrast between the properties of biological tissue are low, using the "weighted back projection" image reconstruction method for the inverse problem do not produce acceptable results (Griffiths, 2001 ; Vauhkonen *et al.*, 2008 ; Adler *et al.*, 1998). Table (2.1) shows the typical values of conductivity and relative permittivity of the biological tissues which are constituents of the ROI. Generally, biological tissues are low in conductivity and permittivity, and have a permeability close to that of free space $\mu_0 = 4\pi \times 10^{-7}$ $\mathrm{H}m^{-1}$ (Griffiths, 2001). As a consequence, the induced currents are small and this leads to small secondary magnetic field.

Displacement currents induced in the biological tissue are in phase with field and are proportional to the square of the frequency. So, in case of the detection of the displacement currents, if we go up in frequency, detected signals are stronger. For instance, the secondary field detected in muscle which consists mainly of water (σ =1 $\mathrm{S}m^{-1}$) at 10 MHz is detected to be 1 percent of the original signal in the device used by (Scharfetter *et al.*, 2001). The total change in the amplitude of the signal is $(1 + (0.01)^2)^{\frac{1}{2}} - 1 = 0.00005$ or 0.005% of the total signal. The change in amplitude will be slightly larger than this because of the permittivity of the water. This value is still smaller than the signal ($|\Delta B/B| < 0.25$), at a frequency of

200 kHz for industrial MIT (Peyton *et al.*, 1996).

Table 2.1 Dielectric properties (experimental) at 50 kHz (our frequency range of interest for measurements) assigned to each tissue type (Gabriel *et al.*, 1996c,b,a).

Tissue	$\sim$ Conductivity S m^{-1}	$\sim$ Relative permittivity $\frac{\varepsilon}{\varepsilon_0}$
Muscle	0.4	1.5×10^4
Blood	0.6	2.1×10^3
Skull	0.035	2×10^2
Skin (Dry)	0.04	2×10^4
Fat	0.025	300
Brain gray matter	0.15	3×10^3
Brain white matter	0.11	1×10^3

The skin depth δ can be estimated for each of the tissues by Eq. (3.18) substituting the effective conductivity $\sigma_{eff} = |\sigma - \imath\omega\epsilon_r\epsilon_0|$ instead of the conductivity. This value for muscle at 50 kHz is about 8.9 meter, while at 10 MHz is about 0.28 meter, which shows that our measurement is not limited by the skin depth at 50 kHz, but starts to be limited at 10 MHz frequency.

It has been suggested that one cannot go beyond 2 MHz in frequency for imaging biological tissues because of β dispersion (associated with the polarization of cellular membranes and protein and other organic macro-molecules) that happens in biological tissues in higher frequencies (Somersalo *et al.*, 1992). As stated before, the effect of capacitive noise from electronics, on the main signals also increases as we go higher in frequency. A working frequency should be selected which also considers these biological limitations along with other limitations.

The electrical properties of tissues and blood, like conductivity and relative permittivity are frequency dependent and are reported in the literature from experimental results and also some models (Gabriel *et al.*, 1996c,b,a).

Generally, dielectric constants of biological tissues decrease with increasing of frequency, while conductivities are weakly dependent on frequency and can be considered to be constant between 10 Hz and 10 MHz. Dielectric properties are assumed to be isotropic, and the relative permeability of all tissues is considered to be unity (μ_0) in this study. The reported values in Table (2.1) are the electrical properties for a frequency of 50 kHz which are used throughout our simulations.

2.3 Possible improvements in the performance

The specific application of the MIT device will critically affect the factors that are considered for its optimization. For bio-medical application, the design of the system is mainly affected by low intrinsic contrast in conductivity of the region and also low absolute value of conductivity of materials, which influence the size and density of the eddy currents and the corresponding secondary magnetic fields.
Devices proposed in the literature for Bio-medical MIT imaging may be improved by two types of modifications :

1. Modifications of the geometrical layout of the device (e.g. position of the induction coils) in order to increase the value of the induced current at the center of the ROI.

2. Modifying the detection method to increase the signal to noise ratio (SNR) of the data used for reconstruction, by changing of the type and the number of sensors and their orientations to reject the primary field.

These opportunities are used to make improvement to the state of art devices. The details of each item is discussed in the following sections.

2.3.1 Modification in the induction geometry

The layout of excitation coils and detectors of the MIT device influences both the induction and the detection of the secondary signal. Excitation coils generate magnetic fields, which induce eddy currents in conducting regions and these currents produce secondary magnetic fields in the ROI, which are informative for finding the unknown desired property. As the secondary field is much lower in amplitude (10^{-2} to 10^{-6} times that of the primary field depending upon frequency and induction coil configurations), the first challenge is thus to design a detector configuration for the secondary field in the presence of background primary field (Griffiths, 1999). Different configurations and frequencies of excitation, have a direct effect on the density and distribution of eddy currents. In the induction of eddy currents, present devices using local exciting coils suffer from the fact that as you get further away from the inducing coil, the magnetic field of the small coil falls of with $\frac{1}{r^3}$ (as the field can be approximated by dipole field). Thus the induced primary magnetic field is the lowest at the center of the ROI and therefore less eddy current is distributed in the ROI.

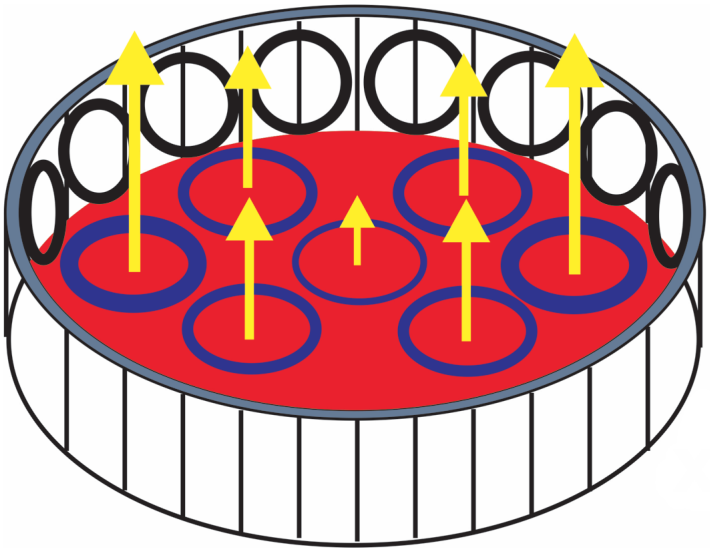

Figure 2.1 Schematic presentation of eddy currents distribution for excitation loops on the sides. Lower density of eddy currents at the center of ROI is due to its' comparably larger distance from the coils

Schematic presentation of eddy currents are shown in Fig.(2.1) for excitation loops on the sides. The thickness of each ellipse refers to the density of eddy current in that area. The arrows correspond to the magnitude of the Z component of secondary magnetic field (thickness of arrows are proportional to the strength of the field). The eddy current densities, therefore the strength of the field lines is less in the middle of ROI in the case of excitation from the sides.

As reported by (Scharfetter *et al.*, 2006), the density of the primary induced field is low at the center in this type of excitation. Therefore the density of the eddy currents is low in the middle of the ROI. The resulted sensitivity to the change in conductivity is minimum near the center of the ROI and increases when moving towards the border (Merwa et Scharfetter, 2008), in this type of induction.

In detection of the secondary signals, even if the secondary field is a result of proper induction and is present everywhere in ROI for detection, present devices suffer from the fact that as sensors are detecting from the sides at the same height as the induction coils, they cannot properly detect the field in the center of ROI due to their distances and orientations ($\frac{1}{r^3}$).

In summary, a change in the induction and detection geometries might enable us to induce

and detect stronger components of the magnetic field which would potentially improve the overall imaging results. The proposed MIT device uses concentric coils parallel to x-y plane for induction. This induction method will provide a more uniform exciting field within the ROI, provided no significant eddy current screening is effective (which is correct at 50 kHz), we expect stronger induction at the center of ROI.

2.3.2 Enhancement of performance in the detection

Different detection techniques have been used in the literature for detection of the secondary field, using inductive coils as sensors, each proper for specific geometries and applications. Some configurations use the same set of coils for both induction and detection. Other methods, like using compensation coils can be made mechanically very stable with most of the primary signal canceled out (Igney *et al.*, 2005). However, this method can only cancel out the primary signal of one excitation coil position at a time, the one which is directly in front of it. Also, phase sensitive detection can also be used to exploit the phase lag of the secondary signal. To improve the measurement precision, we should find a method for better subtraction of the primary signal.

Another method focuses on favorable orientation of the detecting coil that makes it less sensitive to the primary field (Watson *et al.*, 2004). This approach considers the sensitivity profiles of the sensor to the secondary field for the specific configurations. The sensor then is placed in a direction with maximum sensitivity. This method has affected the design of our device, for finding the position and orientation of the sensors. For detection, we have used a circular array of coil sensors, perpendicular to the x-y plane located on the outer surface of ROI and as a result, they are less sensitive to the primary field in the z direction.

The low conductance of biological tissues require higher frequencies for producing a stronger secondary field. However, parasitic capacitance cross-talk resulting from electronics will introduce peaks to the detected fields that are almost as large as secondary field.

Furthermore, the field range of the sensors limits the performance of the device. The primary field is up to 10^6 stronger than the secondary field. Therefore sensors should be able to be functional in a wide range and should be able to detect changes of an order of pT in the field for frequencies around tens of kHz.

As well as the orientation, using different types of sensors can improve the performance. Giant Magneto Impedance (GMI) sensors are smaller in size (less limitation on the number of sensors and their orientation) compared to the coils and experience less cross-talks due to their structure. Therefore, the spatial resolution of the device can be increased using GMI sensors.

Recent studies (Merwa et Scharfetter, 2008) show that it is essential to run simulations for designing of a MIT device, in order to answer questions such as what resolution can be achieved or what type of receivers and in which configuration, is a necessity in order to achieve the desired requirements. Sensor characteristics such as the sensitivity, the dynamic range and the measurable field range will affect the spatial resolution of the image (Griffiths *et al.*, 1999 ; Hollaus *et al.*, 2004a).

2.3.3 Considerations on the spatial resolution

The resolution of an imaging technique, whether electrical or magnetic, is limited by the number of independent measurements done on the system. The model developed in Appendix.(A) illustrate this criterion.
There is a fundamental limit to the resolution, and that is the amount of available information in the data. This information depends on the measurements made, or the possible combination of induction and detection. In the case of MIT the number of independent measurement is usually much lower than the number of voxels (under-determined system). Furthermore, the measurements are correlated to a certain degree which further reduces the available information.
In addition, if we consider the presence of noise, the spatial resolution of the reconstructed image from MIT data now depends on two major factors (Guardo, 2013). The first is the number of linearly independent measurements that can be made with a chosen configuration of coils and sensors. The second is the signal-to-noise ratio (SNR) of the detected signal.
In order to design an optimized non-contact tomographic device with a proper resolution, for any application (Biomedical, Industrial and etc.), we have considered several geometrical factors and also wide range of detection methods. The location of objects inside the ROI, the number of excitation coils and their configurations, and the number of receivers and their configurations are important factors in designing a proper device which will be considered in the device proposed in the next section.
So far, the achievable resolution in EIT devices was shown to be suitable for *in vivo* functional imaging of for instance, lung ventilation or gastric emptying, etc (Coulombe *et al.*, 2005). In principle, this could be the case for MIT and studies done so far supports this hypothesis (Zolgharni *et al.*, 2009b). The present resolution of MIT devices are insufficient for anatomical studies in which other modalities are more appropriate (MRI, CT-scan, etc). However, the option of multi-frequency MIT is an approach to improve the device performance by additional measurements. With more informative imaging results, multi-frequency MIT could be more effective in diagnosis areas (Zolgharni *et al.*, 2010).

2.4 Proposed device specifications

This device is specifically proposed for the detection of the lesions in the brain. We will simulate a three tissue cylindrical disk model as the brain containing a cylinder of raised conductivity, simulating the oedema. The cylindrical ROI with a diameter 45 cm and height of 50 cm is shown in Fig.(2.2). The ROI dimensions are proposed to be suitable to surround average human head with a average diameter of 20 com and its average height (22 cm). The yellow boundary area indicated in Fig.(2.2).a is a cylindrical region with the radius 30 cm and the same height which is solely dedicated to position the head. Therefore, this yellow line is also the boundary of our reconstruction mesh.
Around this yellow boundary area, there are six concentric circular induction coils with a diameter 30 cm parallel to each other and positioned 10 cm apart from each other, positioned at different heights of the ROI cylinder. In between each induction coil, array of 16 detection coils with a diameter of 10 cm is placed perpendicular to the induction coils. This detection coil radius of 50 mm has been used before in MIT setups to detect similar field range from cerebral hemorrhage (Zolgharni *et al.*, 2009a).
The exact position of each detector shown in Fig.(2.2) is assigned to the center of each circular coil or GMI sensors. GMI sensors are also promising for this application as their performance result (detectable field range) suggests (Dufay *et al.*, 2013b ; Guardo, 2013). Position of the other sensors can be obtained by transforming the coordinates of a given sensor by 22.5 degrees step rotation around the Z axis.

2.4.1 The head model

The simulated device should detect the secondary magnetic field associated with the change in the background conductivity, as the lesion with different electrical properties emerges. The head is estimated with a disk model with a radius of 20 cm and the thickness of 10 cm, having three layers with distinct electrical properties as shown in Fig.(2.2).
The electrical properties (conductivity, permittivity, permeability) are substituted by the values of the skull for the outer layer, an average over the of gray and white matter for the middle layer and the blood properties for the inner layer. Even though the model is a crude estimation of the real head model, it is conventional to study the feasibility of detection of stroke at certain frequency using simple geometries such as circular or cylindrical brain models (Scharfetter *et al.*, 2006).

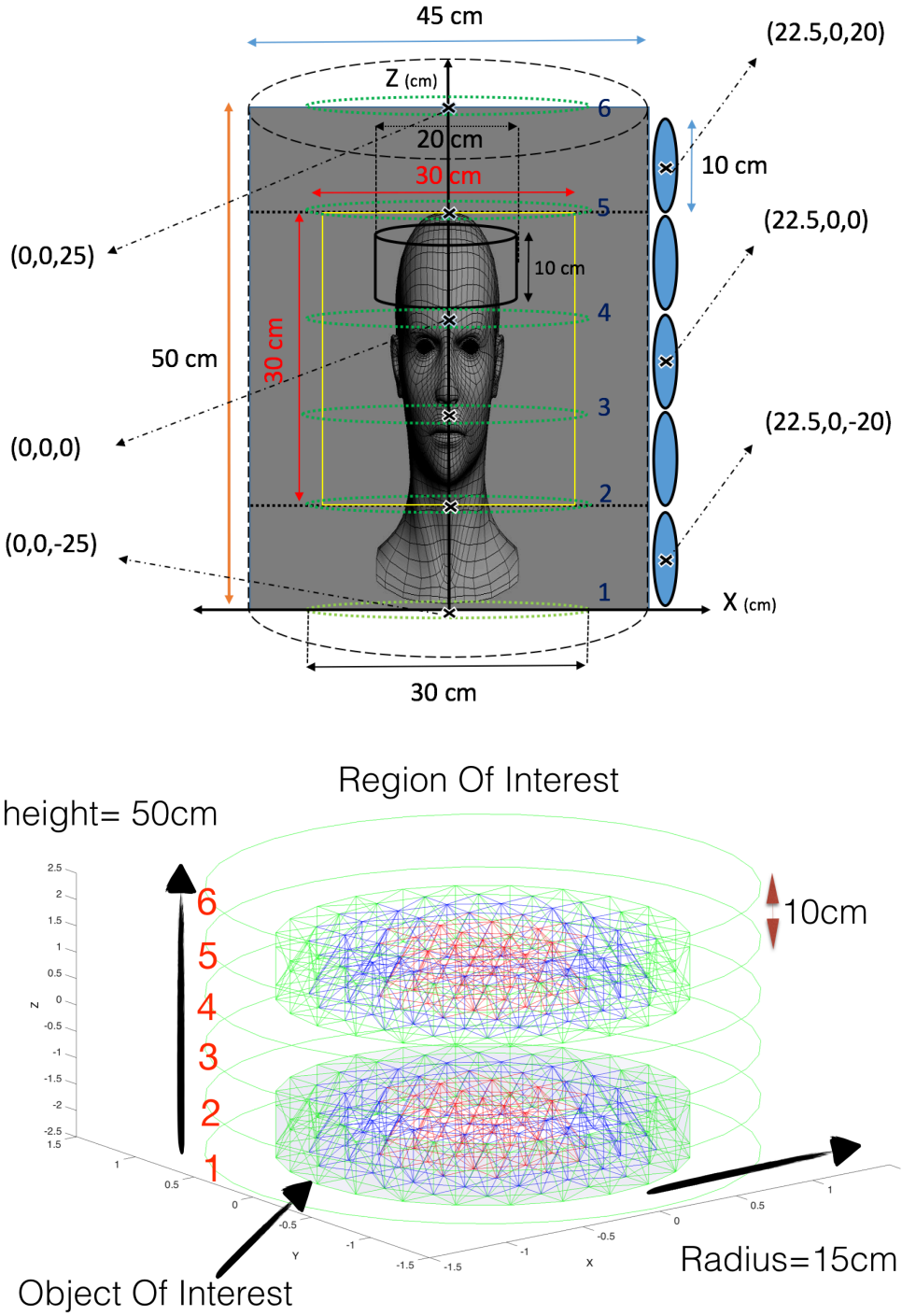

Figure 2.2 Magnetic induction tomography device (top figure) for detection of haemorrhagic cerebral edema operating at 50 kHz. The position of the excitation coil parallel to the x-y plane (the six round green coils) is specified. One of sixteen detection coils in each row between the excitation currents is shown with their positions (location of the others each can be find by 22.5 degree rotation along the z axis). The yellow square region is the region which we perform the reconstruction of the conductivity. The brain is modeled as a disk with distinct electrical properties (bottom figure) in each layer which will be used as targets in the cylindrical ROI.

These simple models can be implemented to answer so many primary questions such as what is the value of the secondary signal for a certain conductivity contrast size at a certain frequency or the achievable resolution. More realistic head models like a twelve layer head mesh have been used by (Zolgharni *et al.*, 2009b). Using this more realistic mesh model is necessary as the assumption of uniform conductivity of the background (white and gray matter) is not entirely true for a complex tissue like brain. This nonuniform background will produce additional noise in conductivity reconstruction. However, as this more realistic mesh requires more computation resources, we have decided to use the simple model to address feasibility study and the realistic head mesh as the subject of future works.

2.4.2 The geometry for induction and detection

One of the drawbacks in state of the art devices, discussed in section (2.3.1), is the lower resolution of the reconstructed image at the center of ROI. The higher the densities of the eddy currents in the ROI, more information and higher resolution are expected. As a result of this geometry used for induction, the primary magnetic field is almost uniform in the entire ROI, which results in stronger eddy currents at the center of ROI. This concentric induction pattern produces a uniform density of field and therefore eddy currents in the ROI, could potentially provide higher resolution reconstructed images at the center of ROI.
The perpendicular positioning of receiver coils with respect to the induction coils make the sensors less sensitive to the strong primary signal in Z direction and therefore will result in higher signal to noise ratio of the secondary signal at the sensors (Watson *et al.*, 2005).

2.4.3 The number of induction and detection coils

Ultimately, the number of independent measurements bound the spatial resolution (this number is much lower than the number of voxels or pixels in the image reconstruction method). As shown by (Tanguay *et al.*, 2007), more than 100 measurements is required to obtain desired resolution in 2D. For example a 2D medium discretize into 10×10 pixels, we will need at least 100 linearly independent measurements to obtain a solution. With 10×10 pixels the spatial resolution is around 10 % of the object's diameter.
With 6 induction coils, the number of detectors will determine the number of independent measurements (see appendix (A)). The number of induction and detection coils are chosen so that we can achieve a total of 96 effective pixel at each layer between the induction coils. Considering that each layer in the yellow region has an additional array of sensors on its top

and bottom row providing additional information to this 96, combination number of induction coils and detectors provides enough data point for a 2D layer.
Our magnetic induction tomography device has (5×16) 80 detectors (see Fig.(2.3)) covering the entire inside wall of the cylindrical ROI, excluding its top and bottom surfaces, to maximize the number of independent measurements in 3D. The detection coils around the ROI will provide 480 independent measurement in 3D (96 measurement at each level). As the induction and detection coil are not the same in this device, the number of independent measurements is not half of 480 (See appendix (A)).

2.4.4 The operation frequency

The induced signal for a given conductivity contrast is proportional to amplitude and frequency of the excitation field. The skin depth value (given by Eq.(3.18)) estimated for the head tissue is about 8.9 meter at 50 kHz, while is about 0.28 meter at 10 MHz, which starts to be comparable to the size of the head model and therefore starts to be limited at 10 MHz frequency. Therefore, in principle we could operate up to about 10 MHz before the skin effect starts to screen the center region. However, at higher frequency, there are also noise and crosstalk problems.
The amplitude of the primary field is also limited due to the amount of electromagnetic exposure that is safe for a certain tissue. The signal absorption rate (SAR) is associated with each tissue and informs us about the amount of electromagnetic field which can be induced in the ROI. The amount of energy in the induced electromagnetic field (absorbed by the tissue) is proportional to the square of frequency (Eq.(**??**)). We investigate our device for exposure safety using the SAR criteria in section.(6.5.6).
And last, but not least, for the targeted application the conductivity contrast is higher at lower frequency. The conductivity contrast due to the ischaemic stroke, which is a result of cell swelling and reduction of the intracellular space, is effected the most at low (kHz) frequencies (Horesh *et al.*, 2005). Holder has shown in an animal model that the conductivity changes can be by as much as 60% at 50 kHz (Holder, 1992).
The effective conductivity ($\sigma_{eff} = |\sigma - \imath\omega\epsilon_r\epsilon_0|$) contrast between blood and normal brain tissue is greatest at frequencies below 10 kHz (Gabriel *et al.*, 1996c). MIT researchers are now designing hardware for operation down to these frequency (Scharfetter *et al.*, 2008). However, a compromise has to be made between the higher signal to noise ratios, which is proportional to frequency and is higher for higher frequencies, and the conductivity contrast between the two tissues which is higher at lower frequencies.
The frequency of 50 kHz will result in a contrast (between blood and average of white and gray matter) of a factor 8, which is better than the factor of 6 which happens at 10 MHz fre-

quency. Also our simulation results show that for an average size contrast of lesion produces a change secondary magnetic field of pT order of magnitude which is detectable by the both sensor types proposed at such frequency (Guardo, 2013). Even though the displacement current are more dominant in higher frequencies (proportional to the square of the frequency), we have considered a complete Full Maxwell's model for the numerical simulation which includes the displacement currents and therefore it can be applied generally for all frequencies. Therefore, considering all of the above, 50 kHz appears to be a sounded operation frequency for the purpose of our simulations. The change in the contrast of effective conductivity for the blood and the brain with respect to frequency is not considerable between frequencies of 10 to 100 kHz (Gabriel *et al.*, 1996c). Therefore using for instance 75 kHz will not produce a significant change in the secondary magnetic field detectable at the sensors.

2.5 Simulation procedure for primary excitation field and secondary field computation

We excite each coil from the six parallel concentric excitation coils one by one. For simplicity, the simulation described for this model considers a unit excitation current (1 A). The coil detectors record the **B** field perpendicular to its surface and the corresponding induced voltage V each time. We use six excitation pattern data sets as the input for the inverse problem. The integration of the **A**-vector (magnetic vector potential) on the edges of elements, where sensors are located, specifies the corresponding induced voltage V of the secondary field in an equivalent one turn coil (see chapter (3)).
The inverse problem may take components of **B** or its corresponding induced voltage V as the input. The one used in this reconstruction problem is V.

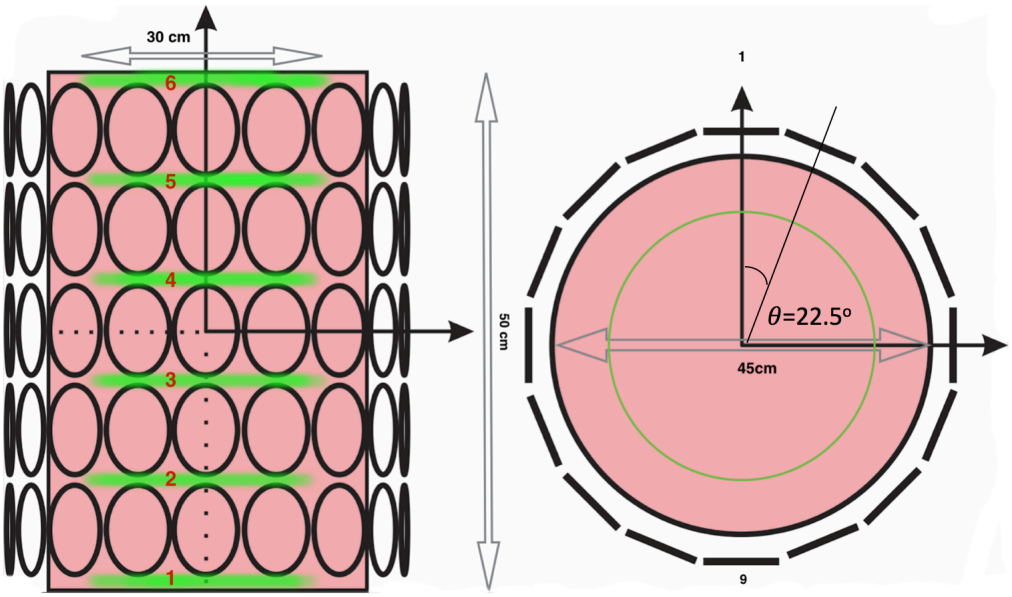

Figure 2.3 Sensor arrangment around the ROI. There are 5 arrays of 16 detecors, arranged symmetrically on the surface walls of the cylindrical ROI with radius 45 cm and height 50 cm. The distance between the sensor arrays and the surface wall shown in this figure is for clarity. Excitation coils with radius 30 cm are shown in green.

The forward formulation calculates the secondary **B**-field produced by the object of interest in any of the elements. Such **B** magnetic fields are known everywhere in the ROI as a vector with 3 components in each element (tetrahedra). The output of the inverse problem (the conductivity difference map) is calculated for fewer mesh elements compared to the number of mesh elements that the forward calculation has used for the secondary magnetic field. Simulated measurement data were generated using the model phantoms, and Gaussian pseudo-random noise was added to the data.

As the device does not have sensors within the ROI, measurement of the secondary magnetic field is only plausible on the surface of the cylinder of the ROI . Therefore, sensor arrays are fixed on the outer surface and around the object of interest. The number of sensors on the surface, (80 sensors, as shown in Fig. (2.3)) times six (number of possible excitation with 6 coils) identifies the number of possible measurement (480). In practice, some measurements are dependent, and as a result, the rows in the sensitivity matrix are not very distinct (See Chapter (6)).

For more realistic models, noise is added to this system at different Gaussian levels (in the m^o order of standard deviation). They have been added to the simulated data as the simulation

errors. However, other effects like the displacement of the disk in the ROI (movement of the head) may also be modeled and is a subject proposed for the future work. This error may be calculated by finding the sensitivity matrix for the case that the coordinates of the induction coils are each shifted by a finite amount (given the symmetry of the problem, displacement of the disk is equivalent to a shift in the induction coils).
The procedure for obtaining a reconstructed conductivity image for the MIT device proposed in this dissertation are as follows :

1. Starting with a ROI filled with air, we apply current in each excitation coil (shown in green) individually and measure the resulting magnetic field and their corresponding induced voltage in all sensors. The medium within the ROI has the electrical properties of free space. We call this calculated V_p that is the primary voltage. This procedure is done for each coil and V is recorded for 80 sensors.

2. We consider the ROI with the object of interest (target with properties of biological tissue) inside it. The disk contains two concentric conductive regions, the inner one being the white or gray matter, and the outer layer being the skull. The value of electrical properties for these regions are prior information provided to the problem. (See Chapter (5)). In other words, we have estimated that in measurement of the conductivity, its value is known approximately in the conductive region of the ROI (we are interested to detect the change in this conductivity value). We apply the currents in each excitation coil one by one and record the induced voltage V_1 and calculate the sensitivity $\mathbf{S}_{\sigma V}$ for each excitation coil. When it comes to the inverse problem, we assemble the sensitivity matrix for each measurement (each coil running) on the top of the other one, to get the complete sensitivity matrix for six excitation pattern. Therefore, the main sensitivity matrix of the device is six times in dimension of that for one excitation coil.

3. We add the effect of cerebral edema, by considering it as blood with its corresponding electrical properties at 50 kHz. We apply these conditions by changing the conductivity of the conductive elements of a certain area (a circle at the center of the white and gray matter disk). Then we apply the excitation currents again and calculate V_2 which is the induced voltage in the presence of the lesion.

4. As the secondary magnetic field signals are in phase quadrature with the primary signal and relatively very small in magnitude, $\frac{V_1}{V_p}$ and $\frac{V_2}{V_p}$ are effectively the phase angle (See Chapter (3)). The phase difference $\Delta\phi$, is a measure of the signal due to the lesion and

is given by :

$$\Delta\phi = \frac{V_2 - V_1}{V_p} \tag{2.1}$$

5. This phase difference is used as the input of the reconstruction procedure, using the sensitivity matrix is found in the second step.

If the phase difference $\Delta\phi$ is large enough compared to the noise level, the change in conductivity is detectable.

A monitoring device (Dynamic MIT)

The results presented in Chapter (6) show that using the direct method for calculating the sensitivity instead of the reciprocity theorem, the reconstructed image of the differential conductivity has less noise and the target image is better localized compared to its original shape and position. The direct method is promising in low frequency differential MIT imaging, despite its computational cost for calculation of the sensitivity matrix. However, the method is not preferred for absolute imaging of the conductivity value.
The direct method used in calculation of the sensitivity matrix, has shown improvement in the accuracy of the reconstructed conductivity required for monitoring compared to the other methods. When the sensitivity matrix is calculated once, the mathematical procedure for conductivity map reconstruction corresponding to certain field measurement is a matrix multiplication which is a relatively fast procedure (about 4 seconds). This fact makes real time imaging feasible with this device and may acquire a dynamic conductivity map of the ROI. The detailed investigation of a real-time device is beyond the scope of this document and is introduced as a subject of future work in Chapter (7).
In the following chapter, the general solution of the forward problem is developed and then the finite element method (FEM) is applied to evaluate the **A** (magnetic vector potential) field which is used to calculate the **B** field and the voltage and phase change (2.1) it induces in the coil sensors.

CHAPTER 3 FORWARD PROBLEM FORMULATION FOR MAGNETIC INDUCTION TOMOGERAPHY

3.1 Solutions to Maxwell's and Helmholtz equations

The purpose of solving the forward problem is to compute the secondary field signal resulting from a primary exciting field for a given setup (geometry, electrical properties distribution and electrical stimulations). Therefore, the forward problem results in calculated values of the magnetic field, as 3D vector distribution in the space for each element of ROI with a specific conductivity, permittivity and permeability distributions all over the region.
The *full Maxwell's equations method* is the name which refers to our forward problem. We show that Maxwell's equations lead to the inhomogeneous Helmholtz equation. The solution to this vectorial equation is a continuous vector field in 3D space. In what follows, we will break the ROI into small cells in order to attack the problem numerically using FEM. The edge element formulation for the homogeneous Helmhotlz equation has been developed by (Reddy *et al.*, 1994). The edge element formulation for the inhomogeneous equation is introduced and implemented in the following section and the results are bench-marked with analytic solutions.
Solutions to the inhomogeneous Helmholtz equation as a partial differential equation (PDE), depend critically upon the BC and also upon the form of the in-homogeneous term. With these considerations, there might exist a Green's function as a general solution. However, this is not the case for most practical problems and these major groups of PDEs should be treated numerically in most cases.

3.1.1 Maxwell's equations and a proper gauge

We begin with Maxwell's equations :

$$\nabla \cdot \mathbf{D} = \rho \tag{3.1}$$

$$\nabla \cdot \mathbf{B} = 0 \tag{3.2}$$

$$\nabla \times \mathbf{E} = -\frac{\partial \mathbf{B}}{\partial t} \tag{3.3}$$

$$\nabla \times \mathbf{H} = \mathbf{J} + \frac{\partial \mathbf{D}}{\partial t} \tag{3.4}$$

where $\mathbf{E}$ is the electric field, $\mathbf{B}$ is the magnetic field, and ρ and $\mathbf{J}$ are the charge and current density respectively.
Assuming a linear homogeneous and isotropic and dispersion-less medium, we can use the local constitutive relation for the electrical displacement $\mathbf{D}$ and the auxiliary field $\mathbf{H}$ to write them in terms of $\mathbf{E}$ and $\mathbf{B}$:

$$\mathbf{D} = \varepsilon \mathbf{E} \tag{3.5}$$

$$\mathbf{H} = \frac{1}{\mu}\mathbf{B} \tag{3.6}$$

where ε is the permitivity and μ is the permeability of the material.
As the magnetic field $\mathbf{B}$ is divergence-less, it can be expressed with the aid of a vector potential (Griffiths, 1999) :

$$\mathbf{B} = \nabla \times \mathbf{A} \tag{3.7}$$

Using Eqs.(3.3) and (3.7) we may write :

$$\begin{aligned} \nabla \times \mathbf{E} &= -\frac{\partial(\nabla \times \mathbf{A})}{\partial t} \\ \nabla \times (\mathbf{E} + \frac{\partial \mathbf{A}}{\partial t}) &= 0 \end{aligned} \tag{3.8}$$

If the curl of some quantity vanishes, then that quantity can be written as the gradient of a scalar.

$$\begin{aligned} \mathbf{E} + \frac{\partial \mathbf{A}}{\partial t} &= -\nabla V \\ \Rightarrow \mathbf{E} &= -\frac{\partial \mathbf{A}}{\partial t} - \nabla V \end{aligned} \tag{3.9}$$

The first term on the right-hand side of Eq.(3.4) can be decomposed into the external current $\mathbf{J}_s$ and conduction current ($\mathbf{J}_\sigma = \sigma \mathbf{E}$). So the Eq.(3.4) can be written as :

$$\nabla \times \mathbf{B} = \mu \mathbf{J}_s + \mu\sigma \mathbf{E} + \mu\varepsilon \frac{\partial \mathbf{E}}{\partial t} \tag{3.10}$$

using the phaser notation for $\mathbf{E}$ and $\mathbf{B}$ and $\mathbf{A}$.

$$\begin{aligned} \mathbf{E}(r,t) &= \mathbf{E}(r)\exp(\imath\omega t) \\ \mathbf{B}(r,t) &= \mathbf{B}(r)\exp(\imath\omega t) \\ \mathbf{A}(r,t) &= \mathbf{A}(r)\exp(\imath\omega t) \end{aligned} \tag{3.11}$$

In Eq.(3.11), $\imath = \sqrt{-1}$ and ω is the angular frequency. Substituting Eqs.(3.7) and (3.9) into Eq.(3.10), we obtain :

$$\nabla \times \nabla \times \mathbf{A} = \mu\mathbf{J}_s + \mu\sigma(-\frac{\partial \mathbf{A}}{\partial t} - \nabla V) + \mu\varepsilon\frac{\partial}{\partial t}(-\frac{\partial \mathbf{A}}{\partial t} - \nabla V) \tag{3.12}$$

After rearrangement of terms in Eq.(3.12) and dividing both sides by μ, we get :

$$\frac{1}{\mu}\nabla \times \nabla \times \mathbf{A} + (\imath\omega\sigma - \varepsilon\omega^2)\mathbf{A} + (\sigma - \imath\varepsilon\omega)\nabla V = \mathbf{J}_s \tag{3.13}$$

Solving this equation in a specific gauge will specify a set of $\mathbf{A}$ and V which are the necessary factors in the calculation of the total magnetic field. Its form suggests that if we use the temporal gauge (V=0) and let the electric field be totally dependent upon $\mathbf{A}$, Eq.(3.13) is the inhomogeneous Helmholtz equation. Choosing this gauge is beneficial while implementing the finite element formulations as it cancels the last term on the left hand side of the equation. In classical electromagnetism, according to gauge theory, one can add the gradient of a function f to the vector field $\mathbf{A}$, as long as the time derivative of the same function f is simultaneously subtracted from V (Griffiths, 1999).

$$\begin{aligned} \mathbf{A}^* &= \mathbf{A} + \nabla f \\ V^* &= V - \frac{\partial f}{\partial t} \end{aligned} \tag{3.14}$$

In temporal gauge (V^*=0), the time derivative of the function f is set equal to V. The gradient of the function f which satisfies the former statement, is what is added to $\mathbf{A}$, which is given by Eq. (3.13).
Considering temporal gauge, the inhomogeneous Helmholtz equation is :

$$\frac{1}{\mu}\nabla \times \nabla \times \mathbf{A} + (\imath\omega\sigma - \varepsilon\omega^2)\mathbf{A} = \mathbf{J}_s \tag{3.15}$$

which is used in our the numerical calculation. The solution to Eq.(3.15) will specify the **B** field. It is convenient to define :

$$\kappa^2 = \omega^2\varepsilon - \imath\omega\sigma \tag{3.16}$$

where κ is the complex wave number which depends upon the material properties and the operation frequency. It has real and imaginary parts. If we consider $\kappa = \alpha + \imath\beta$ then

$$\begin{aligned}\alpha &= [\frac{\omega\mu\sigma}{2}\sqrt{(1+(\frac{\omega\epsilon}{\sigma})^2)} - \frac{\omega\epsilon}{\sigma}] \\ \beta &= [\frac{\omega\mu\sigma}{2}\sqrt{(1+(\frac{\omega\epsilon}{\sigma})^2)} + \frac{\omega\epsilon}{\sigma}]\end{aligned} \tag{3.17}$$

α is called attenuation constant and β is a measure of the radian phase shift per meter (the phase constant). The wavelength λ and the skin depth δ (the distance wave needs to travels before it decays by e^{-1}) are defined as :

$$\begin{aligned}\lambda &= \frac{2\pi}{\beta} \\ \delta &= \frac{1}{\alpha}\end{aligned} \tag{3.18}$$

In this calculation, we do not neglect the skin effect.
For an excitation frequency ω if the skin depth is large compared with the thickness of the sample, which will normally be the case for biological tissue, then the secondary field lags primary signal by 90 degrees and phase sensitive detection can be an option (Griffiths, 2001). With κ defined, our equation will become :

$$\frac{1}{\mu}\nabla \times \nabla \times \mathbf{A} - \kappa^2\mathbf{A} = \mathbf{J}_s \tag{3.19}$$

Where **A** is our vector potential which has this general form :

$$\mathbf{A} = A_x\hat{x} + A_y\hat{y} + A_z\hat{z} \tag{3.20}$$

In the following section, the finite element method is used to develop a numerical algorithm which solves the Helmholtz equation.

3.2 Finite element method formulation

The Finite Element Method (FEM) is a numerical technique which finds approximate solutions for partial differential equations. It uses the variational method to solve the problem by minimizing an associated error function. Similar to the idea that connecting many small straight lines can approximate a large curve, FEM provides methods for connecting many simple element equations over many small sub-domains, finite elements, to approximate a more complex equation over a larger domain.
There are two widely known FEM methods for the numerical treatment of PDEs : Nodal Basis and Edge Basis. The former is suitable for scalar PDEs and the weighting functions (Whitney function) are used as a basis in the variational formulation. These bases are defined at the corner of each element and have such properties as having a well defined gradient, which is necessary for development of the weak formulation of equations like Eq.(3.15). In the weak formulation process, the goal is to reduce the second order derivatives (higher order derivatives) to first order derivatives (lower order derivatives), which is helpful in the sense that we have fewer constraints on the continuity of the test functions. The Edge Basis is suitable for vectorial PDEs (a PDE with an N dimensional vector as the answer), for which the weighting functions used for variational formulation (Whitney functions) are defined on the edges of the elements, with such properties as having a well defined curl. This is useful while applying any condition to a vector set. These basis functions are known to be inside the H (Curl) space in mathematics and have specific properties which make them suitable for solving specific equations (Zolgharni *et al.*, 2009b).
The nodal basis functions are not good candidates for the vector fields, as the BC often takes the form of a specification of only the part of the vector field which is tangent to the boundary. With nodal basis, physical constraints must be transformed into linear relationships between Cartesian coordinate and at the node where the boundary changes direction.
There are advantages in using the edge element basis approach for vectorial PDE's :

1. The edge elements basis imposes the continuity of the tangential components of the vector field which has the form of the BC in the physical problems (Maxwell's BC for continuity of fields)

2. The Dirichlet BC which specifies the values that a solution needs to take on along the boundary of the ROI can easily be imposed on this basis.

3. The interelement BC which specifies the values that a solution needs to take on the

boundaries between the elements are automatically obtained through the natural BC (The inter-element B.C. are similar to the boundary conditions imposed on Maxwell's equation at the boundary of a conducting material)

4. As the edge bases are chosen to be divergence free, non-physical solutions are completely and automatically eliminated.

We investigate the properties of the edge element basis in 3D as we use them as to solve the Helmholtz equation. In the following sections we carry out the weak formulation of Eq.(3.19) using the variational method carried out on the edge basis.

3.3 Variational formulation

Finite element methods are based on the variational formulation of partial differential equations. The weak formulation is the variational form of the PDE, which transforms it to a simpler form. That completely equivalent form is then used with the discretized model in numerical calculations. In most cases, the method transforms a second order PDE to an equivalent first order PDE, which is easier to solve.
We consider the test function $\mathbf{W}$ (weighting function used for variational calculation, which is the first order Whitney function), to be defined below :

$$\mathbf{W} = W_x\hat{x} + W_y\hat{y} + W_z\hat{z} \tag{3.21}$$

This test function can have a general form. Therefore, the formulations developed are general treatments. We multiply the $\mathbf{W}$ with the Eq.(3.19) from the right and integrate it over the volume Ω (the whole region) :

$$\iiint_{\Omega} \left(\mathbf{W} \cdot \nabla \times (\frac{1}{\mu}\nabla \times \mathbf{A}) - \kappa^2 \mathbf{W} \cdot \mathbf{A} \right) d\Omega = \iiint_{\Omega} \mathbf{W} \cdot \mathbf{J}_s d\Omega \tag{3.22}$$

Using the vector identity (Griffiths, 1999)

$$\mathbf{A} \cdot (\nabla \times \mathbf{B}) = (\nabla \times \mathbf{A}) \cdot \mathbf{B} - \nabla \cdot (\mathbf{A} \times \mathbf{B})$$

We can write :

$$\iiint_{\Omega}(\nabla \times \mathbf{W}) \cdot (\frac{1}{\mu}\nabla \times \mathbf{A})d\Omega =$$
$$\iiint_{\Omega} \kappa^2 \mathbf{W} \cdot \mathbf{A} d\Omega + \iiint_{\Omega} \mathbf{W} \cdot \mathbf{J}_s d\Omega + \underbrace{\iiint_{\Omega} \nabla \cdot \left[\mathbf{W} \times \frac{1}{\mu}\nabla \times \ \mathbf{A}\right] d\Omega}_{\text{Boundary Term}} \qquad (3.23)$$

The boundary term can be converted to a simpler surface integral with the aid of the divergence theorem

$$\iiint_{\Omega} \nabla \cdot \mathbf{A} \ d\Omega = \iint_{\Gamma} \mathbf{A} \cdot \hat{n} \ d\Gamma$$

where Γ is the boundary surface of volume Ω and also this vector identity :

$$(\mathbf{A} \times \mathbf{B}) \cdot \hat{n} = -\mathbf{A} \cdot (\hat{n} \times \mathbf{B})$$

where $\hat{n}$ is the normal unit vector. Then Eq.(3.23) will reduces to :

$$\iiint_{\Omega}(\nabla \times \mathbf{W}) \cdot (\frac{1}{\mu}\nabla \times \mathbf{A})d\Omega =$$
$$\iiint_{\Omega} \kappa^2 \mathbf{W} \cdot \mathbf{A} d\Omega + \iiint_{\Omega} \mathbf{W} \cdot \mathbf{J}_s d\Omega - \iint_{\Gamma} \mathbf{W} \cdot \left[\hat{n} \times \frac{1}{\mu}\nabla \times \mathbf{A}\right] d\Gamma \qquad (3.24)$$

Equation (3.24) is the weak formulation of the inhomogeneous Helmholtz equation and is subjected to boundary conditions in the following section. The first order derivatives are what make this equation easier to work with, compared with the Helmholtz equation which has second order derivatives.

3.4 Boundary conditions and the final equation

The whole domain Ω consists of a conducting region Ω_C and a non-conducting region Ω_N ($\Omega = \Omega_C \cup \Omega_N$). The conducting region also consists of different conducting materials : Ω_C^i, $i = 1, 2, \cdots, M$, so that $\Omega_C = \Omega_C^1 \cup \Omega_C^2 \cup \cdots \ \Omega_C^M$. The exciter and sensor are in Ω_N.
The magnetic and the electric field should be tangentially continuous at all the interfaces

of the material. In Maxwell's equations, the normal component of the magnetic field is also required to be continuous, but this not the case for the vectors satisfying the wave equation. The conditions are summarized in the following equation using proper vector notation (Zolgharni *et al.*, 2009b) :

$$\begin{aligned} [\hat{n} \times \frac{1}{\mu} \nabla \times \mathbf{A}] &= 0 \\ [\hat{n} \times \mathbf{A}] &= 0 \\ \hat{n} \times \mathbf{A} &= 0 \end{aligned} \tag{3.25}$$

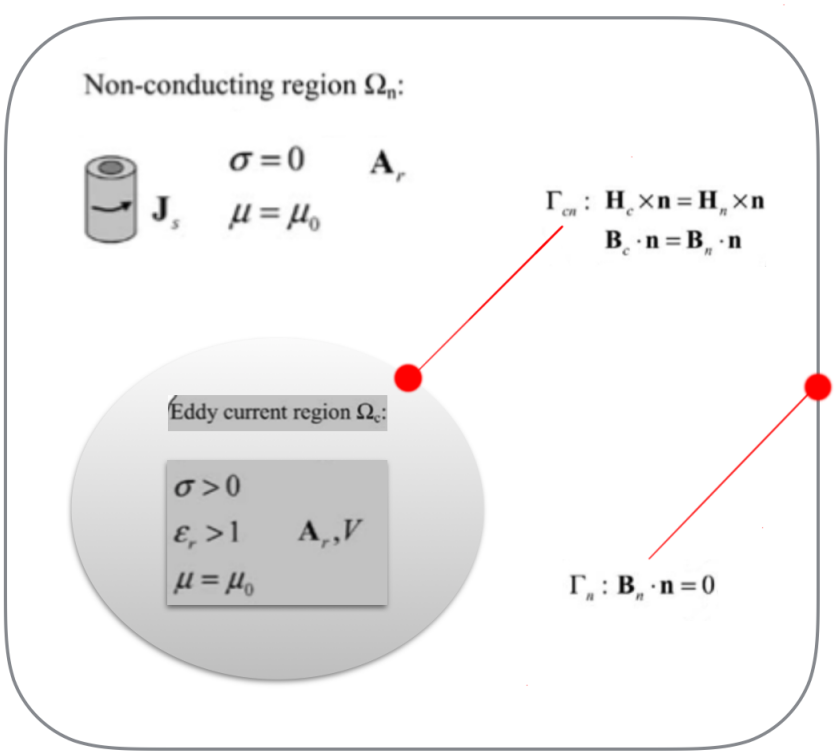

Figure 3.1 A schematic of all the forward problem boundary conditions.

In above equation, [...] denotes the difference and $\hat{n}$ is the outward normal vector on each boundary. Considering these boundary conditions, the last term on the right-hand side of Eq.(3.24) will be zero. A schematic of the forward problem boundary conditions is shown in Fig.(3.1).

3.5 Edge element basis in 3D

We need a basis set to express our vector field. In the presence of tetrahedral elements, Cartesian coordinates can be replaced by a more convenient basis, which handles the BC precisely and more straightforwardly. We discretize our volume with the first order tetrahedral elements as shown in Fig. (3.2). A tetrahedron has four nodes and six edges. Our test function basis, which is also used as the basis for our vector field $\mathbf{A}$ is defined on this tetrahedron.

$$\mathbf{A} = \sum_{m=1}^{6} e_m \mathbf{W}_m \tag{3.26}$$

The six redundant, unknown, vector edge elements $\mathbf{W}_m$ are associated with e_1, e_2, $\cdots$, e_6.

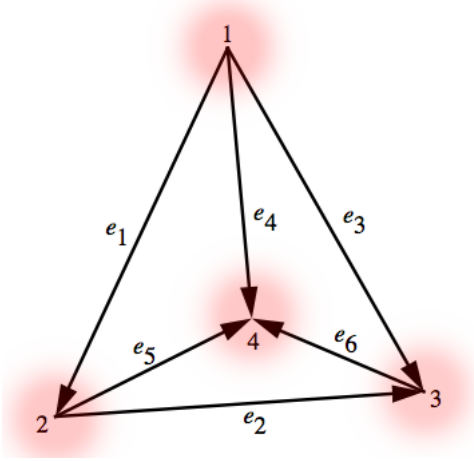

Figure 3.2 Defining the first order weighting function on a tetetrahedron and its edges.

Therefore, the total $\mathbf{A}$ associated with each element is given by Eq.(3.26).
The Whitney functions are used as the test function. There exist different classes whose degrees of freedom and other mathematical properties are known. We use a known Whitney function which is proper for solving the Helmholtz equation (Reddy *et al.*, 1994), as it satisfies vector identities which the solution to the Helmholtz equation needs to satisfy (for example being divergenceless).
Our function is a first order Whitney function which has 6 degrees of freedom. From the same class of functions, second order Whitney function have 20 degrees of freedom which provide more computation accuracy at the cost of more complexity of formulation.

Edge, m	Node i	Node j
1	1	2
2	2	3
3	1	3
4	1	4
5	2	4
6	3	4

Table 3.1 Numbering of the edges for a single element.

We consider $\mathbf{W}_m$, the first order Whitney function with six vectors as edges which are defined by :

$$\mathbf{W}_m = L_m(\alpha_{ti}\nabla\alpha_{tj} - \alpha_{tj}\nabla\alpha_{ti}), \tag{3.27}$$

where m is the edge number, i and j stand for nodes that are connecting the edge m, L_m being the length of the edge m, and α_{ti} and α_{tj} being the simplex coordinates associated with nodes i and j (subscription t denote tangential). The connection between the edge number m and i and j indexes is presented in Table (3.1).
The simplex coordinates (volume coordinates) are given by

$$\alpha_{t1} = \frac{V_1}{V}, \tag{3.28}$$

$$\alpha_{t2} = \frac{V_2}{V}, \tag{3.29}$$

$$\alpha_{t3} = \frac{V_3}{V}, \tag{3.30}$$

$$\alpha_{t4} = \frac{V_4}{V}, \tag{3.31}$$

which V is the volume of the tetrahedron and it is given by :

$$V = \frac{1}{6}\begin{vmatrix} 1 & x_1 & y_1 & z_1 \\ 1 & x_2 & y_2 & z_2 \\ 1 & x_3 & y_3 & z_3 \\ 1 & x_4 & y_4 & z_4 \end{vmatrix}, \tag{3.32}$$

The other $V_1,\cdots,\ V_4$ are defined as follows :

$$V_1 = \frac{1}{6}\begin{vmatrix} 1 & x & y & z \\ 1 & x_2 & y_2 & z_2 \\ 1 & x_3 & y_3 & z_3 \\ 1 & x_4 & y_4 & z_4 \end{vmatrix}, \tag{3.33}$$

$$V_2 = \frac{1}{6}\begin{vmatrix} 1 & x_1 & y_1 & z_1 \\ 1 & x & y & z \\ 1 & x_3 & y_3 & z_3 \\ 1 & x_4 & y_4 & z_4 \end{vmatrix}, \tag{3.34}$$

$$V_3 = \frac{1}{6}\begin{vmatrix} 1 & x_1 & y_1 & z_1 \\ 1 & x_2 & y_2 & z_2 \\ 1 & x & y & z \\ 1 & x_4 & y_4 & z_4 \end{vmatrix}, \tag{3.35}$$

$$V_4 = \frac{1}{6}\begin{vmatrix} 1 & x_1 & y_1 & z_1 \\ 1 & x_2 & y_2 & z_2 \\ 1 & x_3 & y_3 & z_3 \\ 1 & x & y & z \end{vmatrix}. \tag{3.36}$$

For any node (i= 1, 2, 3, 4), α_{ti} is given by

$$\alpha_{ti} = \frac{a_{ti} + b_{ti}x + c_{ti}y + d_{ti}z}{6V} \tag{3.37}$$

where the a_{ti}, b_{ti}, c_{ti} and d_{ti} are cofactors picked from $V_1,\cdots,\ V_4$ for $m = 1, \cdots 6$. From Eqs.(3.27) and (3.37), We can find $\mathbf{W}_m$:

$$\begin{aligned} \mathbf{W}_m &= \frac{L_m}{36V^2}[(A_{xm} + B_{xm}y + C_{xm}z)\hat{x} \\ &\quad +(A_{ym} + B_{ym}x + C_{ym}z)\hat{y} \\ &\quad +(A_{zm} + B_{zm}x + C_{zm}y)\hat{z}] \end{aligned} \tag{3.38}$$

where :

$$
\begin{aligned}
A_{xm} &= a_{ti}b_{tj} - a_{tj}b_{ti} \\
B_{xm} &= c_{ti}b_{tj} - c_{tj}b_{ti} \\
C_{xm} &= d_{ti}b_{tj} - d_{tj}b_{ti} \\
A_{ym} &= a_{ti}c_{tj} - a_{tj}c_{ti} \\
B_{ym} &= b_{ti}c_{tj} - b_{tj}c_{ti} = -B_{xm} \\
C_{ym} &= d_{ti}c_{tj} - d_{tj}c_{ti} \\
A_{zm} &= a_{ti}d_{tj} - a_{tj}d_{ti} \\
B_{zm} &= b_{ti}d_{tj} - b_{tj}d_{ti} = -C_{xm} \\
C_{zm} &= c_{ti}d_{tj} - c_{tj}d_{ti} = -C_{ym}
\end{aligned} \tag{3.39}
$$

It cane be verified that the $\mathbf{W}_m$ will satisfy the following conditions :

$$
\hat{t}_m \cdot \mathbf{W}_m = \begin{cases} 1 & \text{edge } m \\ 0 & \text{otherwise} \end{cases} \tag{3.40}
$$

where $\hat{t}_m$ is a unit vector along the edge (orthonormality condition).
Expressing $\mathbf{A}$ in the same basis of weighting function $\mathbf{W}_m$ (Eq.(3.26)) and substitute in Eq.(3.24) and considering the boundary conditions, we have for n= 1, $\cdots$, 6 :

$$
\begin{aligned}
&\sum_{m=1}^{6} \iiint_{\blacktriangle} \frac{1}{\mu}\Big((\nabla \times \mathbf{W}_m) \cdot (\nabla \times \mathbf{W}_n)\Big) e_m d\Omega \\
&-\sum_{m=1}^{6} \iiint_{\blacktriangle} \kappa_j^2 \Big(\mathbf{W}_m \cdot \mathbf{W}_n\Big) e_m d\Omega = \iiint_{\blacktriangle} \Big(\mathbf{W}_n \cdot \mathbf{J}_s\Big) d\Omega
\end{aligned} \tag{3.41}
$$

The integration is over the volume of one tetrahedron. In matrix form (shown with brackets) as Eq. (3.43) represent 6 equations for each n, it can be written as an eigenvalue equation for one tetrahedron :

$$
\Big(\Big[Z_{el}\Big] - \kappa_j^2 \Big[T_{el}\Big]\Big)\Big[e\Big] = \Big[J_{el}\Big] \tag{3.42}
$$

where

$$\Big[Z_{el}\Big] = \iiint_{\blacktriangle} \frac{1}{\mu}\Big((\nabla \times \mathbf{W}_m) \cdot (\nabla \times \mathbf{W}_n)\Big) d\Omega$$
$$\Big[T_{el}\Big] = \iiint_{\blacktriangle} \Big(\mathbf{W}_m \cdot \mathbf{W}_n\Big) d\Omega$$
$$\Big[J_{el}\Big] = \iiint_{\blacktriangle} \Big(\mathbf{W}_m \cdot \mathbf{J}_s\Big) d\Omega. \tag{3.43}$$

Solving Eq.(3.42), which is an eigenvalue equation, yields the sets of [e] needed in Eq.(3.26) and specifies $\mathbf{A}$.

Further analytic rearrangement of Eq.(3.43) is a necessity for their implementation in numerical calculations. $\Big[Z_{el}\Big]$ can be written, using the form of $\mathbf{W}_m$ introduced in Eq.(3.38) as

$$\Big[Z_{el}\Big] = \frac{L_m L_n}{\mu(18V^2)^2} \times$$
$$\Big(C_{zm}C_{zn} - C_{zm}C_{yn} - C_{ym}C_{zn} + C_{ym}C_{yn}$$
$$C_{xm}C_{xn} - C_{xn}B_{zn} - B_{zm}C_{xn} + B_{zm}B_{zn}$$
$$B_{ym}B_{yn} - B_{ym}B_{xn} - B_{xm}B_{yn} + B_{xm}B_{xn}\Big). \tag{3.44}$$

Further, in order to implement $\Big[T_{el}\Big]$ in our numerical calculations, we have to carry out integrals which contain terms like x, xy, x^2. These terms with their respective coefficient should be integrated over the volume of one element. These integrals can be calculated according to the following relations which are each calculated using the geometrical properties of a tetrahedron and the nodes' coordinates. The integral is taken over the volume of an element

(tetrahedron).

$$\iiint_{\blacktriangle} x\ dxdydz = \sum_{i=1}^{4} x_i = \bar{x}_{tet}$$

$$\iiint_{\blacktriangle} y\ dxdydz = \sum_{i=1}^{4} y_i = \bar{y}_{tet}$$

$$\iiint_{\blacktriangle} z\ dxdydz = \sum_{i=1}^{4} z_i = \bar{z}_{tet}$$

$$\iiint_{\blacktriangle} xy\ dxdydz = \sum_{i=1}^{4} x_i y_i + 16\bar{x}_{tet}\bar{y}_{tet}$$

$$\iiint_{\blacktriangle} yz\ dxdydz = \sum_{i=1}^{4} y_i z_i + 16\bar{y}_{tet}\bar{z}_{tet}$$

$$\iiint_{\blacktriangle} xz\ dxdydz = \sum_{i=1}^{4} x_i z_i + 16\bar{x}_{tet}\bar{z}_{tet}$$

$$\iiint_{\blacktriangle} x^2\ dxdydz = \sum_{i=1}^{4} x_i^2 + 16\bar{x}_{tet}^2$$

$$\iiint_{\blacktriangle} y^2\ dxdydz = \sum_{i=1}^{4} y_i^2 + 16\bar{y}_{tet}^2$$

$$\iiint_{\blacktriangle} z^2\ dxdydz = \sum_{i=1}^{4} z_i^2 + 16\bar{z}_{tet}^2 \tag{3.45}$$

Then $\left[T_{el}\right]$ can be written as

$$\left[T_{el}\right] = \frac{L_m L_n}{1296V^3} \sum_{k=1}^{10} I_k \tag{3.46}$$

Where indexed I_k are as follows :

$$
\begin{aligned}
I_1 &= (A_{xm}A_{xn} + A_{ym}A_{yn} + A_{zm}A_{zn}) \\
I_2 &= (A_{ym}B_{yn} + A_{yn}B_{ym} + A_{zm}B_{zn} + A_{zn}B_{zm})\bar{x}_{tet} \\
I_3 &= (A_{xm}B_{xn} + A_{xn}B_{xm} + A_{zm}C_{zn} + A_{zn}C_{zm})\bar{y}_{tet} \\
I_4 &= (A_{xm}C_{xn} + A_{xn}C_{xm} + A_{ym}C_{yn} + A_{yn}C_{ym})\bar{z}_{tet} \\
I_5 &= \frac{1}{20}(B_{zm}C_{zn} + B_{zn}C_{zm})\left(\sum_{i=1}^{4} x_i y_i + 16\bar{x}_{tet}\bar{y}_{tet}\right) \\
I_6 &= \frac{1}{20}(B_{xm}C_{xn} + B_{xn}C_{xm})\left(\sum_{i=1}^{4} y_i z_i + 16\bar{y}_{tet}\bar{z}_{tet}\right) \\
I_7 &= \frac{1}{20}(B_{ym}C_{yn} + B_{yn}C_{ym})\left(\sum_{i=1}^{4} x_i z_i + 16\bar{x}_{tet}\bar{z}_{tet}\right) \\
I_8 &= \frac{1}{20}(B_{ym}B_{yn} + B_{zn}B_{zm})\left(\sum_{i=1}^{4} x_i^2 + 16\bar{x}_{tet}^2\right) \\
I_9 &= \frac{1}{20}(B_{xm}B_{xn} + C_{zn}C_{zm})\left(\sum_{i=1}^{4} y_i^2 + 16\bar{y}_{tet}^2\right) \\
I_{10} &= \frac{1}{20}(C_{xm}C_{xn} + C_{yn}C_{ym})\left(\sum_{i=1}^{4} z_i^2 + 16\bar{z}_{tet}^2\right)
\end{aligned} \tag{3.47}
$$

Each element of the (6×1) current matrix $\left[J_{el}\right]$ can be calculated using the inner product of current vector

$$\mathbf{J}_s = [J_x, J_y, J_z] \tag{3.48}$$

and the W_m which is given by Eq.(3.38). The product is the value of the current on each edge of the element. If the current components are not a function of coordinates, the result can be written as :

$$\left[J_{el}\right] = \frac{L_m}{36V}\sum_{i=1}^{4} k_i, \tag{3.49}$$

where

$$
\begin{aligned}
k_1 &= (A_{xm}J_x + A_{ym}J_y + A_{zm}J_z) \\
k_2 &= (B_{ym}J_y + B_{zm}J_z)\bar{x}_{tet} \\
k_3 &= (B_{xm}J_x + C_{xm}J_z)\bar{y}_{tet} \\
k_4 &= (C_{xm}J_x + C_{ym}J_y)\bar{z}_{tet}
\end{aligned} \tag{3.50}
$$

Knowing $\left[Z_{el}\right]$ and $\left[T_{el}\right]$, we can specify $\left[e\right]$ which specifies $\mathbf{A}$ on each element. After finding $\mathbf{A}$, the average $\mathbf{B}$ field normal to the surface defined by the edges can be obtained from the voltage that would be induced in a virtual one turn detection coil along the constituent edges and is calculated by line integration over the constituent edges of the $\mathbf{A}$ vector :

$$V = \oint \mathbf{E}.dl = -\imath\omega \oint \mathbf{A}.dl \tag{3.51}$$

3.6 Assembling the global matrix

Eq.(3.42) and other subsequent matrix equations developed up to this point may be solved for one element. Therefore, these equations are local. Connecting the elements requires a matrix assembly to turn Eq.(3.42) into a global equation. This assembly will preserve the form of the equation. In order to get the global matrix, we have to connect all the elements and also apply inter-element BC. Every edge is labeled from 1 to 6 (m subscript).
In order to assemble the global matrix equation, which has the same form as Eq.(3.42), we should have two maps. Any two connected nodes will give us one edge. So the first map is the map between the connected nodes (which two nodes are connected). The second map will specify which nodes belong to a given element.
We start by assigning each edge in the mesh a global number and then remove the duplicates (If one edge is common to two neighboring elements, it should be counted once). To get a sense of how the global matrix $\mathbf{Z}$ is calculated, suppose that the edge numbering process has resulted in edges with global numbering of (59,60,63,144,146,151) for element number 1. Then the matrix element $Z_{1,3}$ in $\left[Z_{el}\right]$ is positioned in $\mathbf{Z}_{59,63}$ in the global matrix. As $\left[Z_{el}\right]$ is a symmetric matrix, $\mathbf{Z}_{63,59}$ in the global matrix will have the same value. So the global matrix $\mathbf{Z}$ is also a symmetric matrix. The procedure is the same for building the global $\mathbf{T}$

matrix. In this map, the form of the Eq.(3.42) is preserved :

$$(\mathbf{Z} - \kappa_j^2 \mathbf{T})\mathbf{e} = \mathbf{J} \tag{3.52}$$

This equation includes the complete formulation and its boundary conditions. In Eq.(3.52), the dimension of $\mathbf{e}$ and $\mathbf{J}$ is the number of the edges. It should be stated that κ_j in Eq.(3.52) is only multiplied by the matrix elements in $\mathbf{T}$ which correspond to the voxel j. However as we need to take its derivative for calculation of the sensitivity matrix elements for each j voxel, it was not included in the definition of the $\mathbf{T}$ matrix.
In order to show the fact our developed formulation with our specific temporal gauge will result in the correct calculation of the magnetic field $\mathbf{B}$ after the treatments of the Helmholtz equation. In the following section, we have simulated examples that analytic solution exist for verification.

3.7 Validation of the forward problem formulation

In order to verify the forward problem formulation and check the numerical accuracy of the method, we have reproduced the results for some geometries for which analytical solutions exist and are well-known. As a benchmark test, calculation of the magnetic field $\mathbf{B}$ and the vector potential $\mathbf{A}$ for a long straight wire and for a pair of Helmholtz coils are performed and compared to the analytical solution.
In general, visualization of a 3D vector field, capable of showing both magnitude and direction is challenging. Therefore, the following graphing method was implemented for better illustration. For vectors of the same length, the width of the arrows shows their magnitude. For vectors of the same width, the length of the arrows shows their magnitude.

3.7.1 Long straight wire

It is well known that for an infinitely long wire, the magnetic field $\mathbf{B}$ in free space forms concentric circles around the wire. The magnetic potential vector $\mathbf{A}$ mimics the direction of the current (Griffiths, 1999) in Coulomb gauge ($\nabla \cdot \mathbf{A} = 0$). Figures (3.3) and (3.4) show the numerically calculated results for the vector potential $\mathbf{A}$ and the magnetic field $\mathbf{B}$, respectively for this case, in the temporal gauge ($V = 0$).
The magnetic vector potential of a finite but very long straight wire of length L carrying a

steady current I can be found from :

$$\mathbf{A}(r) = \frac{\mu_0}{4\pi} I \ln\left(\frac{L}{r}(1+\sqrt{1+(\frac{r}{L})^2})\right)\hat{z} \tag{3.53}$$

where r is the radial distance from the wire. The Eq.(3.53) specify the Z component of the vector potential. The X and Y components cancel out due to the cylindrical symmetry.
The red line in the middle of the Fig.(3.3) and Fig.(3.4) shows the current flow. The bottom and top divergence of vectors in Fig.(3.4) is the result of the fact that the current appears suddenly in ROI as a source and disappears in a sink, as a real wire has a finite length, and the end effects on field lines are not negligible.
The numerical treatment of the Helmholtz equation for a ROI for a straight wire parallel to the Z axis surrounded by air in the middle, will produce the familiar results presented ion page 238 of (Griffiths, 1999) textbook. Therefore, as it can be seen in Fig.(3.4), using the temporal gauge does not change the direction of $\mathbf{A}$. However the gradient which adds to $\mathbf{A}$ in Eq.(3.14) to take it to temporal gauge changes in its magnitude. Therefore the values of $\mathbf{A}$ are not equal to those in Coulomb gauge.

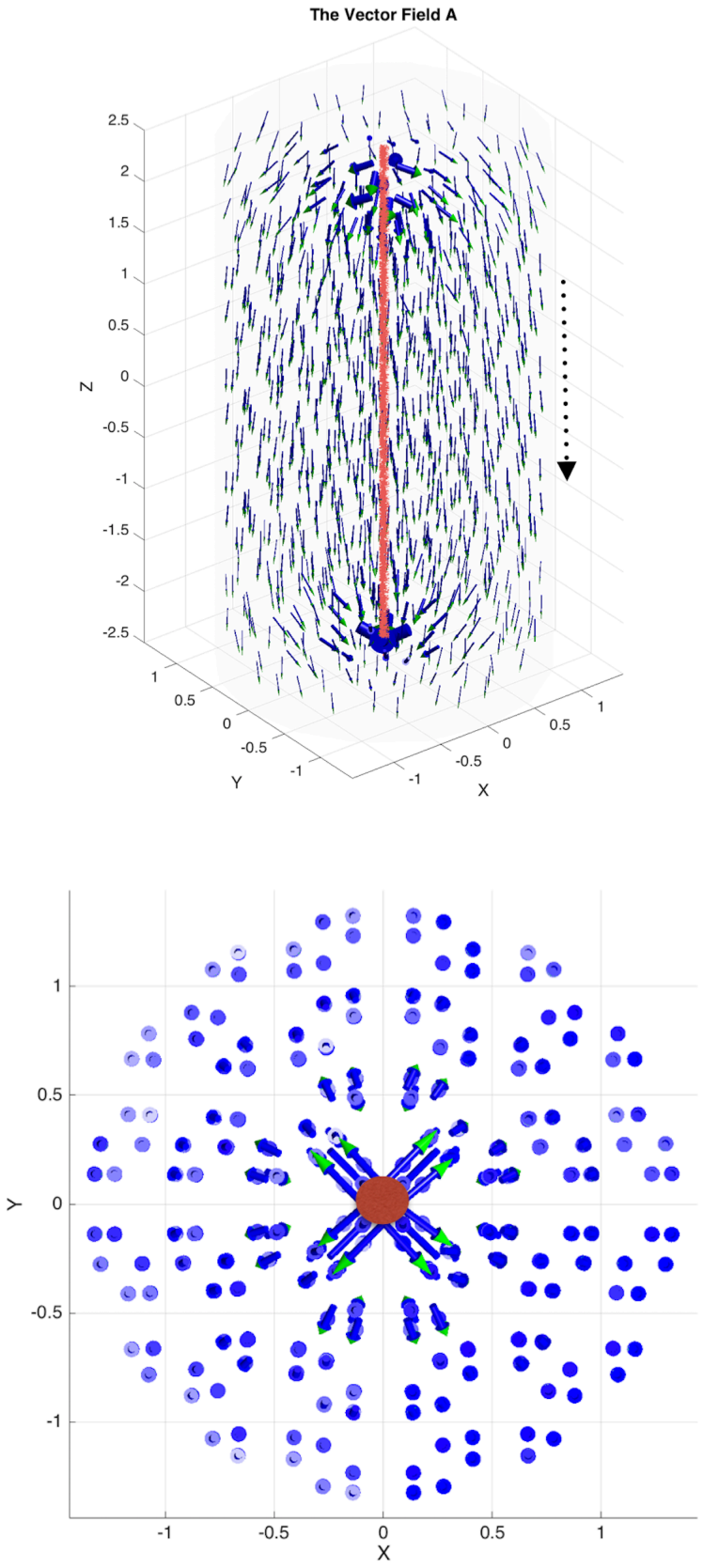

Figure 3.3 The magnetic vector potential, **A** vector field numerically calculated in temporal gauge for a straight wire in 3D (Side view on the top - Top view on the bottom).

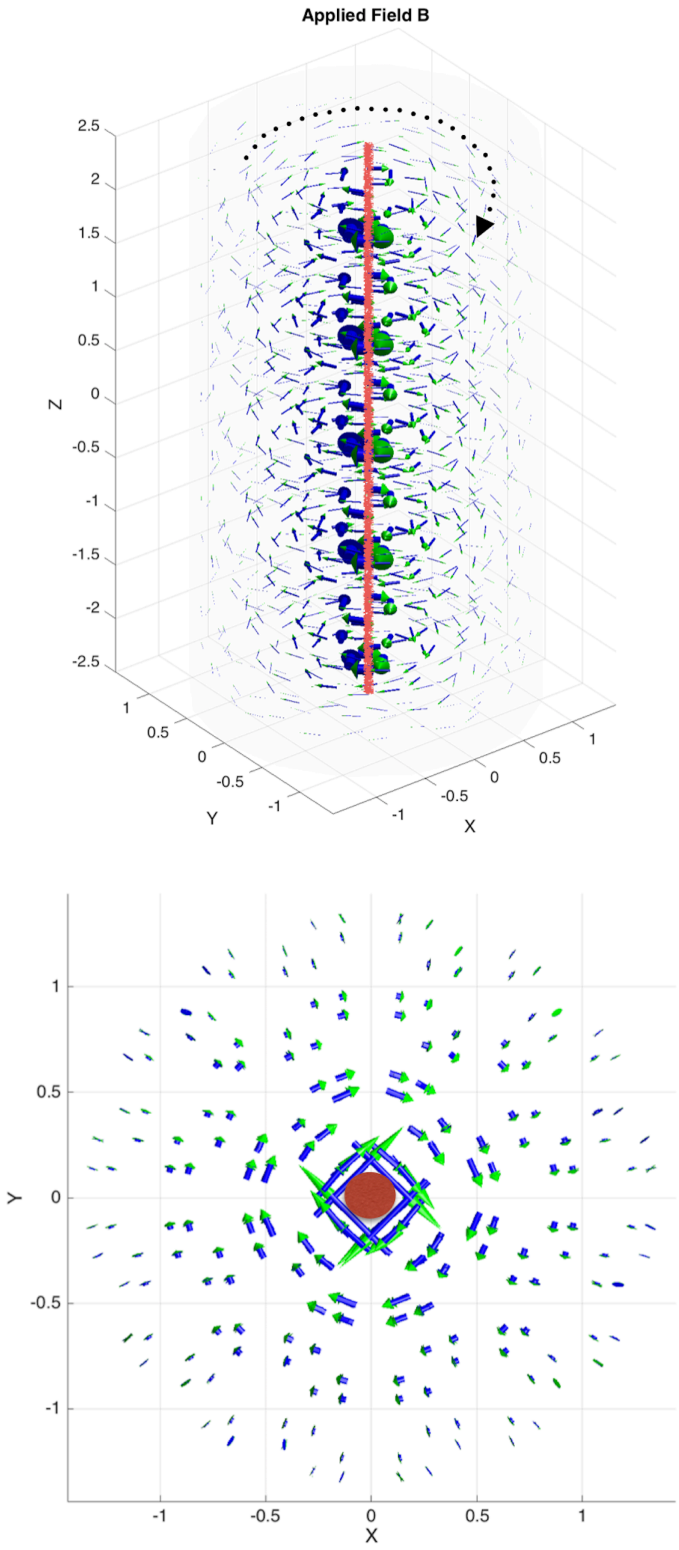

Figure 3.4 Magnetic field, **B** vector field numerically calculated for a straight wire in 3D (Side view on the top - Top view on the bottom).

The values for Eq.(3.53) are calculated in the Coulomb gauge. The vector field $\mathbf{A}$, no matter which gauge is chosen, allows us to us find the $\mathbf{B}$ field. In the numerical case, the gauge is temporal as we discussed. Calculations in both gauges result in the same magnetic field values. For 1 ampere of current, the analytically calculated magnetic field using :

$$\mathbf{B}_\phi = \frac{\mu_0 I}{2\pi r} \tag{3.54}$$

is compared with the numerically calculated field in Fig.(3.5). The average difference is 0.016 % of the value given by the formula.

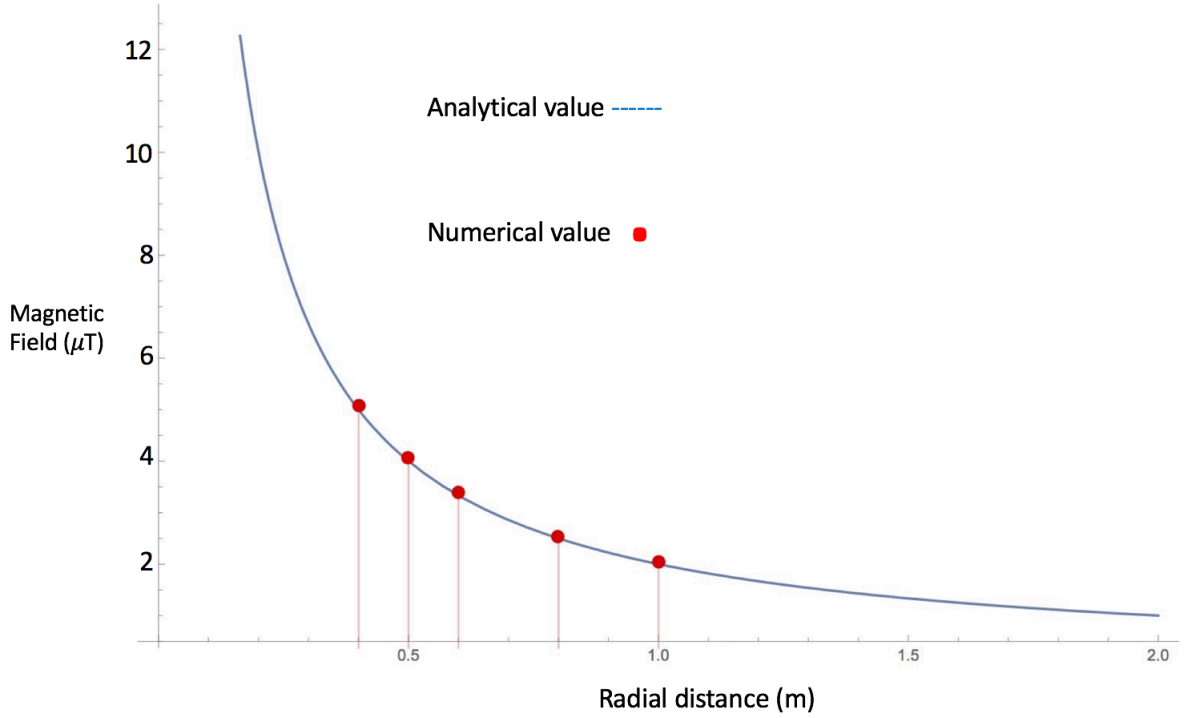

Figure 3.5 The analytically calculated magnetic field of a wire (blue) and the numerically calculated magnetic field of a wire computed at 5 points (red). The average difference is 0.01 % of the analytically calculated value.

This method for comparison of fields was used at larger distances from the wire, to assure that we are far enough from the wire ends so that their effect on the field is neglected. As this model shows a sudden emergence of current in the ROI, the verification for the magnitude of the field is limited to areas less affected by the disturbance.

3.7.2 Helmholtz coils

For validating the primary field produced by current carrying coils, we use the Helmholtz coils configuration which is known to produce a uniform magnetic vector field **B** between two coils. The analytical expression for the magnetic field of a current carrying coil, only for a point along the axis passing through its center is given by :

$$\mathbf{B}(z) = \frac{\mu_0 I R^2}{2(z^2 + R^2)^{\frac{3}{2}}} \tag{3.55}$$

where R is the radius of the coil. The field for two Helmholtz coils along their central axis can be calculated using this expression for the field of each coil. Equation (3.55) has been used to produce the graph in Fig. (3.6).

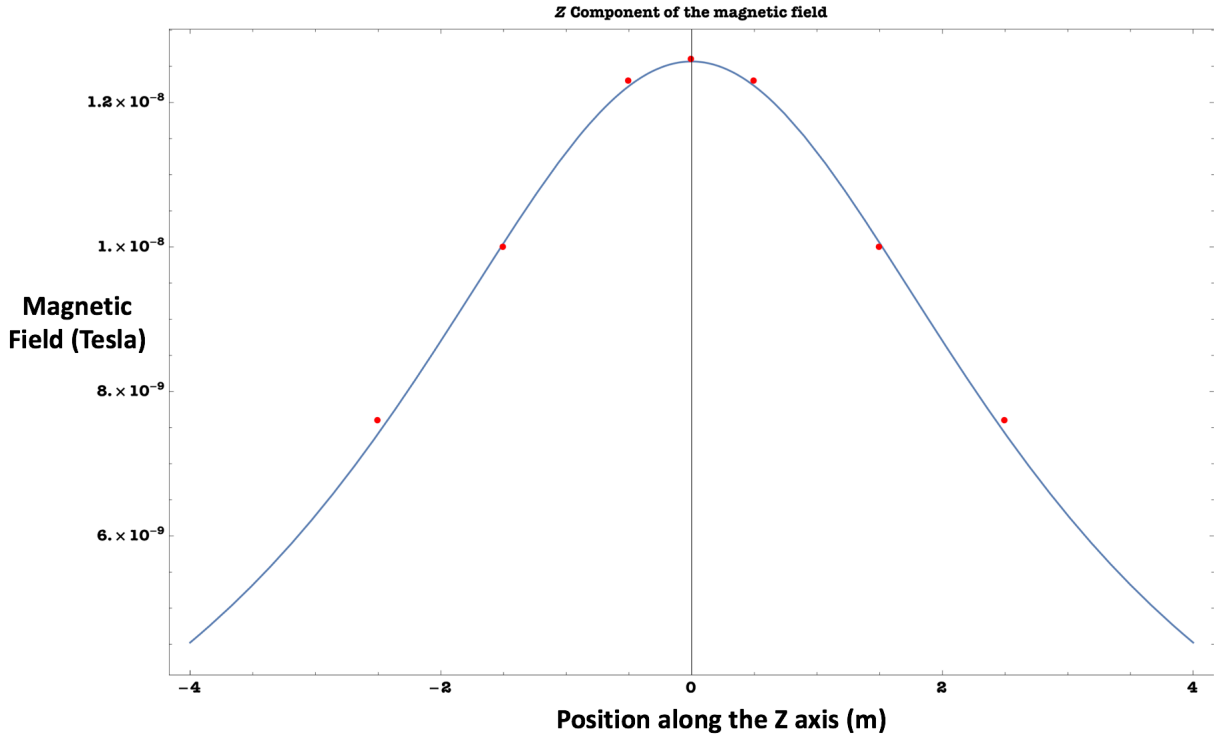

Figure 3.6 The magnetic field $\mathbf{B}_z$ calculated using Eq.(3.55) for two coils located at $z = 0.5$ (coils 4) and $z = -0.5$ (coils 3). The indicated values are the points used for validation of the numerical calculations. The points between these two heights are the points with almost uniform magnetic field.

Figures (3.7) and (3.8) shows the interpolated surface for the z component of the magnetic field $\mathbf{B}$, as well as the points used for this interpolation at two different heights. Figure (3.7) is the magnetic field value $\mathbf{B}_z$calculated at $z = 0$ exactly between the two coils. Uniform field for the area exactly between the coils ($z = 0$) is observed as expected. The numerically calculated values shows 0.01 % difference with the analytical value calculated at $z = 0$. Figure (3.8) is the magnetic field value calculated at $z = 1.5$ above the two coils. The value of the magnetic field has dropped as the analytical model predicted and the field is no longer uniform at this height.

The $\mathbf{A}$ vector will mimic the current direction (Griffiths, 1999). Figures (3.9) and (3.10) show the simulated results for the case of the currents in coils 3 and 4. The vectors' orientations show the direction of $\mathbf{B}$ or $\mathbf{A}$ fields. As expected, there exists a uniform magnetic field region in the middle of the cylinder. The field streamlines are parallel in the middle, as shown in the top view. The $\mathbf{A}$ vector however forms concentric circles in the same direction as the current and decreases in value as we go toward the center of the coils.

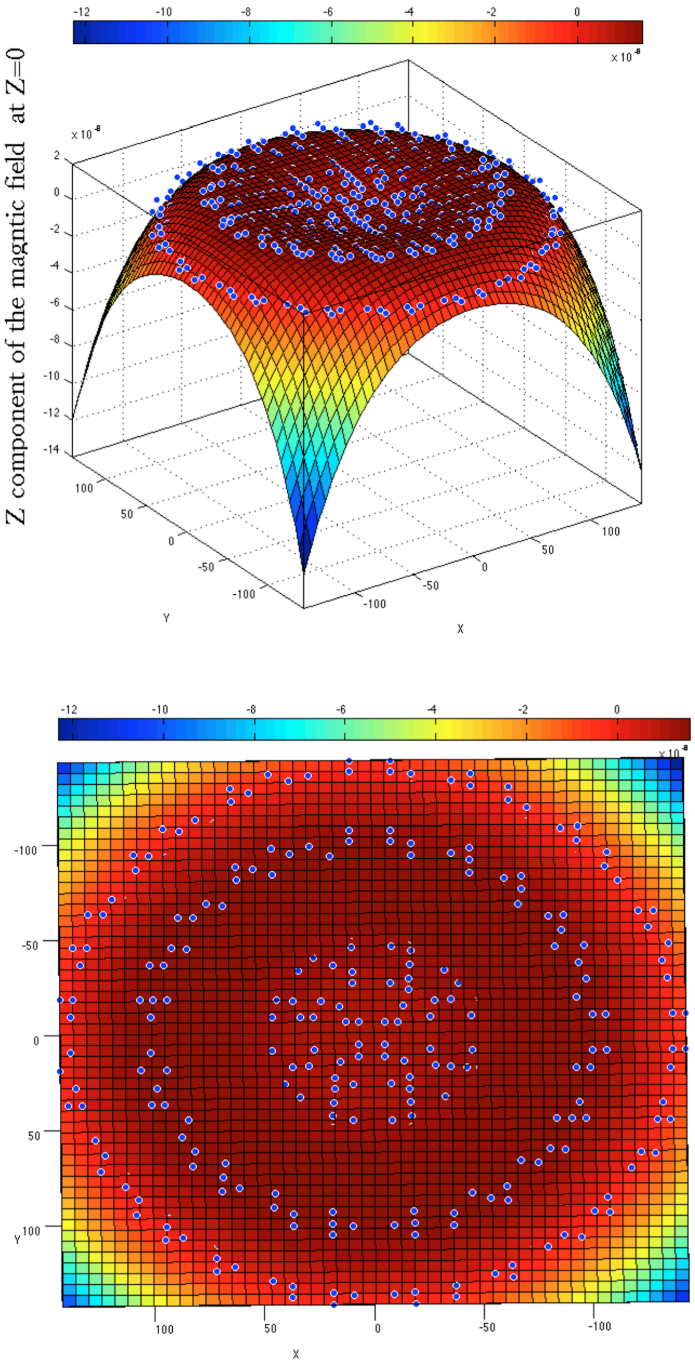

Figure 3.7 The magnetic field $\mathbf{B}_z$ calculated at $z = 0$ using finite element method for two coils located at $z = 0.5$ (coils 4) and $z = -0.5$ (coils 3). The field is uniform exactly at $z = 0$ as expected (Side view on the top - Top view on the bottom).

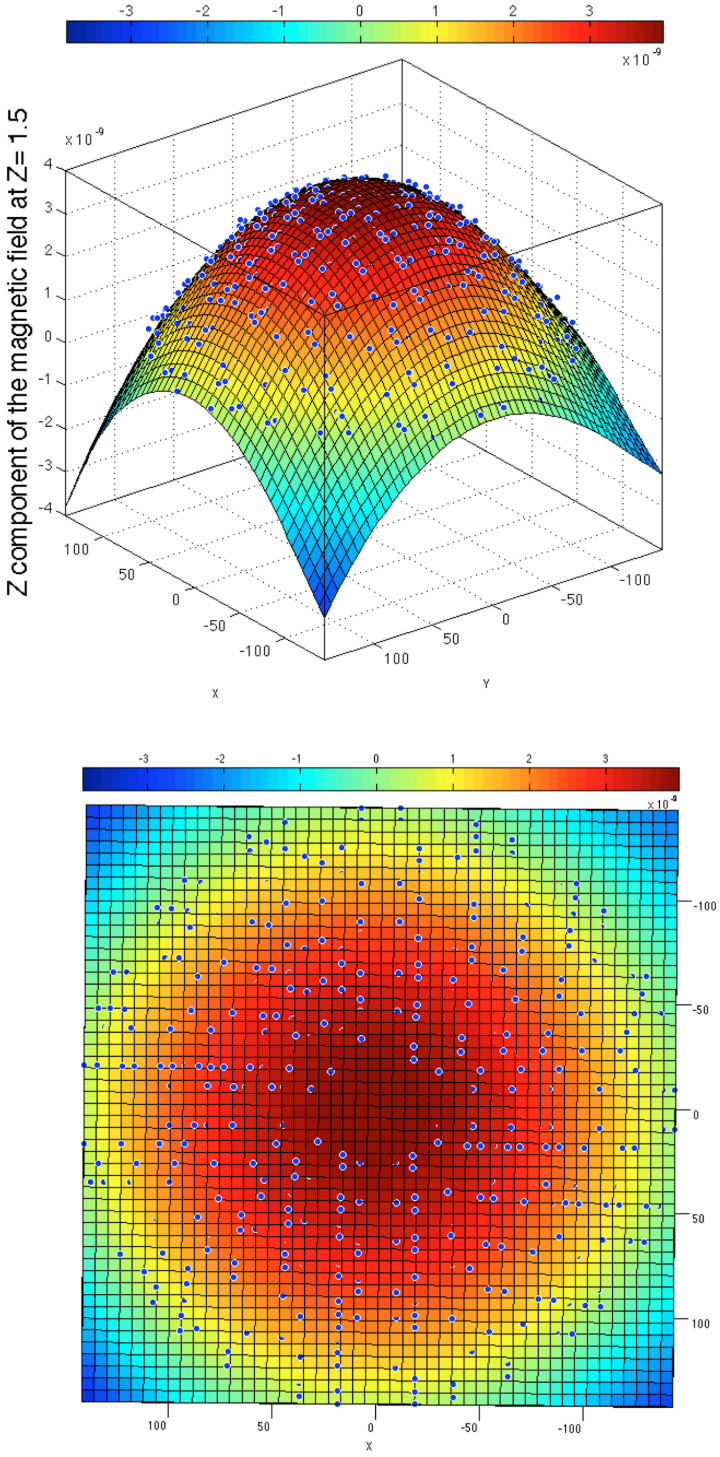

Figure 3.8 The magnetic field $\mathbf{B}_z$ calculated at $z = 1.5$ using finite element method for two coils located at $z = 0.5$ (coils 4) and $z = -0.5$ (coils 3). The field is nonuniform as we go farther vertically from the coils (Side view on the top - Top view on the bottom).

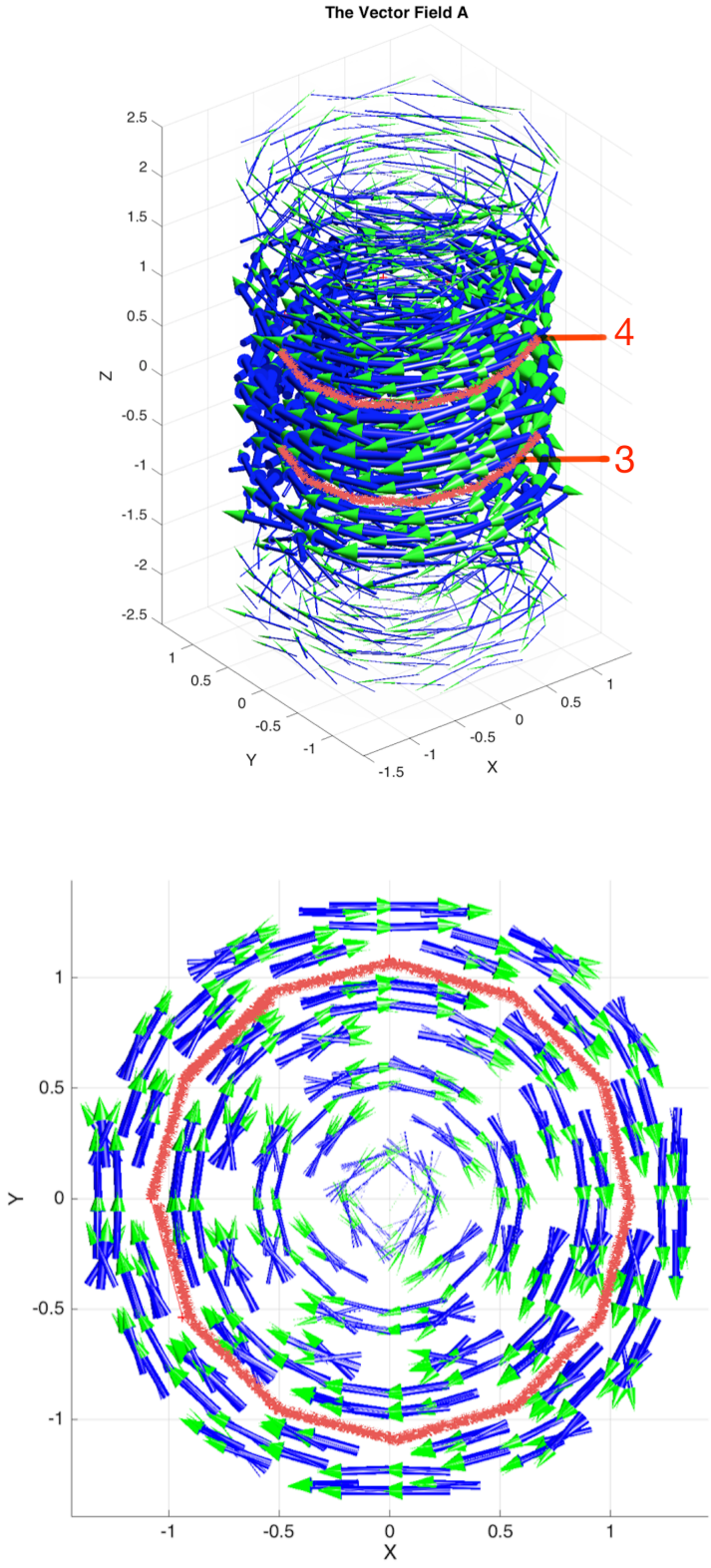

Figure 3.9 The numerically calculated magnetic potential, **A** vector field in temporal gauge for two loops of wire in 3D (Side view on the top - Top view on the bottom). The top view shows that circles are concentric.

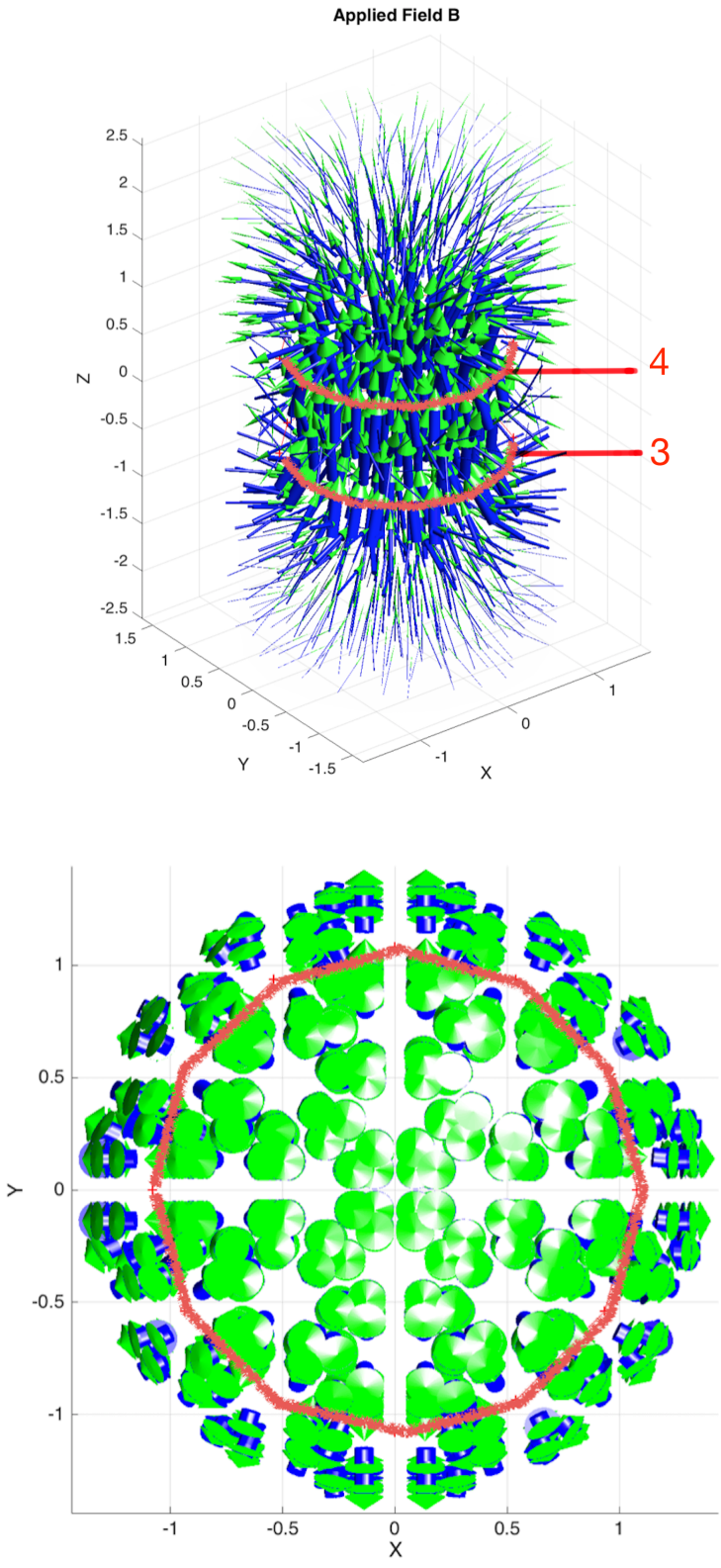

Figure 3.10 The numerically calculated magnetic field, **B** vector field for two loops of wire (Helmholtz coils) in 3D (Side view on the top - Top view on the bottom).

3.7.3 Summary

In summary, in the forward problem we seek to solve Eq.(3.19) in the ROI. In order to carry out that task, our volume is discretized in tetrahedral shaped elements and Eq.(3.19) is written as Eq.(3.52) in matrix form. Once **A** is obtained, the magnetic field **B** at the position of the detectors can be obtained. It can then be used for image reconstruction. With a working forward problem, we are one step away from the image reconstruction. That step is extracting the sensitivity matrix or Jacobian. It tells us how sensitive is the calculated field to all passive electromagnetic properties. The sensitivity matrix shows us how the field changes everywhere if we change the conductivity or permitivity or permeability of an element. Methods and steps of extraction of the sensitivity matrix are discussed in Chapter (4).

3.8 Visualization of the eddy currents

Finally, we consider a thick disk with conductivity of 1.09 Sm^{-1} with a current running in the two inducting coils (1 and 5) above and below of the disk, at different vertical distances (height) from the disk (The disk is positioned between 3 and 4). The conduction current also known as eddy($\sigma\mathbf{E}$) , the displacement current ($\imath\omega\epsilon\mathbf{E}$), the induced secondary magnetic field, **B** and its corresponding **A** are shown in the following figures.
Figure (3.11) shows the thick disk and its induced conduction current ($\sigma\mathbf{E}$). As may be seen in the figure, the density of current is highest on the surface and reduces as we go toward the center due to the skin effect. The information used in the calculation of the eddy currents density may be used to calculate the skin depth using Eq (3.18). The density of current at the bottom the disk is much lower than at the top. This is a result of the asymmetry of the coils distances. These two figures show that we can calculate both eddy current and displacement current and verify that they are not in phase.
Figure (3.12) shows the displacement current ($\imath\omega\epsilon\mathbf{E}$) in the thick disk. As may be seen in the figure, the density of current is less than the conduction current on the surface as we are in a regime with low ω in RF frequencies (50 kHz) and as $\omega\epsilon/\sigma \ll 1$ (we chose the conductivity of the disk to be around biological conductivity). It can be seen that like the conduction current, it also reduces as we go toward the center. The skin depth can be calculated with Eq.(3.18). Moreover, as expected, the density of the current on the bottom the disk is much lower than at the top. The vector potential, **A** and the magnetic field, **B** are shown in Fig.(3.13) and Fig.(3.14) from different view points.

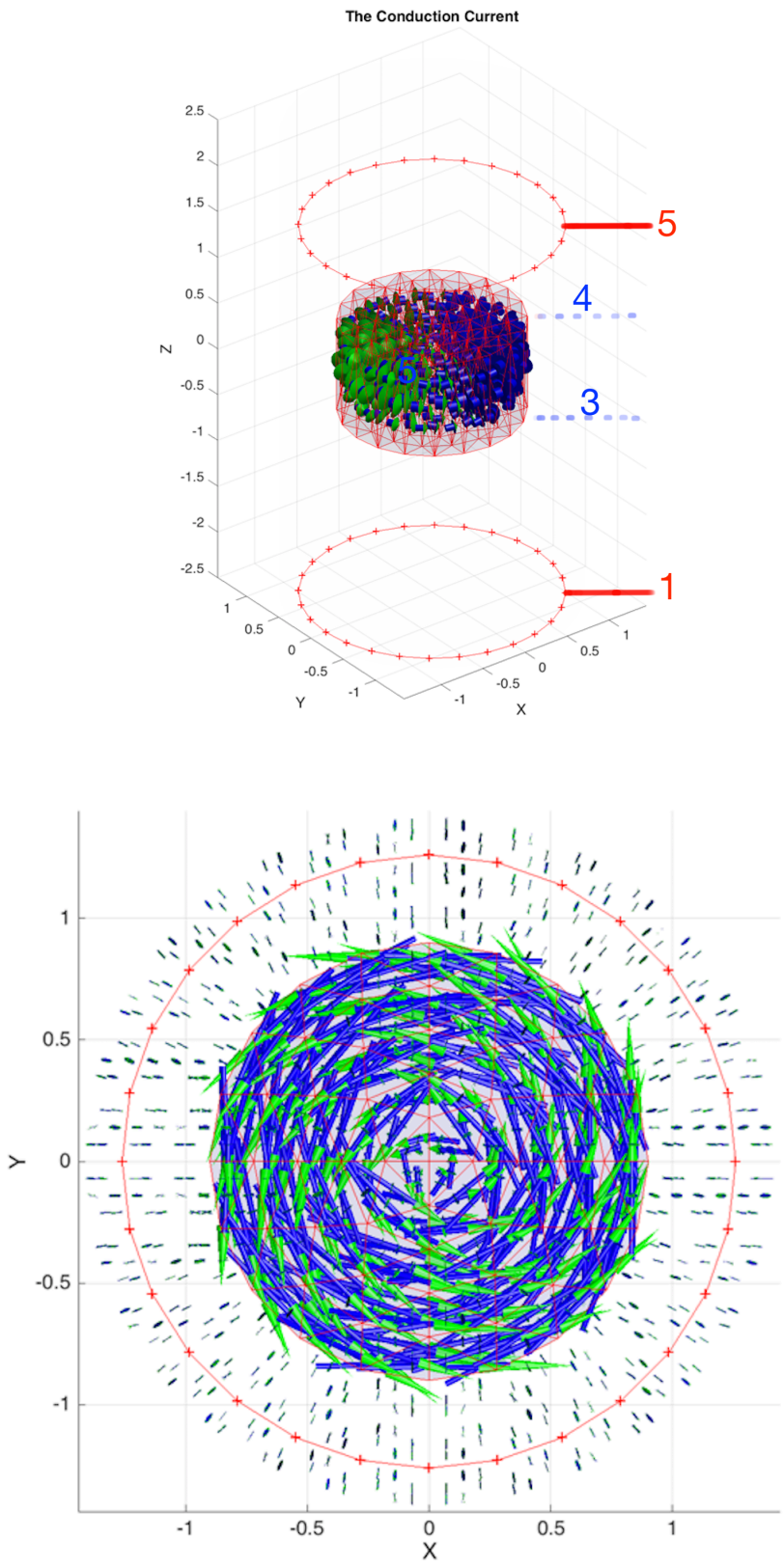

Figure 3.11 Conduction currents produced on a disk as the result of inductions from two coils numerically calculated at different vertical distances from the top and bottom surfaces (Side view on the top - Top view on the bottom).

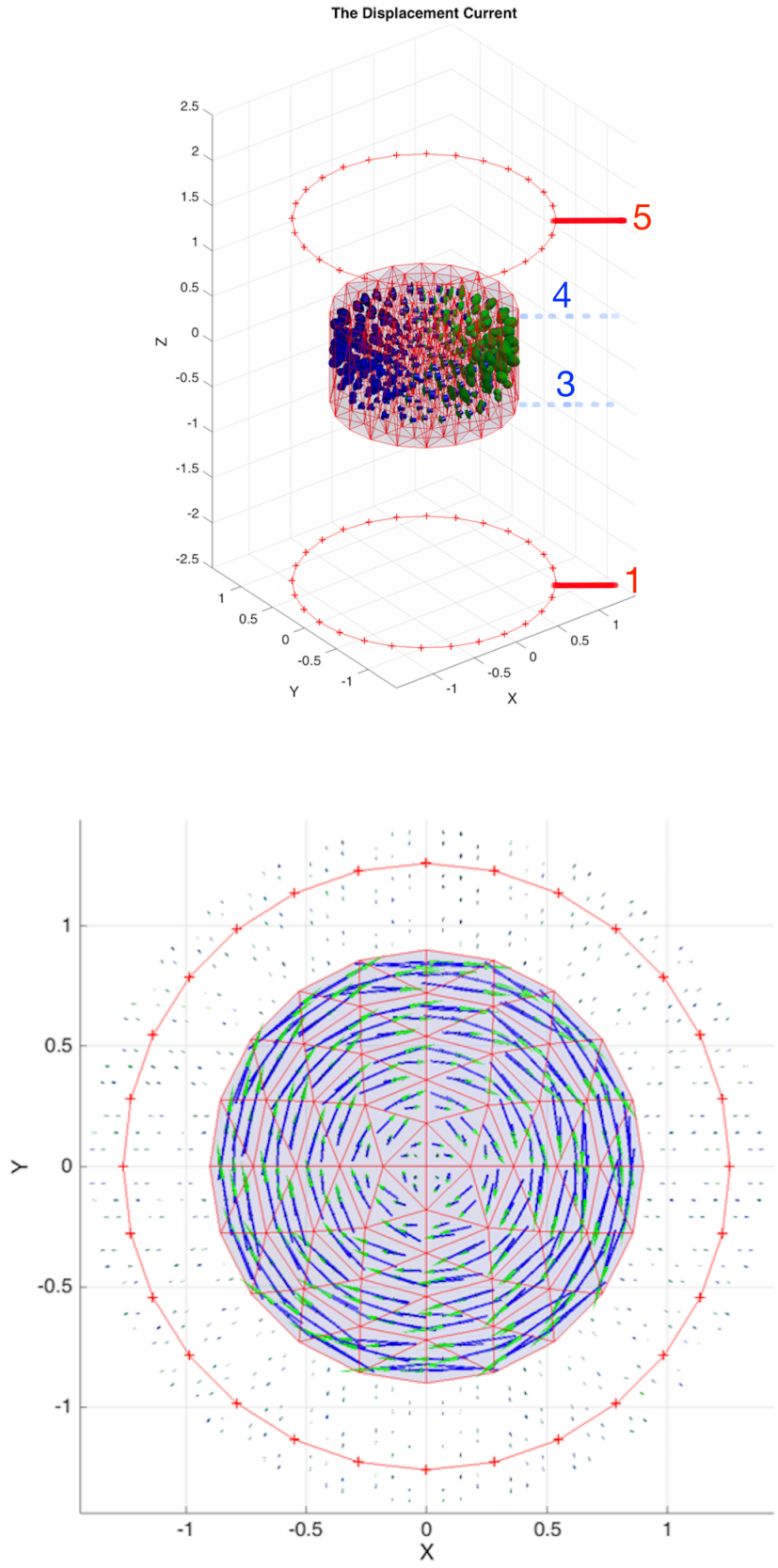

Figure 3.12 Displacement currents produced on a disk as the result of inductions from two coils numerically calculated at different vertical distances form the top and bottom surface (Side view on the top - Top view on the bottom).

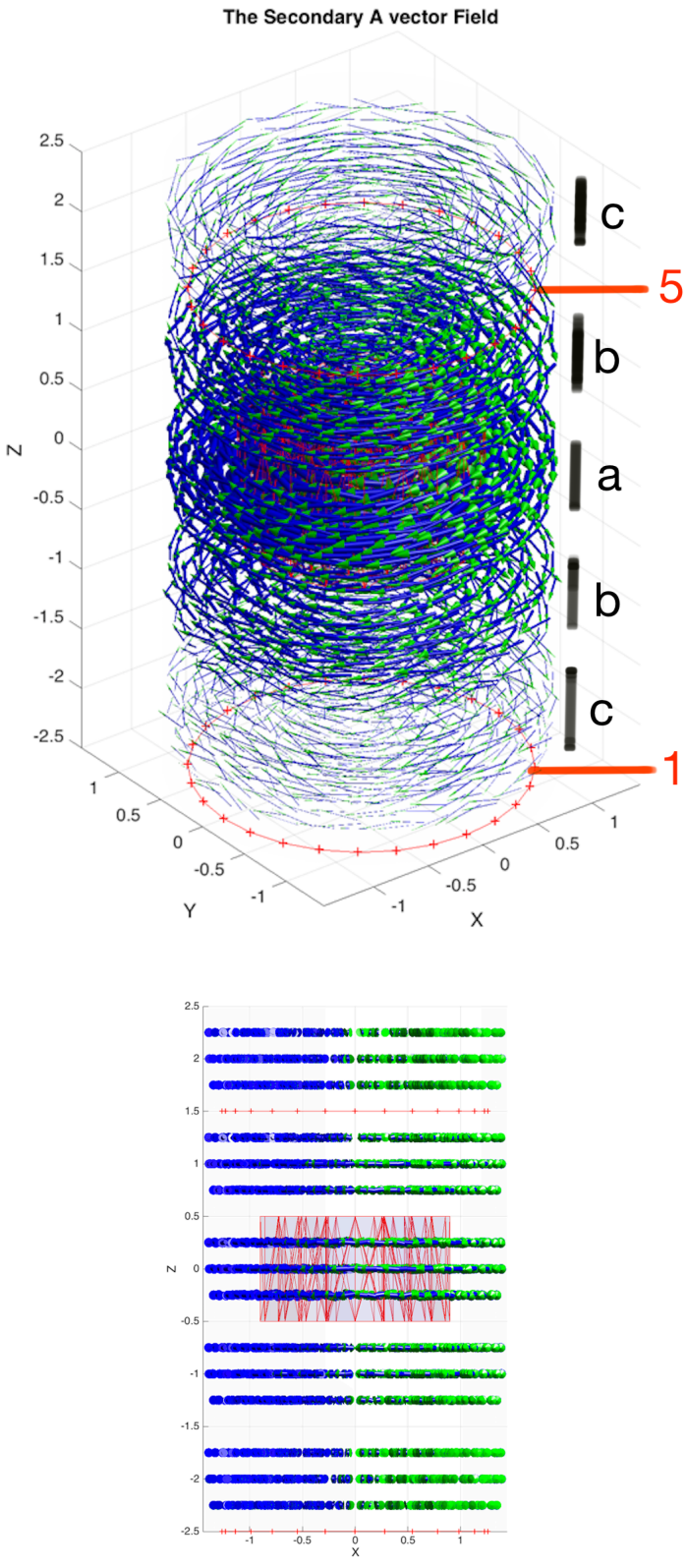

Figure 3.13 The numerically calculated secondary magnetic potential, **A** vector field in temporal gauge produced by eddy currents on the disk surface. The side view shows that the vectors curl around the disk (a, b and c are areas with different densities of **A**) (3D side view on the top - 2D side view on the bottom).

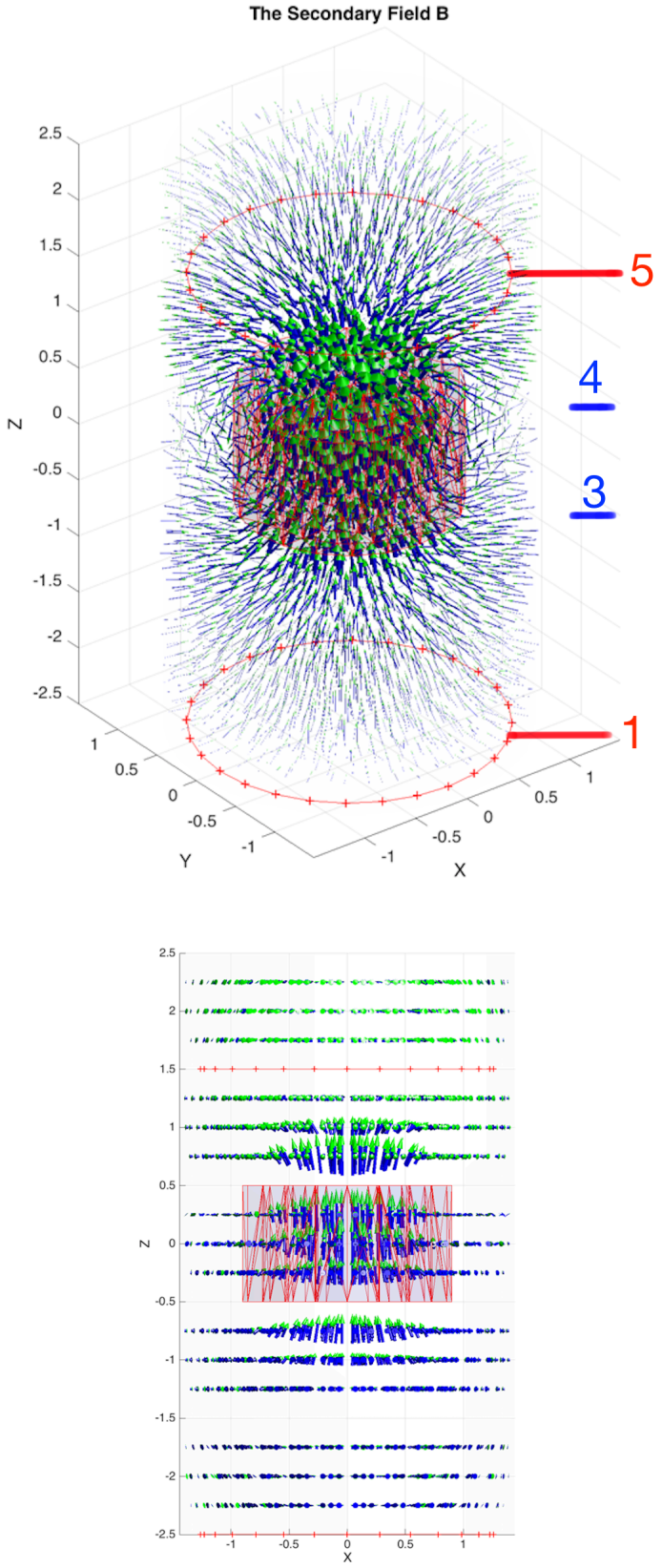

Figure 3.14 The numerically calculated secondary magnetic field, **B** vector field produced by eddy currents on the disk surface. The side view shows that the density of the vectors is maximum in the middle of the disk (3D side view on the top - 2D side view on the bottom).

CHAPTER 4 SENSITIVITY MATRIX CALCULATION

4.1 Sensitivity matrix

In general, sensitivity analysis for a system is concerned with the propagation of uncertainties in mathematical models and analysis of the influence of parameters on the state of the system (in our case the parameter is conductivity). By calculating the sensitivity with respect to various electromagnetic properties, we can predict the response of the system for a perturbation imposed upon it.
The sensitivity matrix is a very informative tool in the design process for a MIT system. At any point in space, the most sensitive direction for sensing the secondary field signal can be calculated. This is beneficial in the positioning of the sensors and also can be used to select different combinations of sensors in order to focus on a certain area in the ROI.
We start with introductory mathematical definitions and then we extract the sensitivity matrix from formulations developed in Chapter (3).
Let's consider a system depending upon n input parameters $\mathbf{p} = [p_1, ..., p_n]^T$ (p_n can be a conductivity distribution) with m output values $\mathbf{u} = [u_1, ..., u_m]^T$ (u_n can be a field set detected at all sensors). This system can be modeled mathematically using a function

$$\mathbf{F} : (D \subset R^n \rightarrow R^m) : \mathbf{p} \rightarrow \mathbf{u} = \mathbf{F}(\mathbf{p}) \tag{4.1}$$

well defined on an open domain D. The properties of such a model are fully determined by $\mathbf{F}$ which could be any map or matrix. However, $\mathbf{F}$ cannot always be known explicitly. For instance, in finite element calculations, $\mathbf{F}(\mathbf{p})$ might be the calculated value at n predefined points or edges. Evaluation of $\mathbf{F}$ in that case corresponds to evaluation of a matrix (Ostermann, 2005 ; Hairer *et al.*, 2010). Most numerical models developed to investigate physical models have matrix structures which satisfy the the definition of Eq.(4.1).

We investigate the behavior of $\mathbf{F}$ in a hyper spherical domain $\mathrm{SD}_R(\mathbf{q})$ with radius R around the point $\mathbf{q} \in$ D

$$SD_R(\mathbf{q}) = \{\mathbf{q} \in R^n :\| \mathbf{p} - \mathbf{q} \| \leq R\} \tag{4.2}$$

The $\| \cdots \|$ shows a norm on R^n. By reducing the radius, we can always assume that this sphere lies in the domain D of $\mathbf{F}$. For instance, we are interested in a distributed conductivity $\mathbf{p}$ over the ROI, which is close enough to a reference distribution $\mathbf{q}$. If $\mathbf{F}$ is Fréchet

differentiable at $\mathbf{q}$, meaning there exists a m×n matrix $\mathbf{J}$ such that for $\mathbf{p} \in SD_R(\mathbf{q})$

$$\lim_{\mathbf{p}\to\mathbf{q}} \frac{\| \mathbf{F}(\mathbf{p}) - \mathbf{F}(\mathbf{q}) - \mathbf{J}\cdot(\mathbf{p}-\mathbf{q}) \|}{\| \mathbf{p}-\mathbf{q} \|} = 0 \tag{4.3}$$

Then, the matrix $\mathbf{J}$ is the Jacobian matrix of $\mathbf{F}$ at point $\mathbf{q}$

$$\mathbf{J} = \mathbf{F}'(\mathbf{q}) = \begin{vmatrix} \frac{\partial F_1}{\partial p_1}(\mathbf{q}) & \cdots & \frac{\partial F_1}{\partial p_n}(\mathbf{q}) \\ \vdots & & \vdots \\ \frac{\partial F_m}{\partial p_1}(\mathbf{q}) & \cdots & \frac{\partial F_m}{\partial p_n}(\mathbf{q}) \end{vmatrix} \tag{4.4}$$

The existence of all partial derivatives of $\mathbf{F}$ at $\mathbf{q}$ is a necessary condition for Fréchet differentiabllity.
If the behavior of the system can be characterized by a Fréchet differentiable function $\mathbf{u} = \mathbf{F}(\mathbf{p})$, Its sensitivity with respect to the parameter p_j at the point $\mathbf{q}$ is defined as

$$\mathbf{s}_j = \frac{\partial \mathbf{u}}{\partial p_j} = \frac{\partial \mathbf{F}}{\partial p_j}|_{\mathbf{p}=\mathbf{q}} \tag{4.5}$$

which is given by the jth column of the Jacobian matrix $\mathbf{F}'(\mathbf{q})$. For instance, if we change the conductivity p_j of the j cell, the resulting change in the measured field is the product of sensitivity and the changed value. It is convenient to write all these partial derivatives (sensitivities) in an m×n matrix

$$\mathbf{S} = \mathbf{F}'(\mathbf{q}) \tag{4.6}$$

The sensitivity matrix $\mathbf{S}$ gives us the variation of the output values for small changes in the parameters

$$\mathbf{F}(\mathbf{p}) - \mathbf{F}(\mathbf{q}) \simeq \mathbf{S}\cdot(\mathbf{p}-\mathbf{q}) \tag{4.7}$$

for $\| \mathbf{p}-\mathbf{q} \|$ sufficiently small. Larger values of the difference can be divided in small enough difference values, which can be implemented iteratively. This essentially is the condition for any perturbative calculations (Stanley et Stewart, 2002).

4.2 Inverse solution of a differential equation

Finding the inverse solution for a differential equation governing physical models is a challenging procedure. If a problem is identified well-posed by Hadamard definition (a unique solution exists and the behavior is continuous with change in the initial condition), there is a good chance that the inverse equation can be solved using a stable numerical algorithm on a computer. Inverse problem is often (almost always) ill-posed (Kabanikhin, 2008). For example, the inverse heat equation is not a well-posed problem, as the boundary condition does not provide enough to find the temperature distribution as a function of time, and a unique solution is not guaranteed unless with some additional information. If the problem is not well-posed (ill-posed), it needs to be re-formulated in the process of numerical treatment. Generally the numerical treatment of an ill-posed problem, is done by additional prior assumptions, such as smoothness of solution. This process is known as regularization, and is discussed in Chapter (5).
The Jacobian matrix which is extracted in the next section shows that even large changes in the conductance of tissue can cause only small changes in the voltages values induced in the coils. By Hadamard definition, such inverse problem is called ill-posed.

4.2.1 Condition of a matrix

In numerical analysis and matrix calculations, the term condition normally arises. The concept is very close to that of sensitivity. The term is used to classify how sensitively the solution of a problem depends on its input data. Condition number is a way to quantify such a dependence.
The problem $\mathbf{p} \rightarrow \mathbf{F}(\mathbf{p})$ is called *well-posed* in $\mathrm{SD}_R(\mathbf{q})$ if and only if there exists a constant $L(R) \geq 0$ such that for all $\mathbf{p} \in \mathrm{S}_R(\mathbf{q})$

$$\| \mathbf{F}(\mathbf{p}) - \mathbf{F}(\mathbf{q}) \| \leq L(R) \cdot \| \mathbf{p} - \mathbf{q} \| \tag{4.8}$$

The Lipschitz constant $L(R)$ may be chosen here to be minimum without loss of any generality (Ostermann, 2005). $L(R)$ is called the condition number of Eq.(4.1) in $\mathrm{S}_R(\mathbf{q})$ and describes the maximum amplification of parameter variations in $\mathrm{S}_R(\mathbf{q})$. With appropriate regularity assumptions, it can be shown that

$$\lim_{R \rightarrow 0} L(R) = \| \mathbf{F}^{'}(\mathbf{q}) \| \tag{4.9}$$

The operator norm of the sensitivity matrix is the limit of the corresponding condition numbers. This shows that condition is just a rough estimation for sensitivity.
An ill-conditioned problem is indicated by a large condition number. Even if the problem is well-posed, it may still be ill-conditioned if the condition number is large (which it is in our case). It might be the case that the solution is continuous with respect to the initial conditions, but it suffers from numerical instability when solved with finite precision or when errors are added to the data. It means that a small error in the initial data can result in much larger errors in the answers. It is observed that our solution's behavior does not change continuously with the initial conditions (Kabanikhin, 2008).

4.2.2 The inverse MIT problem

The inverse MIT problem is known as an ill-conditioned and ill-posed problem. The sensitivity map for a conductive background differs extensively from a free space background and it is necessary to recalculate the Jacobian in each step. This is what makes the measurement of absolute value of conductivity far from its true value in linear approximations. However, the true value can be reached using the iterative solutions which is discussed in Chapter(5). The mathematical procedure for extracting the sensitivity matrix form Eq.(3.52) using the direct method will be discussed in the following section.

4.3 The idea of a direct method

Consider a function $\mathbf{B(x,\sigma)}$, which specifies the value of magnetic field of each point of x coordinate for given a conductivity distribution σ in a medium. The function $\mathbf{B(x,\sigma)}$ represents an output of the simulated device which is used in a reconstruction algorithm to produce the conductivity map. But in practical measurement devices, one can measure the magnetic field for a limited number of points along the x axis. In order to approximate a function using a few points, the values of the function as well as the values of the nth derivative of that function with respect to σ are required (higher orders of derivative provide a better approximation to the function). This statement is also true in finding a vector set containing the information about the values, as well as directions of the magnetic field, instead of a function. In the linear approximation, the function (vector set) is specified by its values and the values of the first derivative. Therefore to specify $\mathbf{B(x,\sigma)}$, we need its values at sensor positions and the first derivative of $\mathbf{B(x,\sigma)}$, which in each element can be calculated with respect to conductivity,

using the chain rule.
For the non-linear reconstruction, the derivative is calculated in iterations until the desired degree of accuracy is satisfied for the approximated function. For monitoring purpose, which is equivalent to calculating the change in the values of the function, the linear approximation is shown to be a promising criterion for the differential detection in EIT (Adler et Guardo, 1996).
The direct method is a new approach introduced in the next section to calculate the first derivative (or in an iteration) of the conductivity value function with respect to field from the same formulation which simulates the secondary magnetic field values. The calculation of the sensitivity matrix using this approach can considerably improve the calibration precision of model and therefore results of a practical MIT device.

4.3.1 Extraction of the sensitivity matrix - The direct method

We begin with Eq.(3.52)

$$(\mathbf{Z} - \kappa_j^2 \mathbf{T})\mathbf{e} = \mathbf{J} \tag{4.10}$$

Then, $\mathbf{e}$ can be written as :

$$\mathbf{e} = (\mathbf{Z} - \kappa_j^2 \mathbf{T})^{-1}\mathbf{J} \tag{4.11}$$

Taking the derivative of both sides with respect to σ_j(each element has its own conductivity and vector [$\mathbf{e}$] is sensitive to each one) will produce :

$$\frac{\partial \mathbf{e}}{\partial \sigma_j} = \frac{\partial [\mathbf{Z} - \kappa_j^2 \mathbf{T}]^{-1}\mathbf{J}}{\partial \sigma_j} \tag{4.12}$$

We expand Eq.(4.12) using the product rule of differentiation :

$$\frac{\partial \mathbf{e}}{\partial \sigma_j} = \frac{\partial [\mathbf{Z} - \kappa_j^2 \mathbf{T}]^{-1}}{\partial \sigma_j}\mathbf{J} + [\mathbf{Z} - \kappa_j^2 \mathbf{T}]^{-1}\frac{\partial \mathbf{J}}{\partial \sigma_j} \tag{4.13}$$

The term $\frac{\partial \mathbf{J}}{\partial \sigma_j}$ is zero as the external current is not dependent upon σ. The second term in Eq.(4.13) is zero. The term $(\mathbf{Z} - \kappa_j^2 \mathbf{T})$ is a matrix. However, in Eq.(4.13) the derivative of the inverse needs to be calculated. In order to find the derivative of the inverse we write :

$$\frac{\partial \mathbf{I}}{\partial \sigma_j} = \frac{\partial}{\partial \sigma_j}(\mathbf{Z} - \kappa_j^2 \mathbf{T})(\mathbf{Z} - \kappa_j^2 \mathbf{T})^{-1} \tag{4.14}$$

where $\mathbf{I}$ is the identity matrix. Assigning :

$$\mathbf{M} = (\mathbf{Z} - \kappa_j^2 \mathbf{T}) \tag{4.15}$$

and knowing that the derivative on the identity matrix is zero we can write :

$$0 = \frac{\partial \mathbf{M}}{\partial \sigma_j}\mathbf{M}^{-1} + \mathbf{M}\frac{\partial \mathbf{M}^{-1}}{\partial \sigma_j} \tag{4.16}$$

Multiplying both terms in Eq.(4.16) by $\mathbf{M}^{-1}$ and rearrangement on both sides of the equation results in the following equation, which specifies the relation between the derivative of the inverse of a matrix and itself.

$$\frac{\partial \mathbf{M}^{-1}}{\partial \sigma_j} = -\mathbf{M}^{-1}\frac{\partial \mathbf{M}}{\partial \sigma_j}\mathbf{M}^{-1} \tag{4.17}$$

Using Eqs. (4.13) and (4.17) we may write :

$$\frac{\partial \mathbf{e}}{\partial \sigma_j} = -\mathbf{M}^{-1}\frac{\partial \mathbf{M}}{\partial \sigma_j}\underbrace{\mathbf{M}^{-1}\mathbf{J}}_{\mathbf{e}} \tag{4.18}$$

The term $\mathbf{M}^{-1}\mathbf{J}$ is substituted with $\mathbf{e}$. As the matrix $\mathbf{M}$ is explicit function of $\mathbf{k}$ and not of σ, from the chain rule we obtain :

$$\frac{\partial \mathbf{e}}{\partial \sigma_j} = \frac{\partial \mathbf{e}}{\partial \kappa_j}\frac{\partial \kappa_j}{\partial \sigma_j} \tag{4.19}$$

Calculating the $\frac{\partial \mathbf{e}}{\partial \kappa_j}$ first using Eq.(4.18) :

$$\frac{\partial \mathbf{e}}{\partial \kappa_j} = -(\mathbf{Z} - \kappa_j^2 \mathbf{T})^{-1}(-2\kappa_j \mathbf{T})\mathbf{e} \tag{4.20}$$

The second term in the right side of the Eq.(4.20) is $\frac{\partial \mathbf{M}}{\partial \kappa_j}$.
Using Eq.(3.16), $\frac{\partial \kappa_j}{\partial \sigma_j}$ is :

$$\frac{\partial \kappa_j}{\partial \sigma_j} = \frac{-\imath\omega}{2\sqrt{\epsilon_j\omega^2 - \imath\omega\sigma_j}} \tag{4.21}$$

Using Eqs.(4.20) and (4.21) we can rewrite Eq.(4.19) :

$$\mathbf{S}_{\sigma j} = \frac{\partial \mathbf{e}}{\partial \sigma_j} = (\mathbf{Z} - \kappa_j^2\mathbf{T})^{-1} 2\kappa_j \mathbf{T}\mathbf{e} \frac{-\imath\omega}{2\sqrt{\epsilon_j\omega^2 - \imath\omega\sigma_j}} \tag{4.22}$$

$\mathbf{Z}$ and $\mathbf{T}$ are both square matrices of dimension $(m \times m)$ where m is the number of independent edges, $\mathbf{e}$ is a column vector of dimension $(1 \times m)$, and $\mathbf{S}_{\sigma j}$ is the jth column of the sensitivity matrix that is calculated for the jth element. The sensitivity matrix $\mathbf{S}_\sigma$ of dimension $(m \times j)$ calculated for the set $\mathbf{e}$ can be used along with Eqs.(3.26) and (3.7) to calculate $\mathbf{S}_{\sigma B}$ which is the sensitivity matrix calculated with respect to the magnetic field $\mathbf{B}$ at sensors positions. This is suitable for solving the inverse problem using the calculated values of the $\mathbf{B}$ field. $\mathbf{S}_\sigma$ can also be used along with Eqs.(3.26) and (3.51) to calculate $\mathbf{S}_{\sigma V}$ which is the sensitivity matrix calculated with respect to the voltage induced by the field at the sensor and is suitable for reconstruction of the conductivity from the induced voltages at the sensor, instead of their corresponding $\mathbf{B}$ field.

This procedure can be carried out for each element with respect to σ and ϵ and μ of all the other elements. For example, for each excitation in the case of having a number of 960 elements (which has 1349 independent edges), the procedure in Eq.(4.22) has to be carried out (1349×960) times for calculation of the sensitivity with respect to σ, and three times of that for all the passive electromagnetic properties. Therefore, building the sensitivity matrix or the Jacobian is the most time consuming part of the calculation.

The computation costs are high in terms of the amount of memory needed for the calculation. In our largest mesh with 155253 elements, 234 Gb of memory were needed to build the sensitivity matrix.

For each configuration of excitation currents for a given conductivity distribution in the region of interest (the initial condition), we have to carry out the sensitivity analysis once. As there are six different excitation patterns, the sensitivity matrix is calculated six times. In practical measurements, the detected field at the sensors for each excitation pattern is used to construct the conductivity map, along with the sensitivity matrix calculated for that excitation.

The same procedure for ϵ and μ yields the expressions :

$$\frac{\partial \mathbf{e}}{\partial \epsilon_j} = (\mathbf{Z} - \kappa_j^2\mathbf{T})^{-1} 2\kappa_j \mathbf{T}\mathbf{e} \frac{\omega^2}{2\sqrt{\epsilon_j\omega^2 - \imath\omega\sigma_j}} \tag{4.23}$$

$$\frac{\partial \mathbf{e}}{\partial \mu_j} = (\frac{1}{\mu_j}\mathbf{Z} - \kappa_j^2 \mathbf{T})^{-1} \frac{\mathbf{Z}}{\mu_j^2}\mathbf{e} \tag{4.24}$$

Eqs. (4.22), (4.23) and (4.24) are general equations that can be used for any excitation current and mesh configuration to calculate the sensitivity.

4.4 Fast calculation of the sensitivity matrix using the reciprocity theorem

The reciprocity theorem and its extension for non-quasi static fields (Mortarelli, 1980) have been used extensively in EIT and MIT for calculation of the sensitivity matrix.
In EIT the method is as well known as *adjoint field method* (Adler et Guardo, 1996) which uses the variational formulation of the Laplace equation along with a linear approximation to find an expression for the change in the conductivity. The method is also known as a fast method for calculation of the sensitivity matrix, as there exist a method known as direct method (requiring more computation time and power) for calculation of the EIT sensitivity matrix (Gómez-Laberge et Adler, 2007).
No direct method had been proposed for calculation of MIT sensitivity matrix, other than the one introduced in the previous section. However, the fast method for calculation of the sensitivity matrix in MIT developed by Geselowitz is derived from Eq. (4.25), which is a result of reciprocity theorem in electromagnetism (Geselowitz, 1971). The theorem states that for two distinct coils, the flux produced by coil a in coil b when a current is running in a, is identical to the flux produced in coil a while the same current is running in coil b. Using this principle along with the physical mutual energy concept we can write (Corson et Lorrain, 1962) :

$$\int_{\Omega} \nabla \cdot (\mathbf{E}_\phi \times \mathbf{H}_\psi - \mathbf{E}_\psi \times \mathbf{H}_\phi) d\Omega = 0. \tag{4.25}$$

Indices ψ and ϕ denote two different electromagnetic fields fields at the same spatial point but which are produced in two different situations. The index ϕ is the case when the field is produced by the excitation coil is on while the receiver coil is off with the object in the ROI. The index ψ applies when we run the current in the receiver coil with the same distribution of conductivity in the ROI, but now with the excitation coil turned off.
Using the vector identity :

$$\nabla \cdot (\mathbf{E}_\phi \times \mathbf{H}_\psi - \mathbf{E}_\psi \times \mathbf{H}_\phi) = \mathbf{H}_\psi(\nabla \times \mathbf{E}_\phi) - \mathbf{E}_\phi(\nabla \times \mathbf{H}_\psi) - \mathbf{H}_\phi(\nabla \times \mathbf{E}_\psi) + \mathbf{E}_\psi(\nabla \times \mathbf{H}_\phi) \tag{4.26}$$

and using Maxwell's equations (3.3) and constitutive laws (3.6), we can find the change in the mutual impedance (Somersalo *et al.*, 1992) :

$$\Delta Z = -\int_{\Omega} (\sigma_\phi + \imath\omega\Delta\epsilon_\phi - \sigma_\psi + \imath\omega\Delta\epsilon_\psi)\mathbf{L}_\phi\mathbf{L}_\psi d\Omega + \int_{\Omega} (\mu_\phi - \mu_\psi)\mathbf{K}_\phi\mathbf{K}_\psi d\Omega \tag{4.27}$$

which can be written in this more compact form :

$$\Delta Z = -\int_{\Omega} (\Delta\sigma + \imath\omega\Delta\epsilon)\mathbf{L}_\phi\mathbf{L}_\psi d\Omega + \int_{\Omega} \Delta\mu\mathbf{K}_\phi\mathbf{K}_\psi d\Omega \tag{4.28}$$

where factors $\mathbf{K}$ and $\mathbf{L}$ are defined as :

$$\begin{aligned}
\mathbf{L}_\phi &= \frac{-\imath\omega(\mathbf{A}_{p\phi} + \mathbf{A}_{s\phi} + \nabla V_\phi)}{\mathbf{I}_\phi} \\
\mathbf{L}_\psi &= \frac{-\imath\omega(\mathbf{A}_{p\psi} + \mathbf{A}_{s\psi} + \nabla V_\psi)}{\mathbf{I}_\psi} \\
\mathbf{K}_\phi &= \frac{\nabla \times \mathbf{A}_{p\phi} + \nabla \times \mathbf{A}_{s\phi}}{\mu_\phi \mathbf{I}_\phi} \\
\mathbf{K}_\psi &= \frac{\nabla \times \mathbf{A}_{p\psi} + \nabla \times \mathbf{A}_{s\psi}}{\mu_\psi \mathbf{I}_\psi}
\end{aligned} \tag{4.29}$$

The index p in $\mathbf{A}_{p\phi}$ corresponds to the primary field vector potential and s in $\mathbf{A}_{s\phi}$ is the secondary field vector potential. This formulation is not exact, as it considers a linear approximation. In order to get Eq. (4.27), after substituting for $\mathbf{E}$ and $\mathbf{B}$ using Maxwell's equations (3.3) and constitutive laws (3.6), only the linear terms of the Eq. (4.26) are kept. Also this formulation does not take into account any net current in the ROI (Hollaus *et al.*, 2004a). In order to implement Eq. (4.28) in the finite element method the integrals can be split up into sums of integrals over the finite element volumes. Then the change in the impedance can be calculated for the element j using :

$$\Delta Z_{\phi\psi} = -\sum_{j=1}^{n_{FE}} \left[(\Delta\sigma_j + \imath\omega\Delta\epsilon_j) \int_{\Omega_j} \mathbf{L}_\phi\mathbf{L}_\psi d\Omega \right] + \sum_{j=1}^{n_{FE}} \left[\Delta\mu_j \int_{\Omega_i} \mathbf{K}_\phi\mathbf{K}_\psi d\Omega \right] \tag{4.30}$$

where n_{FE} is the number of elements used in the finite element formulation. The specific contributions coming from the individual finite elements to the overall change in the mutual

impedance can be clearly seen in (4.30). The sensitivity matrix **GS** maps the material changes assigned to the finite elements to the voltage change in the receiver coil.

$$\Delta V_\psi = I_\phi.\mathbf{GS}.\left\{ \begin{array}{l} \Delta\sigma + \imath\omega\Delta\epsilon \\ \Delta\mu \end{array} \right\} \tag{4.31}$$

The entries in the sensitivity matrix **GS** for the finite element j are shown in :

$$\begin{aligned} \mathbf{GS}_j^L &= \int_{\Omega_j} \mathbf{L}_\phi \mathbf{L}_\psi d\Omega \\ \mathbf{GS}_j^K &= \int_{\Omega_j} \mathbf{K}_\phi \mathbf{K}_\psi d\Omega \end{aligned} \tag{4.32}$$

The calculation of the sensitivity map using this method requires only two forward problems to be solved to calculate $\mathbf{A}_{p\phi}$ and $\mathbf{A}_{s\phi}$ everywhere while the current is running in the transmitter coil and $\mathbf{A}_{p\psi}$ and $\mathbf{A}_{s\psi}$ while the current is running in the receiver coil. Computation of the sensitivity matrix using reciprocity principle is faster than the direct finite element method.

In the following chapter, using the sensitivity matrix, we introduce our method to solve the inverse problem. The inverse problem is usually ill-posed and needs regularization in the presence of data inaccuracies. The numerical singularity happens because of the fact that some of the eigenvalues of **Z** and **T** matrices of the forward operator are very small. This causes a strong amplification of the errors in the conductivity domain.

CHAPTER 5 INVERSE PROBLEM FOR MIT

5.1 The inverse problem

The inverse problem frequently arises in experimental situations when the description of the internal structure of a system is given by indirect noisy data (compared with the forward problem, estimation of the response of a system with a given complete specification of the internal structure).
In the last step, we want to interpret the conduction map from measurement of the secondary field. There are several methods developed in the literature, some of which are introduced briefly throughout this chapter. Then, the method used is elaborated in more detail.
The forward mapping problem can be described as :

$$\mathbf{B} = \mathbf{F}(\boldsymbol{\sigma}) \tag{5.1}$$

$\mathbf{F}$ is a map that includes geometrical properties as well as the estimated conductivity information. It is a map that takes $\boldsymbol{\sigma}$, a vector describing the conductivity of all cells, to $\mathbf{B}$ which is the vector of all the $\mathbf{B}$ fields at the potential detecting positions , and this for a given excitation current. In other words, each mode of excitation (each individual exciting coil) will give rise to a distinct forward problem such as Eq.(5.1). Then the corresponding inverse problem could be defined as :

$$\boldsymbol{\sigma} = \mathbf{F}^{-1}(\mathbf{B}) \tag{5.2}$$

So the problem is the finding of an inverse map which is not in most cases simply the inverse of a square matrix. As $\mathbf{F}$ might not even be a square matrix : If there are m field measurements and we are looking for conductivity n voxels, then $\mathbf{F}$ is $m \times n$ matrix which does not have an inverse unless $m=n$. That is why the solution of an inverse problem often is a compromise which results from an optimization problem. This requires methods such as the Maximum Likelihood Estimation (MLE) or the Maximum Aposteriori Estimation (MAP), which are discussed below.
The solution of Eq.(5.2) requires that the target region be discretized into voxels. A grid of tetrahedral finite elements of first order are employed here.
In order to develop the method and formulations for the inverse problem, we introduce the concepts of conditional probability and Bayes rule. We need to discuss the likelihood of a an event and methods to maximize that likelihood in order to deduce the Gauss-Newton approach, which is our method for the inverse problem. We use the single step Gauss-Newton

approach, for the differential imaging. This can be used to measure the difference in the secondary magnetic field when there is change in the conductivity of the ROI compared to the initial conductivity distribution. We have also used the iterations of this method to calculate the sensitivity matrix each time to be able to reconstruct the absolute value of the conductivity more accurate.

5.1.1 Maximum likelihood estimation

The maximum likelihood method is the procedure for finding the value of one or more parameters for a given statistic (distribution of a certain quantity of interest, such as the conductivity distribution) which makes the known likelihood distribution a maximum.
Given the knowledge that event B has occurred (Data of **B** field values), what is the probability that event A (certain conductivity distribution) happens ? This is the question of the conditional probability. The statement is written in the following form :

$$P(A|B) = \frac{P(A \cap B)}{P(B)} \tag{5.3}$$

This gives us a fraction of B that also contains$A$.
For example, taking the population of Canada as a sample, we define the occurrence X_i which can take the values of zero and one, where zero is the individual being male and one is the individual being female (X_i is an event with two possible outcomes). If p is the probability (given knowledge) of finding a female individual in town, then maximum likelihood function is just the fraction of individuals. Given the following likelihood function :

$$f(X_i|p) = p^{X_i}(1-p)^{X_i} \tag{5.4}$$

Then the likelihood of the events are :

$$f(1|p) = p^1(1-p)^0 = p \tag{5.5}$$

$$f(0|p) = p^0(1-p)^1 = 1-p \tag{5.6}$$

For different values of i (X_i is an event with N possible outcomes), the likelihood function has the following form :

$$f(X_1 = x_1, X_2 = x_2, X_3 = x_3, \cdots, X_N = x_N|p) = \prod_{i=1}^{N} p^{x_i}(1-p)^{1-x_i} \tag{5.7}$$

where x_i is the value that X_i takes in our model. Given this likelihood function, we can find the maximum of that function by taking its derivative with respect to the probability p (taking log and then derivative). The maximum likelihood probability p_{ML} in this case is the average.

$$p_{ML} = \overline{X} = \frac{1}{N}\sum_{i=1}^{N} X_i \tag{5.8}$$

MLE is a well-known method for estimating a parameter of distribution. For example, if we are interested in the conductivities of voxels, but we are unable to measure the conductivity of every single voxel in a ROI due to some constraints, MLE is a good candidate method. Assuming that the conductivities are normally distributed with some unknown mean and variance, the mean and variance can be estimated with MLE while only knowing the conductivities of some voxels as a sample of the overall population of voxels. MLE will do this by taking the mean and variance as parameters and finds particular parametric values that make the observed results the most probable given the model.

Given the data $D = (x_1, x_2, \cdots, x_n)$ ($x_n \in \mathbb{R}^d$ can be vectors or scalars) in d dimensional real space, we can assume a family of distributions $\{p_\theta, \theta \in \Theta\}$ on $\mathbb{R}^n$. If D is a sample with the mean p_θ (possible conductivity distribution) for some $\theta \in \Theta$, MLE will estimate the true value of parameter that is originating D. Θ_{MLE} is a MLE for θ if

$$\Theta_{MLE} = argmax(P(D|\theta)) \quad \theta \in \Theta \tag{5.9}$$

This means that we have to find the value of θ which makes the argument maximum. (In our specific problem, D is a set of all magnetic field vectors (d=3) in n voxels, while θ is the conductivity distribution of those n voxels, Θ is a set of all possible conductivity distributions, and p_θ is the probability of that conductivity).

The method is relatively easy to use and interpret as the distribution is invariant under re-parametrization. However, it lacks any representation for the uncertainty. Moreover, the existence and uniqueness of the MLE is not always guaranteed. The method also suffers from over-fitting of the data.

These drawbacks are the reason that MLE is not directly used in the inverse problem. However, modifications to MLE will provide us with a tool which is known to be suitable for this type of problem. This method is introduced in the next section.

5.1.2 Maximum *a posteriori* estimation

It may happen that we have a priori information about the physical process whose parameters we want to estimate. Such information can come either from scientific knowledge of the physical process or from previous empirical evidence. In our case, the prior information is knowing that we are imaging a model of the brain, with a certain size and certain expected values of conductivity in a region. This prior information will result in a more specific answer to the question how a parameter (conductivity) affects the data (collected **B** fields).
MAP is a method based on MLE that employs an augmented optimization objective which incorporates a prior distribution over the quantity one wants to estimate.
Given the data $D = (x_1, x_2, \cdots, x_n)$ in $\mathbb{R}^d$, we can assume a joint distribution $P(D, \theta)$ on $\mathbb{R}^d$. The goal is to find a good value of θ for D, where θ is the parameter from which the data comes from. Θ_{MAP} is a MAP estimation for θ if

$$\Theta_{MAP} = argmax(P(\theta|D)) \quad \theta \in \Theta \tag{5.10}$$

where Eq.(5.10) is the *a posteriori* distribution on θ. If we compare Eqs.(5.9) and (5.10), the difference is the order of D and θ. There is an inversion in conditional probability. Bayes rule tells us how to do this inversion :

$$P(B|A) = \frac{P(A|B)P(B)}{P(A)}. \tag{5.11}$$

This may be verified using Eq.(5.3). In our forward problem, the question is : what is the **B** field in all voxels given the conductivity distribution. So the inverse problem question follows : given the **B** field, what is the most probable conductivity distribution. The Bayes statistic is used to reverse the conditional probability in the forward problem for the inverse problem.
In the following section, we find the Θ_{MAP}, given the data set D, and θ as a random variable.

5.2 Implementation of maximum a posteriori estimation for a multivariate Gaussian

The first order estimate of the change in the calculated distribution magnetic field **B** with respect to a variable γ (conductivity, permittivity or permeability distribution in the cells) using the first order perturbation (Taylor expansion) is given by :

$$\Delta\mathbf{B} = \frac{\partial\mathbf{B}}{\partial\gamma}\Delta\gamma \tag{5.12}$$

The derivative is just the definition of the sensitivity matrix, which we replace with $\mathbf{S}_{\sigma B}$, as introduced in the previous chapter. The form of the Eq.(5.12) is the same if we write it for voltage while the sensitivity matrix changes to $\mathbf{S}_{\sigma V}$ ($\Delta\mathbf{V} = \frac{\partial \mathbf{V}}{\partial \gamma}\Delta\gamma$). We use the general term $\mathbf{S}$, for convenience and write :

$$\Delta\mathbf{B} = \mathbf{S}\Delta\gamma + n \tag{5.13}$$

and the variable n introduces noise into the system (Gaussian noise in our case). We need to calculate the Θ_{MAP} for the Eq.(5.13). In the development of the final equations we use notations $\mathbf{B}$ and γ instead of their changes for notation simplifications. The corresponding MAP formulation can be written (Using Bayes law) as :

$$\gamma = argmax_{\gamma} P(\gamma|\mathbf{B}) = \frac{P(\mathbf{B}|\gamma)P(\gamma)}{P(\mathbf{B})} \tag{5.14}$$

P($\mathbf{B}$) does not vary with respect to γ and does not effect the maximum. Then Eq.(5.14) reduces to

$$\gamma = argmax_{\gamma} P(\mathbf{B}|\gamma)P(\gamma). \tag{5.15}$$

In order to solve Eq.(5.15), we need to have an estimation of $P(\mathbf{B}|\gamma)$ and $P(\gamma)$. We assume they are normally distributed (Gaussian), $N(\mu, \sigma^2)$, where μ is the mean and σ^2 the standard deviation. However, as $\mathbf{B}$ in our formulation is a vector, we have used a multivariate Gaussian for this estimation. Multivariate Gaussian is a generalization of the univariate distribution (regular Gaussian) to higher dimensions. A random vector is said to be n-variate normally distributed if every linear combination of its' n components has a univariate normal distribution.

Consider $X = \{x_1, x_2, x_3, \cdots, x_i\}$ where the x_i are independent and each can be estimated by $N(\mu_i, \sigma_i^2)$ with μ_i being the mean and σ_i the standard deviation of the ith parameter. Then the multivariate Gaussian $N(\mu, \mathrm{C})$ is n normal distribution in $\mathbb{R}^n$ where C is the semi definite symmetric matrix called the covariance matrix. Covariance of two parameters X and Y is defined as :

$$Cov(X, Y) = E(XY) - E(X)E(Y) \tag{5.16}$$

where E is the expected value of that parameter. If x_i and x_j are independent, then the $Cov(x_i, x_j) = 0$ and the covariance matrix is just the diagonal matrix of variances.

$$C = \begin{vmatrix} \sigma_1^2 & \cdots & 0 \\ \vdots & & \vdots \\ 0 & \cdots & \sigma_i^2 \end{vmatrix} \tag{5.17}$$

The diagonal is just $Cov(x_i, x_i)$ which equals σ_i^2. We may write $P(\mathbf{B}|\gamma)$ as follows :

$$P(\mathbf{B}|\gamma) = N(\mathbf{S}\gamma, \Gamma_N) \tag{5.18}$$

where the term $\mathbf{S}\gamma$ in the distribution is the mean value and the variance Γ_N is the noise. $P(\gamma)$ can also be written in terms of a multivariate Gaussian :

$$P(\gamma) = N(\gamma_0, \Gamma_\gamma) \tag{5.19}$$

γ_0 is zero in our case as we want the values of γ, which represent the difference in electrical properties, to be zero. Using Eqs.(5.18) and (5.19) we may rewrite Eq.(5.15) :

$$\gamma = argmax_\gamma(N(\mathbf{S}\gamma, \Gamma_n)N(\gamma_0, \Gamma_\gamma)) \tag{5.20}$$

where the first term $N(\mathbf{S}\gamma, \Gamma_n)$ is given by :

$$N(\mathbf{S}\gamma, \Gamma_n) = \frac{1}{(2\pi)^{\frac{N}{2}}\sqrt{\Gamma_n}} \exp(-\frac{1}{2}(\mathbf{B} - \mathbf{S}\gamma)^T\Gamma_n^{-1}(\mathbf{B} - \mathbf{S}\gamma)) \tag{5.21}$$

and the second term $N(\gamma_0, \Gamma_\gamma)$ is given by :

$$N(\gamma_0, \Gamma_\gamma) = \frac{1}{(2\pi)^{\frac{N}{2}}\sqrt{\Gamma_\gamma}} \exp(-\frac{1}{2}(\gamma - \gamma_0)^T\Gamma_\gamma^{-1}(\gamma - \gamma_0)) \tag{5.22}$$

each being a multivariate Gaussian. In order to maximize the argument, we do the Log transformation (Log is a monotonic function) which makes calculations of the matrix more straightforward. Eq.(5.15) is then rewritten as :

$$\begin{aligned}
\gamma &= argmax_\gamma(\log(P(\mathbf{B}|\gamma)P(\gamma))) \\
&= argmin_\gamma(-\frac{1}{2}(\mathbf{B} - \mathbf{S}\gamma)^T\Gamma_n^{-1}(\mathbf{B} - \mathbf{S}\gamma) - \frac{1}{2}(\gamma - \gamma_0)^T\Gamma_\gamma^{-1}(\gamma - \gamma_0)) \\
&= argmin_\gamma((\mathbf{B} - \mathbf{S}\gamma)^T\Gamma_n^{-1}(\mathbf{B} - \mathbf{S}\gamma) + (\gamma - \gamma_0)^T\Gamma_\gamma^{-1}(\gamma - \gamma_0))
\end{aligned} \tag{5.23}$$

In this final form of Eq.(5.23) the term $(\mathbf{B} - \mathbf{S}\gamma)^T\Gamma_n^{-1}(\mathbf{B} - \mathbf{S}\gamma)$ is called fidelity to the measurement and the term $(\gamma - \gamma_0)^T\Gamma_\gamma^{-1}(\gamma - \gamma_0)$ is called fidelity to the prior information. Taking the derivative of the expression with respect to γ and setting it equal to zero give us an expression for γ :

$$\gamma_{MAP} = ((\mathbf{S}^T\Gamma_n^{-1}\mathbf{S} + \Gamma_\gamma^{-1}))^{-1}\mathbf{S}^T\Gamma_n^{-1}\mathbf{B} + ((\mathbf{S}^T\Gamma_n^{-1}\mathbf{S} + \Gamma_\gamma^{-1}))^{-1}\Gamma_\gamma^{-1}\gamma_0 \tag{5.24}$$

Considering $\gamma_0 = 0$ will eliminate the second term of the Eq.(5.24). Then, in the first term the expression $((\mathbf{S}^T\Gamma_n^{-1}\mathbf{S} + \Gamma_\gamma^{-1}))^{-1}\mathbf{S}^T\Gamma_n^{-1}$ is just a pseudo inverse of the sensitivity matrix $\mathbf{S}$ as the inverse might not be calculated simply by inverting the matrix depending on the conditioning of the Matrix. The sensitivity matrix is not always a square matrix and cannot be simply inverted since the number of measurements is generally less than the number of unknown conductivity variations. We can replace the sensitivity matrix $\mathbf{S}_{\sigma B}$ with $\mathbf{GS}_{\sigma B}$ according to Eqs. (4.22) and (4.30) to compare the reconstructed images of the reciprocity method and the direct method.

Equation (5.24) is the main formula that we use in our inverse problem (considering the fact that γ and $\mathbf{B}$ both correspond to the change in the quantities). The inverse problem may take components of $\mathbf{B}$ or its corresponding induced voltage V as the input. The one used in this reconstruction problem is V. Using the general Eq. (5.24) and replacing $\mathbf{B}$ with $\Delta\phi$ (2.1) and $\mathbf{S}$ with $\mathbf{S}_{\sigma V}$, we can estimate changes in the conductivity of the ROI.

As the problem is ill-posed, any discrete linearized approach will be ill conditioned. To overcome this problem, we have included the prior information into the system. This regularizes the ill posed problem. In our case, this prior information will be the location of the head and a prior guess as to the conductivity which we want to determine.

The noise terms can be written as $\Gamma_n = \sigma_n\mathbf{I}$ and $\Gamma_\gamma = \sigma_\gamma\mathbf{I}$ ($\mathbf{I}$ being the identity matrix) and values of the sigma (standard deviation) determines the amount of regularization used in the inversion. The ratio of $\frac{\sigma_\gamma}{\sigma_n}$ is known as λ in the literature and is called the regularization parameter. It acts like a weighting factor to find a balance between the fidelity to the measurement and fidelity to the prior information.

By choosing different forms of the covariant matrix, we can build different regularization methods. Using the unit matrix is called the Tikhonov-regularization method which is known for penalizing high values of the reconstructed conductivity changes. Using the number of nearest neighbor of the element i in the covariance matrix will lead to a regularization method called Neighboring matrix. In this dissertation, we have used the identity matrix regularization method. Other regularization methods can be used in this inverse problem which is a subject of future work.

5.3 Iterative Gauss-Newton approach

In practice, even though a linear reconstruction algorithm will often successfully locate an isolated inclusion in a homogeneous background (like detection of a lesion in the gray matter background), a nonlinear method is needed to reconstruct more complicated conductivity

distributions, such as several nearby objects .

The non-linear image reconstruction problem consists in reconstructing the absolute value of the conductivity of the ROI knowing the detected values of **B** magnetic field. This can be done using iterative solutions based on the optimization methods. However, the inverse problem is ill-posed and any discrete linearized approximation will be ill conditioned. Moreover, the measurement of the **B** field contains uncertainties and limited precision, which is included in the simulation in the parameter (Γ_n). In order to partially overcome this problem, we add prior information (initial guess) for conductivity value to regularize the ill-posed problem.

The regularized Gauss-Newton method uses repeated linearization to overcome the non-linearity, and incorporates a priori information about the unknown conductivity to obtain a stable solution of the inverse problem. That's why the linearization used in the forward problem, to get the Jacobian matrix or Fréchet derivative of the forward map, is an important part of such methods.

A row of the Jacobian matrix can be interpreted as a map which shows the sensitivity of a given measurement to a small change in conductivity of each element of the mesh. These sensitivity maps depend strongly upon the background conductivity, from which the linearization has been carried out. If the sensitivity matrix is calculated for the device before considering the prior information, the linear reconstruction provides less accurate conductivity values compared to the case that is calculated when the prior information is added.

When applying Newton's method, we use the prior information on the conductivity σ to calculate the sensitivity matrix for this parameter and using the calculated **B** field to get $\Delta\sigma$. Then for this updated value of conductivity (incremented by $\Delta\sigma$ in each iteration), the sensitivity matrix should be recalculated and the procedure iterates until convergence. If the solution of the inverse problem is close to the initial guess, the method typically converges. Fig.(5.1) shows the steps schematically. This procedure is time consuming, hence a complete iterative identification run requires significant computing power, bottleneck being the calculation of the sensitivity matrix. In this dissertation we use the Newton-one-step error reconstructor (NOSER) for the differential imaging and iterate it n steps for the absolute imaging (It means that $n = 1$ will just be the NOSER). The iteration is terminated when the residual error falls below the measurement accuracy of conductivity, which we set at 10^{-6} Sm^{-1}.

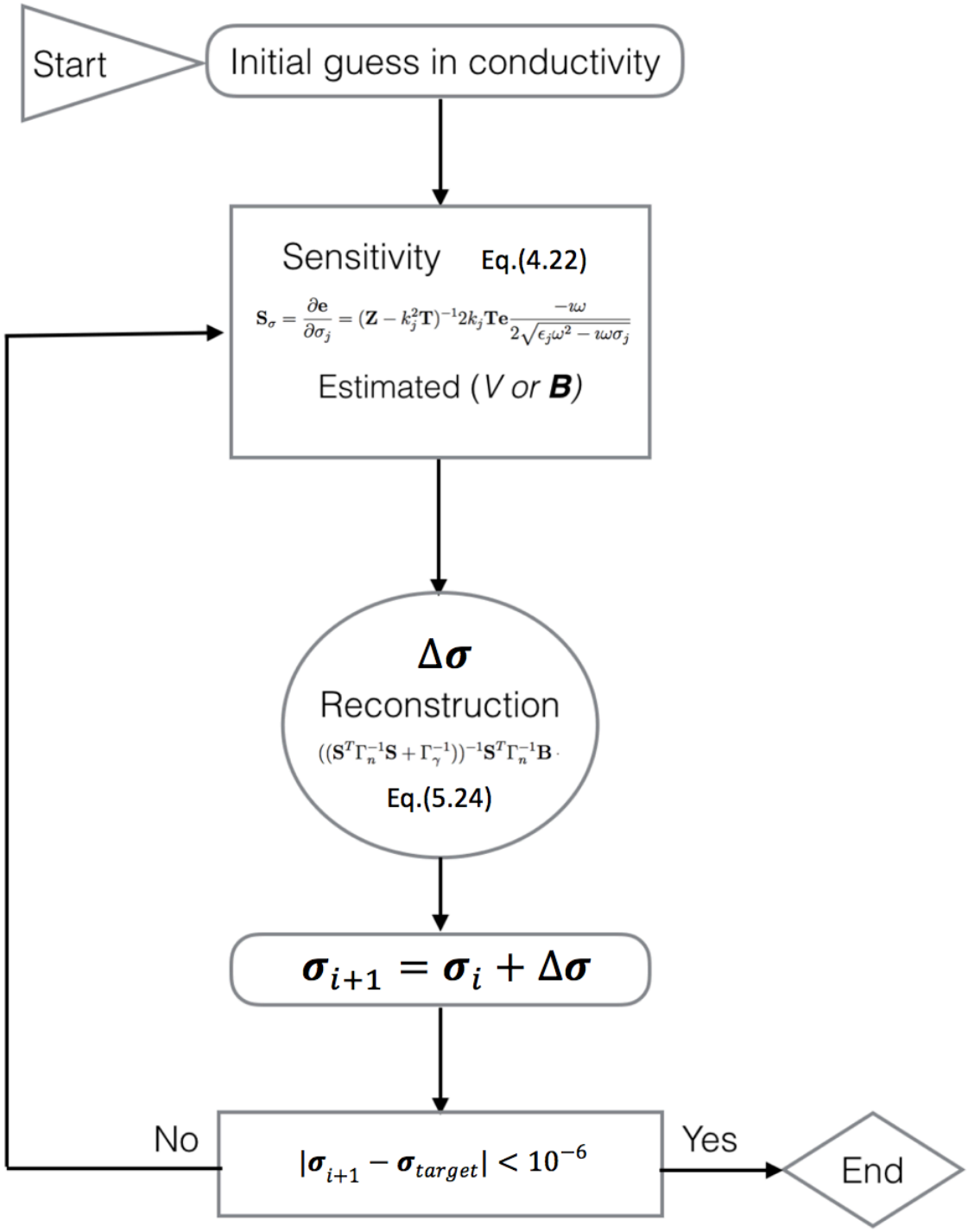

Figure 5.1 Flow chart showing the steps and conditions of the iterative solution.

CHAPTER 6 SIMULATION RESULTS

6.1 Simulation details

We use the proposed device in the section (2.4) to run the forward simulation and the inverse reconstruction. The cylindrical geometry and dimensions of the ROI were chosen based on the requirements of performing differential imaging of the lesion in the head. There are six concentric excitation coils surrounding the area dedicated to the head (Fig.(2.2)) with a radius 30 cm parallel to each other and there are five layers of 16 detection coils of radius 5 cm surrounding the ROI (sensors) and perpendicular to the excitation coils at each level. In total 80 sensors cover the whole region of interest wall which we use their detected field value for reconstruction of the conductivity.

The excitation frequency is 50 kHz which was chosen based on the fact that lower frequencies are better candidates for detection of the conductivity contrast due to the ischaemic stroke (Horesh *et al.*, 2005 ; Holder, 1992 ; Gabriel *et al.*, 1996c), as these frequencies provide higher contrast between the blood and the white matter. Furthermore, as discussed in chapter (2) lower frequencies are better candidates in terms of lowering the noise due to electronic elements of the device.

The excitation current of 1 A was chosen to induce the primary field. Even though tissue heating is known to be negligible in MIT (Holder, 2004), we made sure the system is operating within the safety limit in terms of the amount of electromagnetic exposure. This will be discussed more in section.(6.5.6).

To avoid the subtleties of working with more complex head mesh in a feasibility study for the contrast detection, we decided to use a simpler model. The head is estimated with a disk model with a radius of 20 cm and the thickness of 10 cm, having three layers with distinct electrical properties as shown in Fig.(2.2). This model can be provide us with answer to preliminary questions such as what is the value of the secondary signal for a certain conductivity contrast size at a certain frequency or what is the achievable resolution, which are very useful in early stages of designing a MIT device.

We use this device to calculate the expected field at the sensors for a conductivity contrast with a fixed volume for three different locations of the disk. We will calculate the sensitivity matrix and then use the calculated field and sensitivity for reconstruction of the conductivity map of ROI. We investigate the reconstruction problem for two method of sensitivity calculation introduced in chapter (4) and use following performance criteria to compare them : We calculate the reconstruction error (normalized error of reconstructed conductivity) for the

image. The error function is defined in Section.(6.5) in Eq.(6.2) and it quantifies the difference between the reconstructed conductivity and the true values of the target conductivity. Then we calculate the point spread function, also related to spatial resolution (1/mm), which inform us about how a point source is blurred and distorted through to imaging system and can highlight the appearance of artifacts in the image. It is defined in Appendix (B) and mostly exploited in Section.(6.6.1). The PSF is then used to extract the resolution of the image.

6.1.1 Computational details

The forward and inverse problems have been developed in MATLAB. Objects are defined with symmetrical layers each having different electrical properties. The interactions of the ROI with the magnetic field produces different currents in each region and such interaction is quantified in the magnitude of the detected signal. The program was bench-marked with known classical models and qualitative results for the forward problems that were presented in Chapter (3).

This work has been done using a 2.2 GHz Core-i7 Intel CPU with shared RAM that was extended to 234 Gb for the full calculation of the sensitivity matrix for the largest mesh. The coding materials are available as a separate file.

Table (6.1) shows the details of numerical calculations and specifies the computational requirements for simulation of the disk model. For calculations which needed more number of RAMs, supercomputer clusters were used. The results in this chapter are calculated using three mesh set that were used in the forward and one for the inverse problem as listed in Table (6.1). The smallest mesh has 3840 number of elements, which is more than the total independent measurements in 3D and therefore suitable for the inverse problem in 3D. The first column shows the number of the elements, the second column shows the number of the edges (degrees of freedom in the numerical model or the number of calculated Whitney function basis), the third column shows the run time for the full forward problem (F.P), which includes the calculation of the sensitivity matrix and the last column is the gigabytes RAMs that were used for forward simulation.

Table 6.1 Details of meshes used for the forward problem calculations.

No. of Elements	No. of Edges	Run time of the Full F.P	dedicated RAM
3,840	4,924	43 minutes	12 Gb
61,440	75,114	3 Weeks and 2 days	64 Gb
155,253	182,305	8 weeks and 4 days	234 Gb

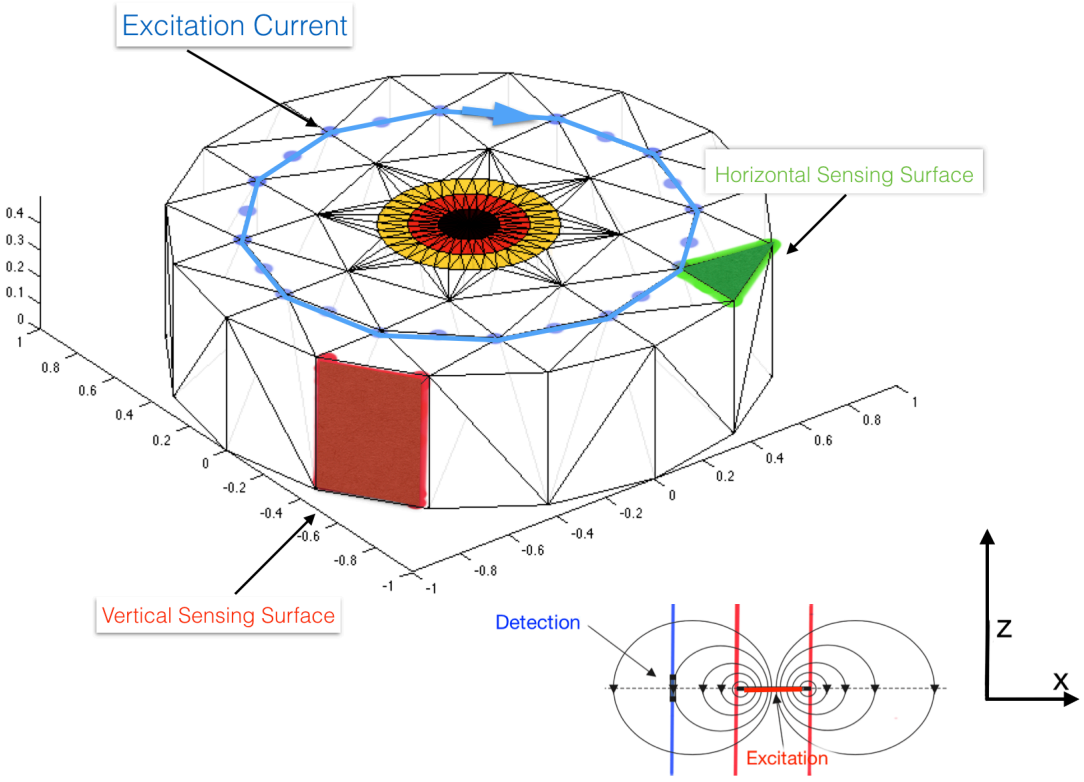

Figure 6.1 A slice of the ROI showing the possible orientation of surfaces that can be used for placing induction and detection coils. For this configuration of excitation and detection, the sensor positioned on the vertical surface is less sensitive to measurement of the primary magnetic field, compared to the horizontal one. Therefore vertical position is prefered in terms of primary coil field cancelation.

We used a mesh with a larger number of elements for the forward problem compared to inverse problems. The rationale is that we wanted to have a precise forward model with having more voxels in development of the model. This will allow us calculate the sensitivity at more points in the space. However, as the resolution is bounded by the total number of independent

measurement, fewer number of voxels (number of elements) were used in the mesh for the inverse problem.

The mesh used for the inverse problem has 3840 elements for 3D reconstruction, which is much less than the number of elements used for the disk forward problem (155253 elements). A slice of the ROI (between the coils no. 4 and 5) is shown in Fig.(6.1). The excitation current is simulated along the edges shown with blue line. The vertical sensing surface is used to model the sensor and the induced voltage in the sensor is calculated by integration of the **A** vector along the edges of the red square. The sensor arrangement for this slice, along with numbers attributed to this sensors in this chapter is shown in Fig.(6.2). The *a* located at [7.5,0,0], *b* [5,0,0] and *c* [0,0,0] are three different positions‘of the disk in the ROI which the detection of the contrast is investigated.

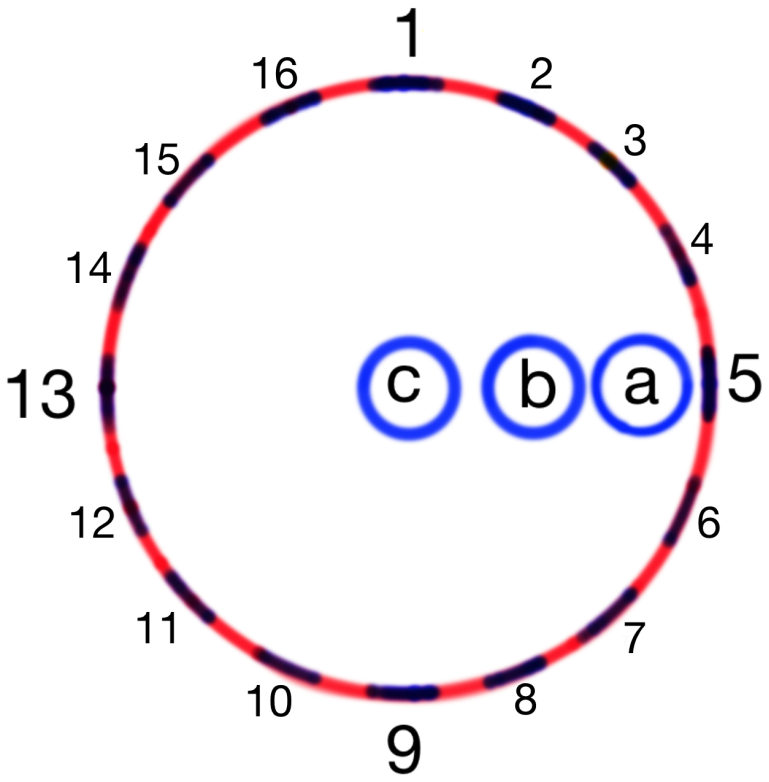

Figure 6.2 Schematic figure showing the relative sensors position and their attributed position numbers. The positions of the conductive area is shown by circles *a*, *b* and *c*

6.2 Secondary field range

In order to investigate that our sensors are suitable in terms of the detectable field range in a MIT device, it is useful to know what field values are expected due to a certain conductivity contrast. The change in the detected magnetic field at the sensor depends on the conductivity contrast value, the volume of the contrast, the distance of the contrast from the sensor, as well as the frequency and magnitude of the excitation current.

At a fixed frequency, the excitation current should provide a primary field within the safety zone in terms of the amount of exposure of the tissue to electromagnetic radiations. As this radiation is proportional to the square of frequency and the excitation current (Eq.(6.6)), at a fixed frequency there exist a maximum allowable excitation current that will result in the strongest secondary field. However, this maximum excitation current at 50 kHz is more constrained by electronics (driving high AC currents in the excitation coil) rather than the amount of electromagnetic radiations. We have used 1 A for the excitation current and will show in this section that the resulting secondary field is of pT order. This field can be detected with our sensors and used for a successful reconstruction. However the excitation current can be increased to increase the secondary magnetic field, provided we stay in the safety zone in terms of the amount of exposure of the tissue to electromagnetic radiations. This topic will be more discussed in section.(6.5.6).

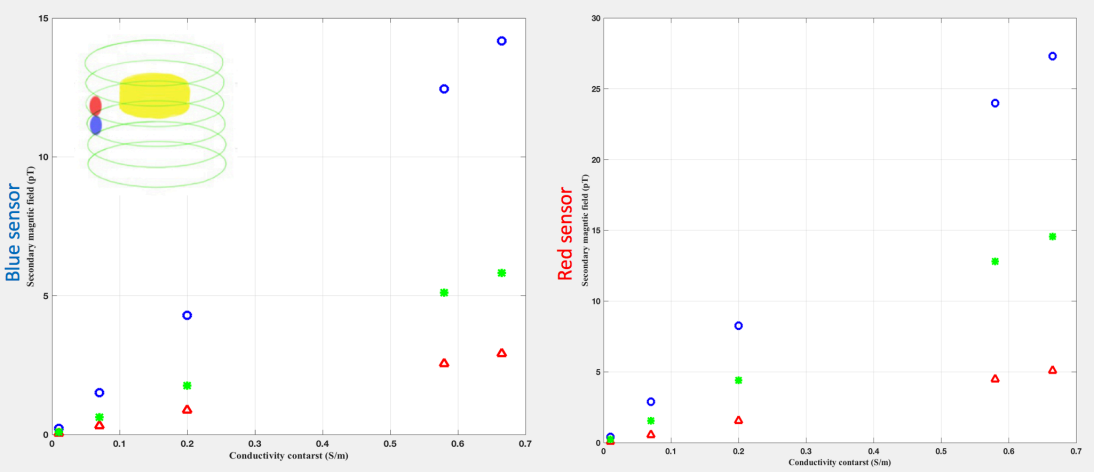

Figure 6.3 The change in the secondary magnetic field in the red and blue sensors. The circular blue dots are the detected change in the magnetic field value at position a, the green astricks show the change in magnetic field at position b, and the red triangles show the change in the magnetic field at position c

Fig.(6.3) shows the value of the change in magnetic field due to the contrast while the current of 1A is running in the excitation coil number 4. For a fixed contrast volume, we use the forward simulator developed in chapter (3) to calculate the change in secondary magnetic field at two sensors (blue and red indicted in the Fig.(6.3)) at the position 5 shown in Fig.(6.2). We calculate the change in secondary magnetic field value for two sensors at 3 different positions a, b and c in the ROI as indicated in Fig.(6.2).
The secondary field due to the the disk which has the conductivity average of the gray and white matter has the order of some nT, while the contrast due to the blood with fixed volume of 75 cm^3 produces the change in the magnetic field in the order of some pT.
The linear change of the field with respect to conductivity is the result of using the linear model of the Helmholtz equation. The slope of the line connecting the blue or red markers shows how sensitive a position in ROI is to the conductivity contrast. We will elaborate more on the sensitivity concept in section (6.3.1).
Using coils or GMI sensors can accommodate a good detection at tens of pT. Therefore, for the case of the blood lesion which corresponds to the contrast value of 0.59, the signals are promising, specially for the red sensor at positions a and b. However the conductivity contrast which result in a change in magnetic field which is lower than 10 pT will be harder detection targets for these sensors.
Even if for instance the field of 4 pT at a sensor which is close to the contrast is detected well, the other sensors in the ROI will detect relatively smaller fields due to the fact that they have larger distance from the contrast, and therefore considering the reconstruction noise, there might not be enough information to locate and reconstruct this contrast.

6.3 Reconstructed targets

The reconstruction package calculates the primary and secondary magnetic fields and the Jacobian for reconstructing a general conductivity map.
The results of the inverse problem for two forward model simulations are presented in the following sections. The targets in the ROI are selected to investigate certain aspects of the imaging problem.
For the first target, we try to detect two small conductive elements whose volume sizes are smaller than one percent of the volume of ROI. The inverse problem for this case is done only with one iteration.This example works as a benchmark test for the inverse problem as we change value of an element with a known position to simulate the forward problem and use the calculated magnetic field values for reconstruction, to verify that the inverse problem finds the same element in the reconstruction using the field at the sensors.

This example reveals that small sized perturbations cannot be properly detected in differential imaging, even in the cases of perfect, noise free imaging as the number of voxels is much less than the number of the independent measurements.
The second target is a disk as an estimation of the head shape and volume. The disk has a thickness of 10 cm and contains two concentric regions with properties of certain biological tissue. The outer region is has the properties of the skull and the inner region has the gray and the white matter properties averaged (the true average is used due to their real proportion in the brain). While using the disk as the target, we introduce the lesion alteration by changing the electrical properties of certain elements at the center of the disk in the region which was filled with the white and gray matter. The sensitivity of each sensor is calculated for three different radial position of the disk in the ROI.
For the disk target, the dynamic MIT imaging is done using NOSER which was introduced in previous chapter. The conductivity values calculated for this altered region is 65% different from the original values with an optimized regularization parameter which is almost the same as the state of art devices (Zolgharni *et al.*, 2009a). The simulation results for a disk model as an estimation for the head, dynamic MIT is a promising approach for monitoring the cerebral edema development after the surgery or where monitoring of the brain for fluid is of interest. For the disk model, we solve the inverse problem using iteration as well to compute the absolute values of conductivity. In this case, the absolute value of the conductivity is calculated after 5 iterations the residual error falls below the measurement accuracy, and the iteration stops. The position of the lesion alteration is determined more accurately using the nonlinear approach. However, the computation time is long for the forward problem simulation and calculation of the sensitivity matrix at each step of iteration. This fact suggest that using this method along with an MIT device is not a good candidate to measure the absolute conductivity value considering the computational costs.

6.3.1 Most sensitive direction

As discussed in Chapter (2), one of main challenges in MIT is subtraction of the primary signal. In general, primary field compensation is possible by aligning the detector coils along the magnetic field streamline such that there is no net flux passing through it. In order to reach this goal, we use the sensitivity matrix elements to interpret the direction that is less sensitive to the primary signal.
The sensitivity matrix elements are complex numbers of form : $S{=}S_r{+}\imath S_i$. The real part of the sensitivity shows how sensitive is a sensor to the primary signal or the displacement current. Using the configuration introduced in Fig.(6.1), the vertical sensing surface shown

in red shows lower values of the real part of sensitivity profile compared to the horizontal sensing surface. This means that this sensing direction is less sensitive to the primary signal. As the contribution of displacement current in the secondary field at 50 kHz is small, an optimized direction for the sensor is the one with smallest real value of sensitivity.
This is an optimization method which can be used to find the best configuration and orientations for the sensors. For a symmetrical situation, like the object of interest at the center, choosing a completely vertical set of sensors produces a negligible S_r compared to S_i. The sensor configuration shown in Fig.(2.3) is the optimized sensor configuration (for the object at the center) according to the symmetry of the system. However if the disk is displaced from the center, vertical orientation is not the direction least sensitive to the primary signal.

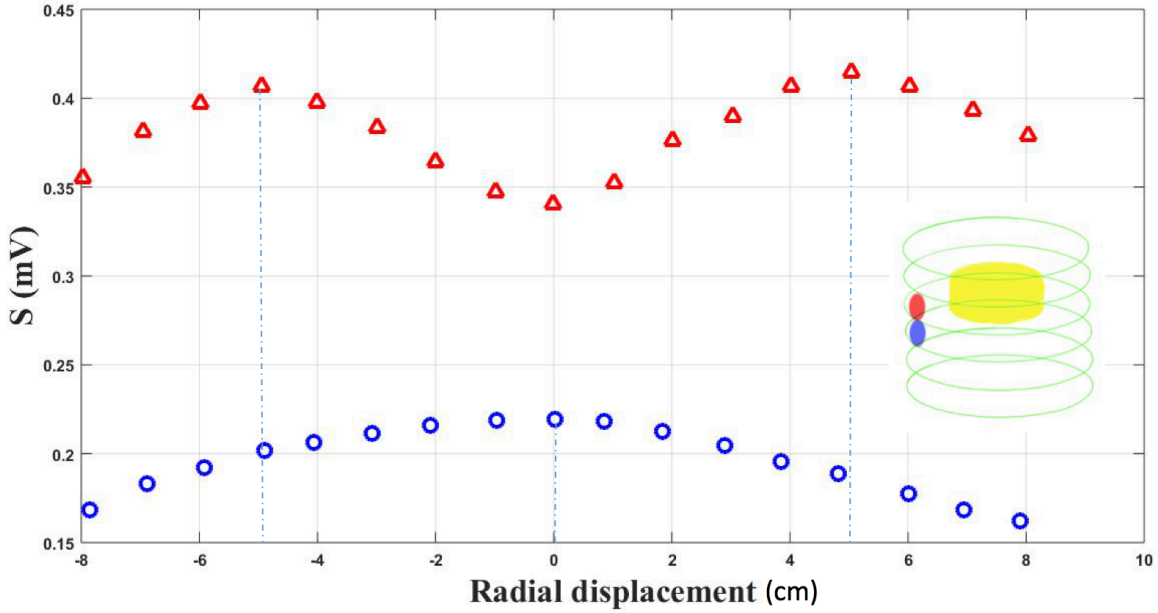

Figure 6.4 Imaginary part of sensitivity profile versus the radial displacement for two sensors at angular position 5 and two different heights. The inset shows the six coils, two detectors and the disk. The red dots are for the sensor between excitation coil 4 and 5 (the same level with the object shown in yellow). The blue dots are sensitivity values for the sensor at the same angular position between excitation coil 3 and 4.

The S_i is the sensitivity to the secondary signal (mainly from the conduction current) which should be maximum for an ideal conductivity measurement. After various simulations of possible configuration, it is observed that this S_i value is not necessarily maximum when sensors

are completely vertical and depends on the location of the object in the ROI, as well as the excitation coil height from x-y plane. Therefore, sensors may be tilted to become more sensitive to some locations in the ROI. Equivalently, different set of sensors rather than the sixteen shown in Fig. (6.2) could be used for this purpose.

Fig.(6.4) shows the imaginary value of sensitivity in m V for two sensors, which are vertically positioned at two different heights from the base of ROI as the object of interest is moved along the x axis (along the radius and toward the center of the cylinder). It can be seen that for the sensor in the red position, the maximum sensitivity happens for around positions b and a while for the blue sensor happens in position c. It is also observed that the overall sensitivity profile for the red sensor is more than the blue sensor, which demonstrate that the signal from sensors located at the same height as the object of interest have major contribution in the reconstruction.

However, for reconstruction of an object at c (shown as a yellow disk directly in front of the red sensor) the blue sensor is also effective and a combination of blue and red sensor provides enough sensitivity along the x axis. However the sensitivity value in the center of the ROI is still lower compared with other positions.

As a future work discussed in Chapter (7), using the sensitivity analysis, an optimized model in terms of the excitation coils location and sensors direction can be developed for a specific conductivity distribution such as in the human head. This model is expected to have a better performance at the center of ROI, compared to the current device. The optimization method (Gursoy et Scharfetter, 2009) works based on the principle of making the rows in the sensitivity matrix more independent by changing the excitation patterns and the sensor orientations.

The symmetry in the current model shown in Fig.(6.1), suggests that for the head located at the center of the ROI, with 6 excitation coils centered at the cylinder axis, the least sensitive direction to the primary signal (the one with most cumulative value of imaginary sensitivity profile at all 80 sensors) is the vertical position. However, this arrangement is suggested base on a limited number of simulations and it is not unique.

6.4 Case I : Two selected elements

Figure (6.5) shows the reconstructed conductivity value for all the elements, when we only change the conductivity of one element. We reconstruct conductivity when we change the conductivity of an element which is located almost at the center of ROI (element number 300) and other one located close to the surface of ROI (element number 3585). Two dif-

ferent locations were chosen for the altered elements to discuss the amount of artifact in the reconstructed conductivity map based on the element distance from the sensors. We set their conductivity to have the value of conductivity of blood. The other elements have the air conductivity (almost non-conductive σ=3×10^{-15} Sm^{-1}). The volume of each element is approximately 0.3% of the total volume of ROI.

The total of 80 sensors on the surface were used to measure the effect of this small size perturbation, with a total of 480 measurements. We have used the same mesh (3840) for the forward and the inverse problem to keep track of the element for the benchmark. We change the conductivity value for this element while keeping the properties for the other elements constant.

In Fig.(6.5).a, the signal corresponding to the reconstructed conductivity value of element 300, the one that was modified, is marked with red dash. Green marked signals in Fig.(6.5).a correspond to reconstructed conductivity for elements which are in fact nonconducting. These elements are mainly neighboring elements of the element 300 which are responsible for the blurring effect.

This behavior is also observed in Fig.(6.5).b when we change the conductivity of element number 3585 marked with red dash and its neighboring elements, which are in fact nonconducting marked with green dash. When the conductivity is changed in both elements and perform the reconstruction, the two signals add, as shown in Fig.(6.5).c.

The element 300 is located at the center of the ROI and therefore further from the sensors compared with the element 3585 which is located close to the cylinder surface. If we refer to the red marked signal as main signal and green marked signal as reconstruction noise in Fig.(6.5).a, and compare it to Fig.(6.5).b, it is evident that the element closer to the surface (3585) is located more accurately as it has a larger value ratio of signal to noise. However, as number of elements contributing to this noise for element 300 is less than that of the other element, the element at the center is less blurred compared to the one close to the sensors.

The sensitivity matrix in this simulation is computed according to the electrical properties of air, assigned to all elements in the ROI. As for the small value of air conductivity (3×10^{-15} Sm^{-1}), the sensitivity matrix is ill-conditioned with a larger conditioning number compared to the sensitivity matrix calculated with the prior information. Therefore, the calculation of the sensitivity matrix for a less conductive background takes longer time than the calculation for a more conductive background.

As a result of this larger conditioning number, the conductivity values calculated for the elements are up to three times their real values (inaccurately), for one iteration. Further, even though the conductivity value is the same for both selected elements, the element closer to the surface of the cylinder (and the sensors) shows a greater conductivity value in the

reconstructed image.

This imposes a limitation in locating small perturbations as the inverse solution in this case can not find the exact location of element. Depending on the cut-off signal we consider for the reconstruction, the number of artifacts in the image changes. This ambiguity is amplified by symmetries present in the relative position of the detection and excitation coils with respect to the voxel (element) being considered.

In producing the conductivity map, the green marked conductive elements in Fig.(6.5) blurs the targeted element. For a symmetrically shaped object, they usually produce rings of less conductive areas around the object of interest. This will make the reconstructed image blurry. Fig.(6.6) shows the element number 3585 and its neighboring elements. The element itself has more conductivity but some less conductive elements (green marked signals) appear around it.

Artifacts are results of the linearization of the numerical solution and the fact that the number of independent measurements made is less than the number of voxels with unknown conductivity (no noise was added in this measurement). It can be concluded that prior information, such as the ranges of the conductivity in the ROI and the position of the disk (head), are important for detecting the change in conductivity with the linear method. We will verify such detection in the next section, while simulating the disk model.

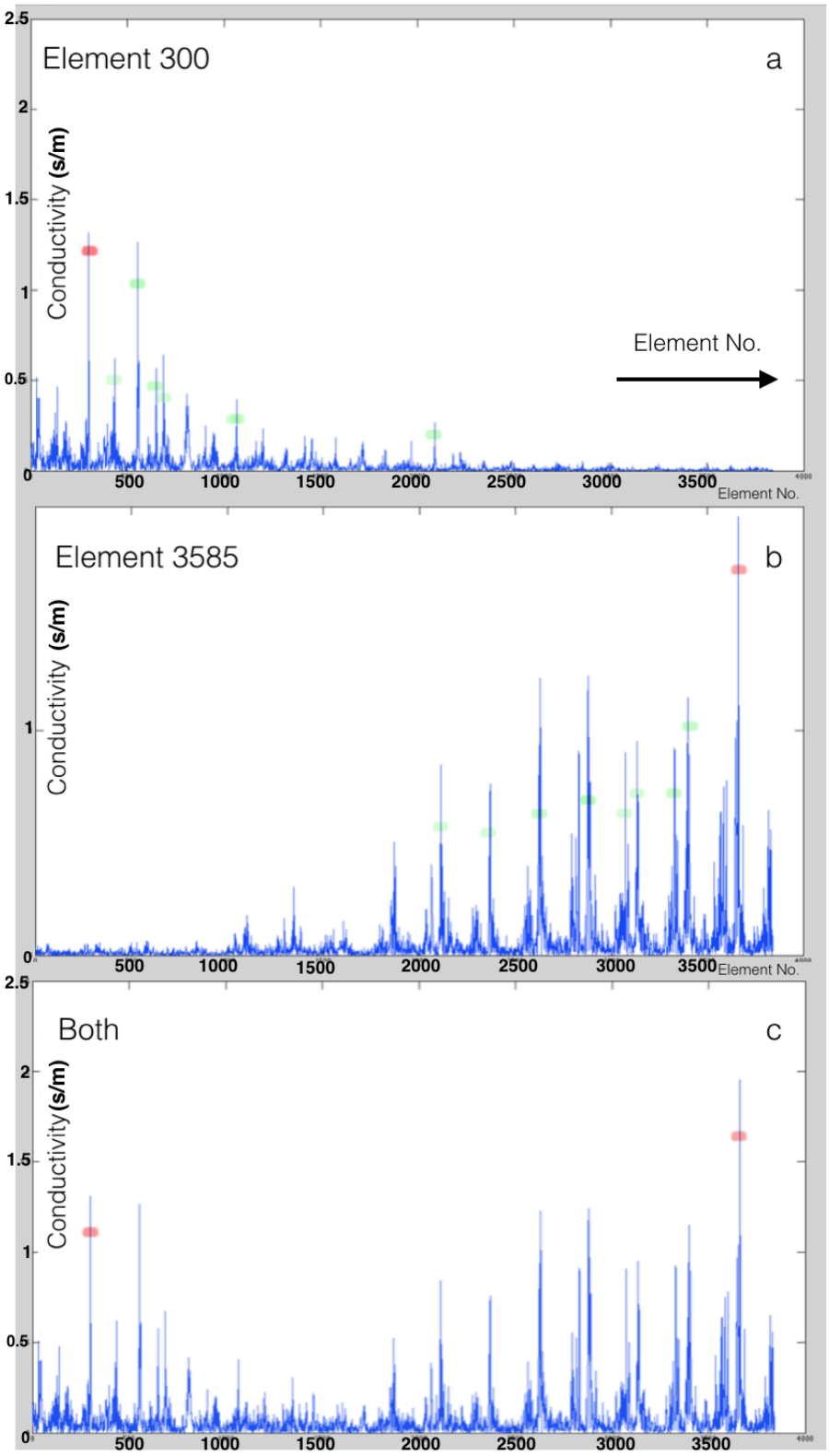

Figure 6.5 Reconstructed conductivity in Sm^{-1} when we change the conductivity of element no.(300) located close to the center of the cylinder (a), Reconstructed conductivity in Sm^{-1} when we change the conductivity of element no.(3585) located close to the outer surface (b), Reconstructed conductivity in Sm^{-1} when we change the conductivity of both elements(c). The marked in red signal is the detected element, while the marked in green signals are the elements which produce the shadow images in reconstruction.

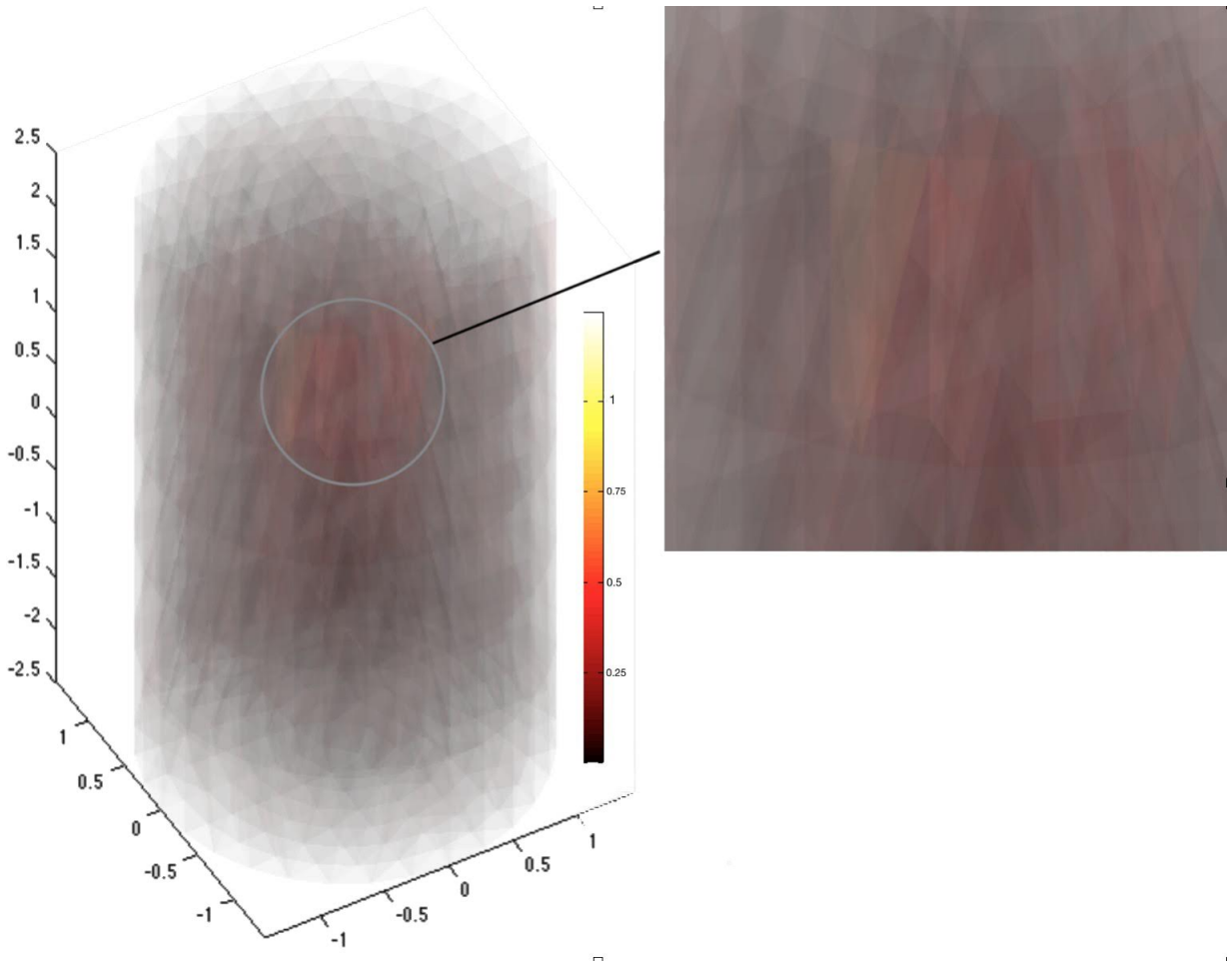

Figure 6.6 Reconstructed image for one conductive element (3585) located on the surface of the cylinder with the conductivity of 0.6 Sm^{-1}. Shadows of the reconstructed elements are less in intensity compared to the element (3585).

6.5 Case II : A disk with two concentric conductive regions

The disk consists of two concentric cylinders with different values of conductivity, chosen to represent an estimation of the head target. The outer ring has the electrical properties of the skull and the inner one has the gray and the white matter electrical properties averaged. The outer radius ratio of the gray matter to skull section is 8 to 10. The sensitivity matrix in this case is calculated with the brain properties as the background for the object of interest. The conductivity and relative permitivity of the tissues given in Table (2.1) were used in calculation of the sensitivity matrix. After calculation of the sensitivity matrix, and also V_p and V_1, a lesion with the volume of 75 cm^3 (5% of the disk volume) is added at the center

of the disk. A constant phase noise level was added to the simulated data before performing the inversion. The level of the noise is determined after the first simulation and using the secondary field value to find a proper level noise. As the signal-to-noise ratio (SNR) is defined as follows :

$$SNR = 20 \log_{10} \frac{U_S}{U_N} \tag{6.1}$$

with U_S being the signal voltage and U_N being the noise voltage, We add 1% of the maximum of $\Delta\phi$ as a reasonable noise value to the simulated data as uncorrelated Gaussian noise which result in 40 dB of SNR.

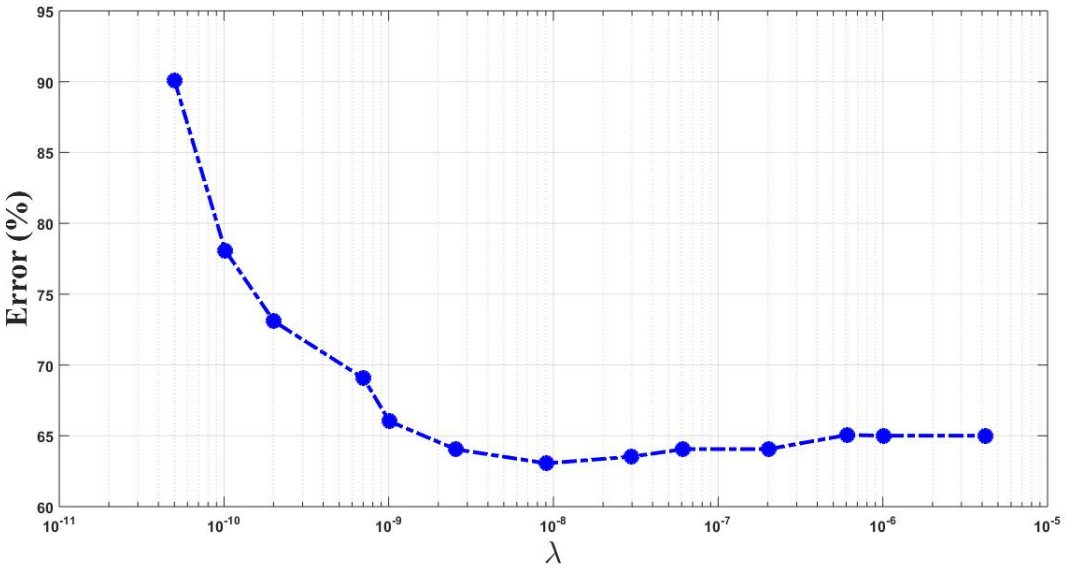

Figure 6.7 Error in (linear) reconstructed conductvity value with respect to the regularization parameter λ.

Different noise levels require different regularization parameters (defined in section (5.2)) in order to obtain satisfying image. Figure (6.7) shows the value of error as a function of the regularization parameter λ. The parameter is optimized by computing the error by the following formula :

$$E = \frac{\| \Delta\sigma_{true} - \Delta\sigma_{rec} \|}{\| \Delta\sigma_{true} \|} \tag{6.2}$$

where $\Delta\sigma_{true}$ is the vector with all the true values of the conductivity used in the forward problem and $\Delta\sigma_{rec}$ is the vector for all the reconstructed conductivities. The sign $\| \cdots \|$ shows the L_2 norm and the error value is plotted as percentage. The minimum error in the

conductivity value happens when the regularization parameter λ has the value 2×10^{-8}, which corresponds to 63% error in calculating the conductivity value, using the linear approximation.

6.5.1 Phase change due to modeled cerebral edema development

The phase change $\Delta\phi$ is computed for the 16 sensors at the same level as the disk and for three positions. The phase change values, $\Delta\phi$ are shown in Fig.(6.8) along with their corresponding disk positions. The value of the phase change for all the three cases are in the range of milli-degrees. This phase change is only according to the development cerebral edema and as may be seen in the figure, The maximum value of $\Delta\phi$ falls off as the disk gets further from the sensor as the inductive coupling of lesion and the detection coil is less according to their distances. This phase change value is much larger for the head itself as an alteration. The phase change relative to the empty detector volume when the disk without the lesion was introduced ($\frac{V_1}{V_p}$) has the maximum of 1403 m^o (milli-degrees).

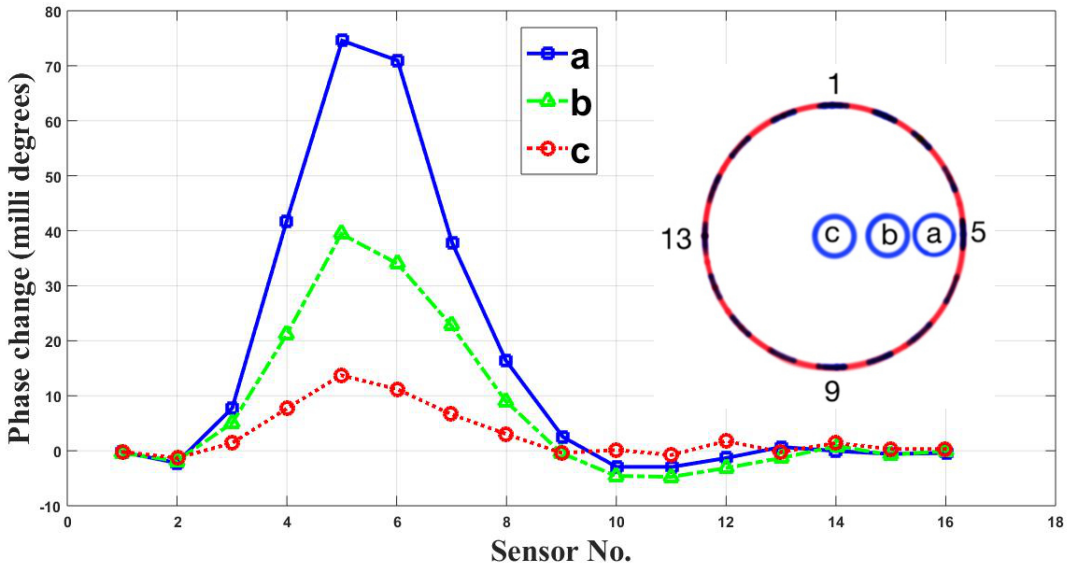

Figure 6.8 The phase change $\Delta\phi$ in each sensor measured at the same level with the disk, for positions : a in red, b in blue and c in green.

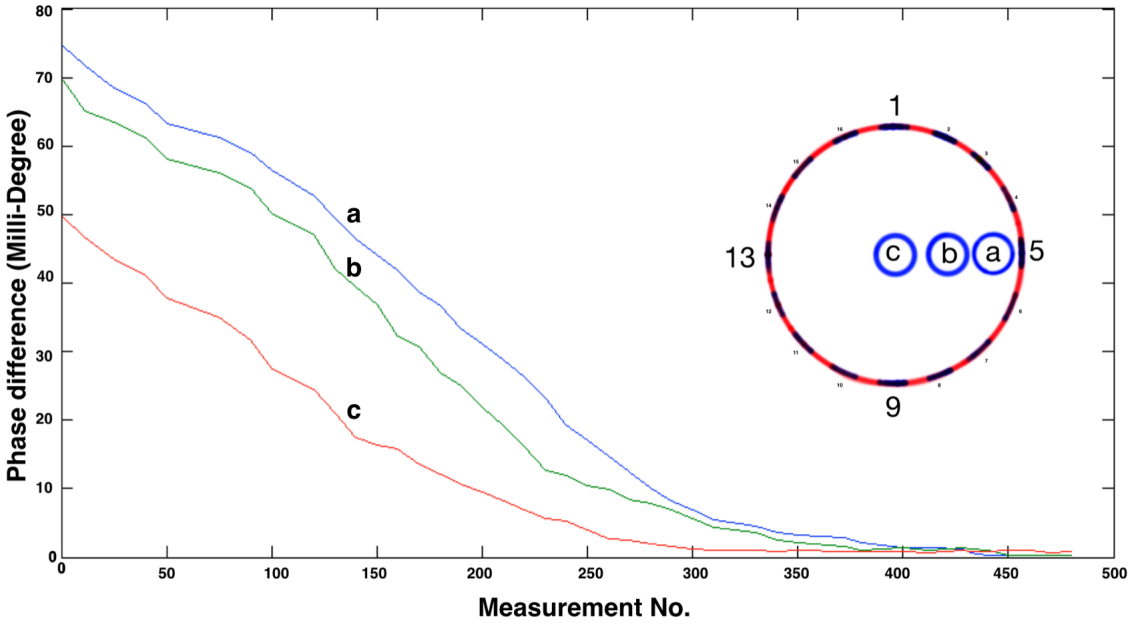

Figure 6.9 The phase change detected in each measurement for positions : a in blue, b in green and c in red. Data is sorted from largest to smallest.

In modeling of the disk with the lesion at position a, 31% of the signal or 149 of the total 480 measurements done ranged between 20 m^o (milli-degrees) to 74 m^o in $\Delta\phi$. From the detected signals, 71% or 340 measurement are above 3 m^o.

In this case, 1% of the maximum signal which is about 1 m^o is added to the data in form of a Gaussian noise, before they are used for the inverse problem. The distribution of the phase change versus the number of measurement is given in Fig.(6.9) for the three different positions. The poorest performance in terms of the detected phase change is when the object located at the center, as it have the maximum distance with the detectors. However, even in this case 20 % of the signals are above 20 m^o.

Figure (6.10) shows the calculated conductivity profiles that were obtained using the detected phase change. It shows how the conductivity changes as we move along the x axis at the same z level with the disk. The conductivity distribution for position b is more widespread than the others, which indicates that the spread of lesion in the reconstructed image of the conductive area is larger at this position. At position c, it is observed that the conductivity is not computed to be zero on the walls of ROI (contrary to the model), which will produce shadows of the conductive area on the walls of ROI that can be seen in Fig.(6.10).

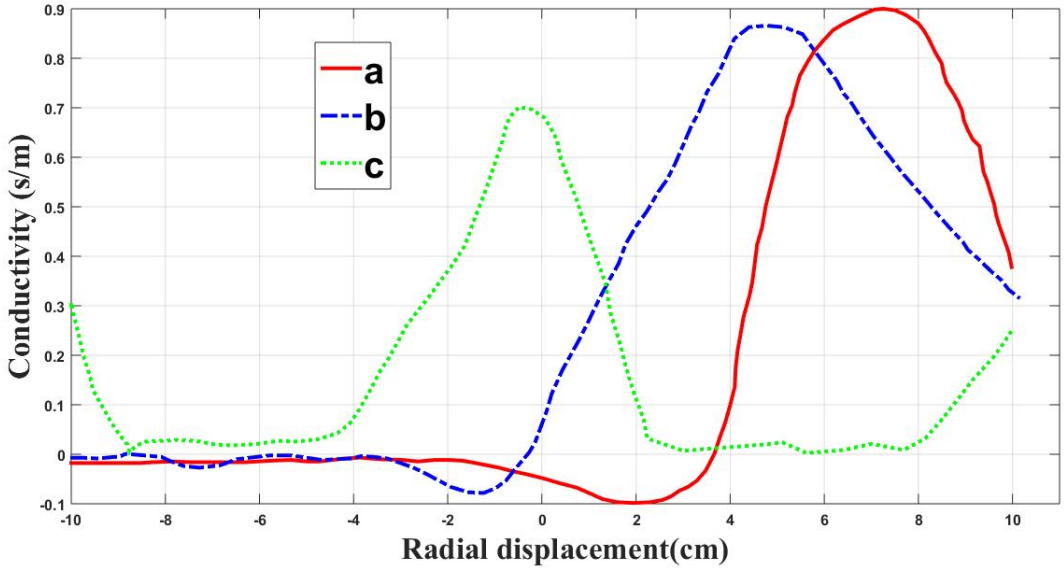

Figure 6.10 The conductivity profile computed at z=10 cm (between coils 4 and 5) at the same level with the disk as the fuction of the radial displacement r.

6.5.2 Linear reconstruction of the conductivity map in 2D

With the optimized regularization parameter the inverse problem is solved for the targets shown in the Fig.(6.12) and the reconstructed conductivity map is given in Fig.(6.13) . The conductive area which can be seen for all the three cases, is indicative of cerebral edema developed within the skull. The value of the reconstructed conductivity for the lesion is off by 63% from the actual value. This issue is the direct result of linearization of a non-linear problem. We can use iterations to find the correct value of conductivity for this area. For our objective, which is monitoring the contrast, results in Fig.(6.13) are sufficient to admit the presence of the lesion. However, the model still lacks the precise resemblance of the disk to the human head and further investigation with a real head model, which is necessary for this confirmation.

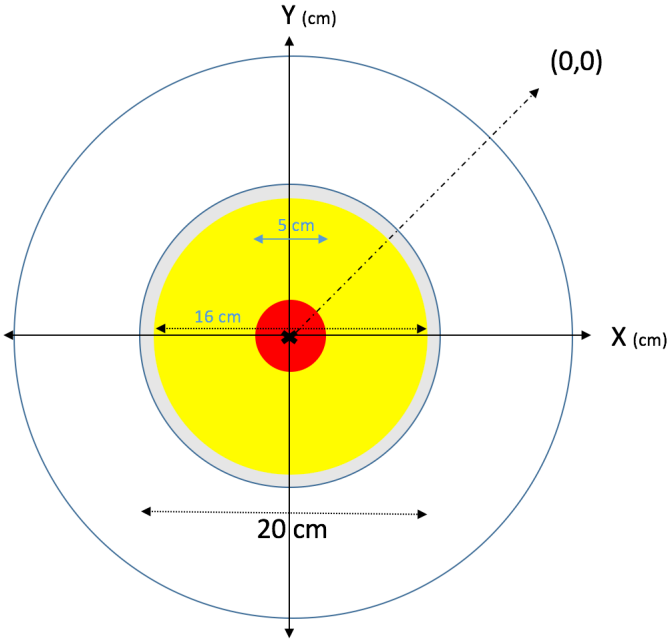

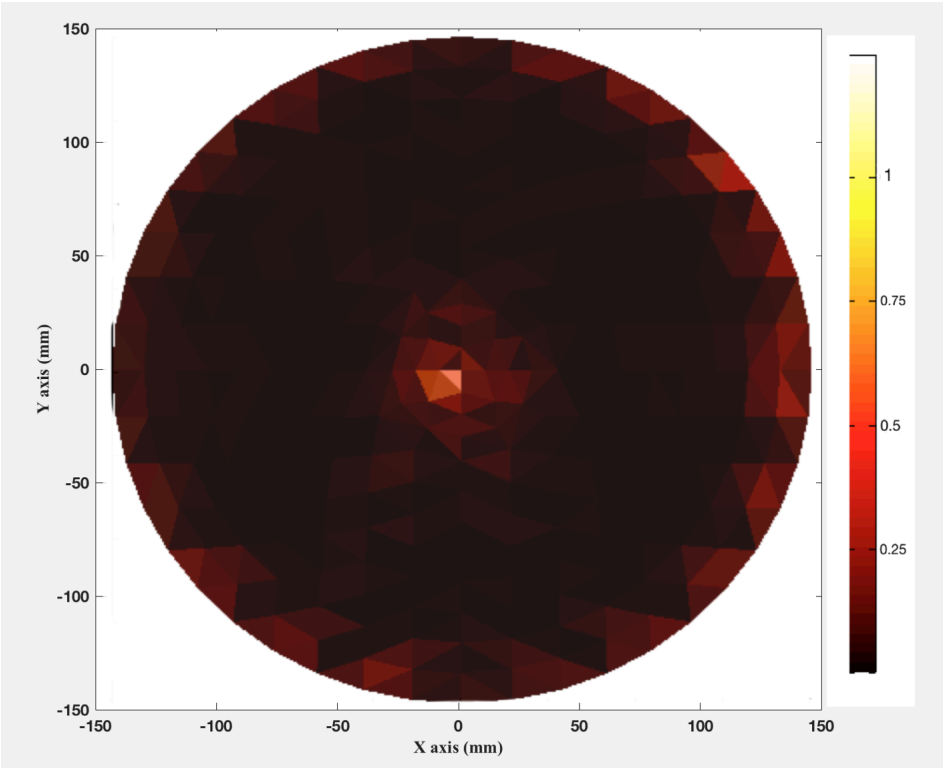

Figure 6.11 The lesion modeled at location c and its linear reconstruction conductivity contrast map in 2D

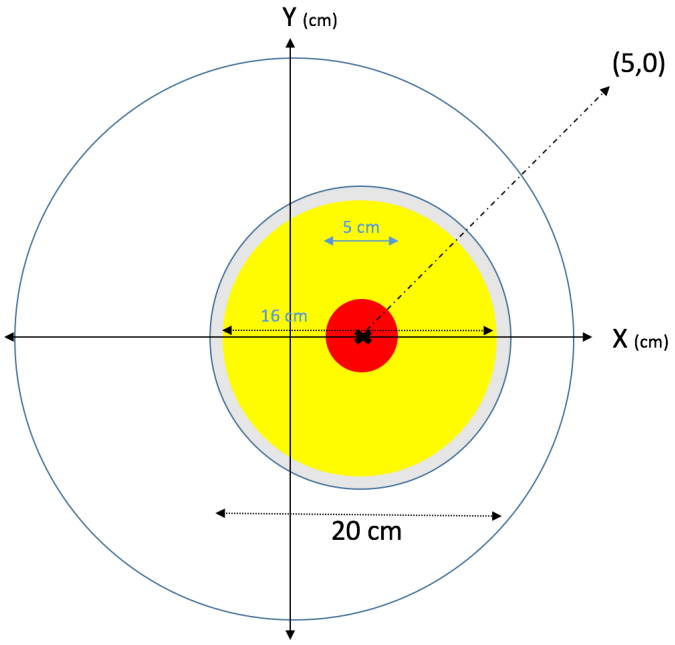

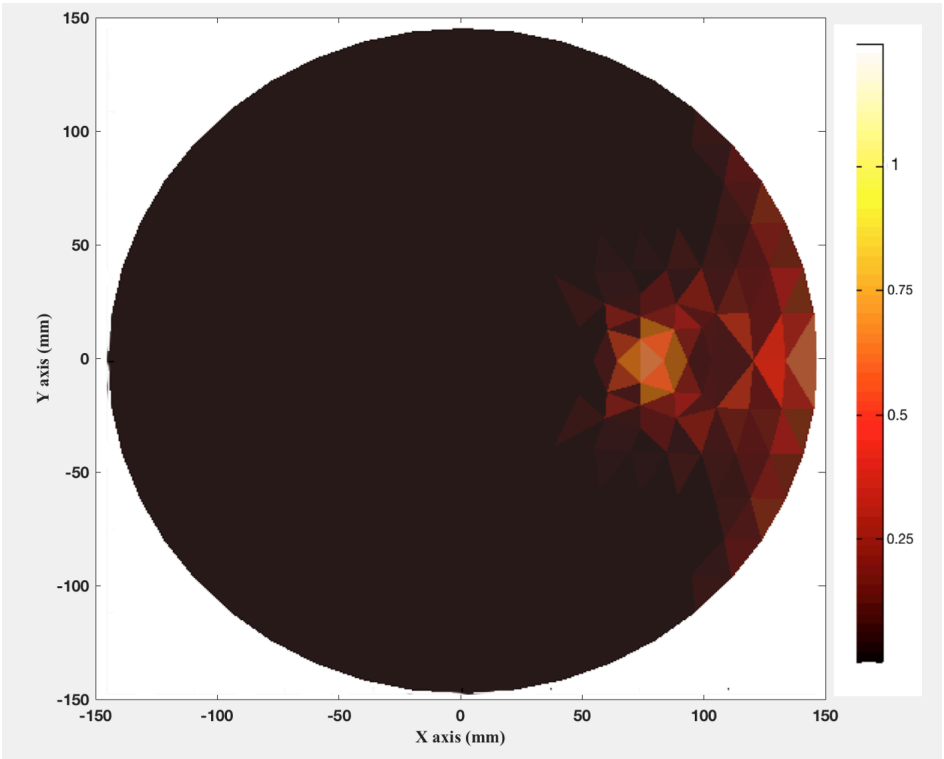

Figure 6.12 The lesion modeled at location b and its linear reconstruction conductivity contrast map in 2D

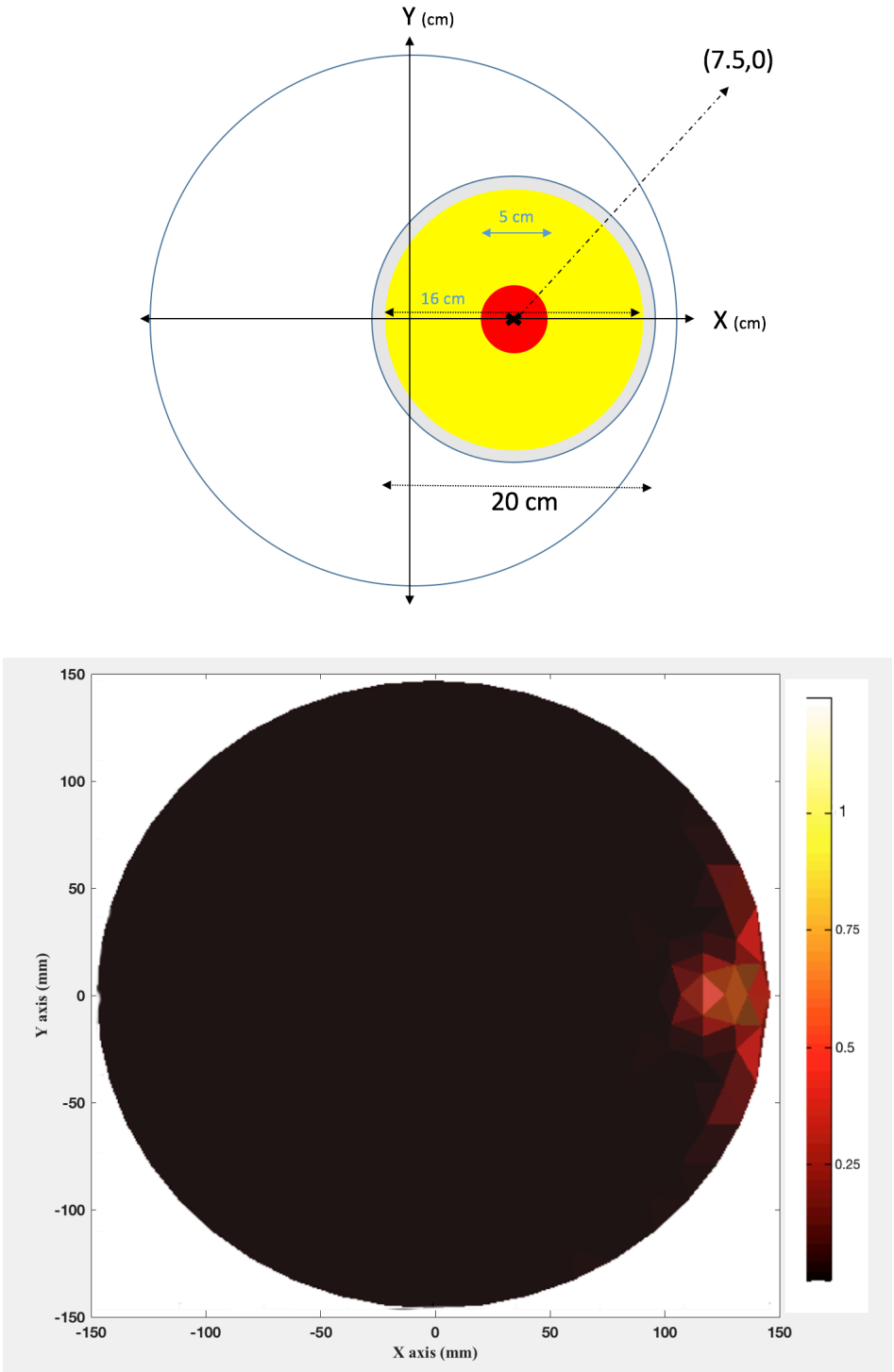

Figure 6.13 The lesion modeled at location a and its linear reconstruction conductivity contrast map in 2D

6.5.3 Linear reconstruction of the conductivity map in 3D

Fig.(6.14) shows the result of the linear reconstruction of the conductivity map in 3D for the same arrangements, with the disk at three different locations. The shadows appearing around the surface of ROI, indicating those elements in the map is the result of the linearization of the problem (they do not appear in the non-linear model).
There are more shadow elements in the reconstructed conductivity map when the object of interest is at a position which is more symmetrical with respect to the sensor positions (at c).

6.5.4 Nonlinear reconstruction of the conductivity map in 3D

Fig.(6.15) shows the nonlinear reconstruction of the same target with the lesion inside the disk. In this case, we have only considered position c which showed the lowest signal value and applied iteration to find the correct value of conductivity.
In each iteration, the sensitivity is re-calculated and the iteration continues until the difference between the reconstructed conductivity and the true value is less than 1 percent. Fig.(6.16) shows how the answer converges in each step. The error in Fig.(6.16) is computed using Eq.(6.2).

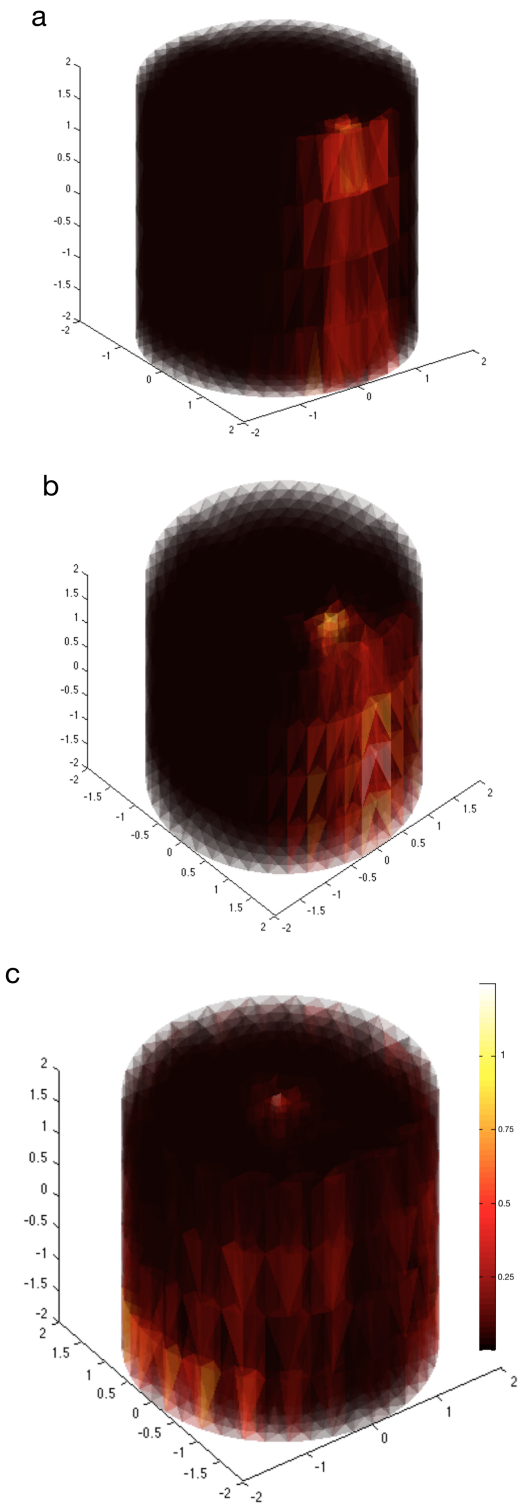

Figure 6.14 Linear reconstruction of the conductivity map in 3D for the lesion at three different locations of ROI.

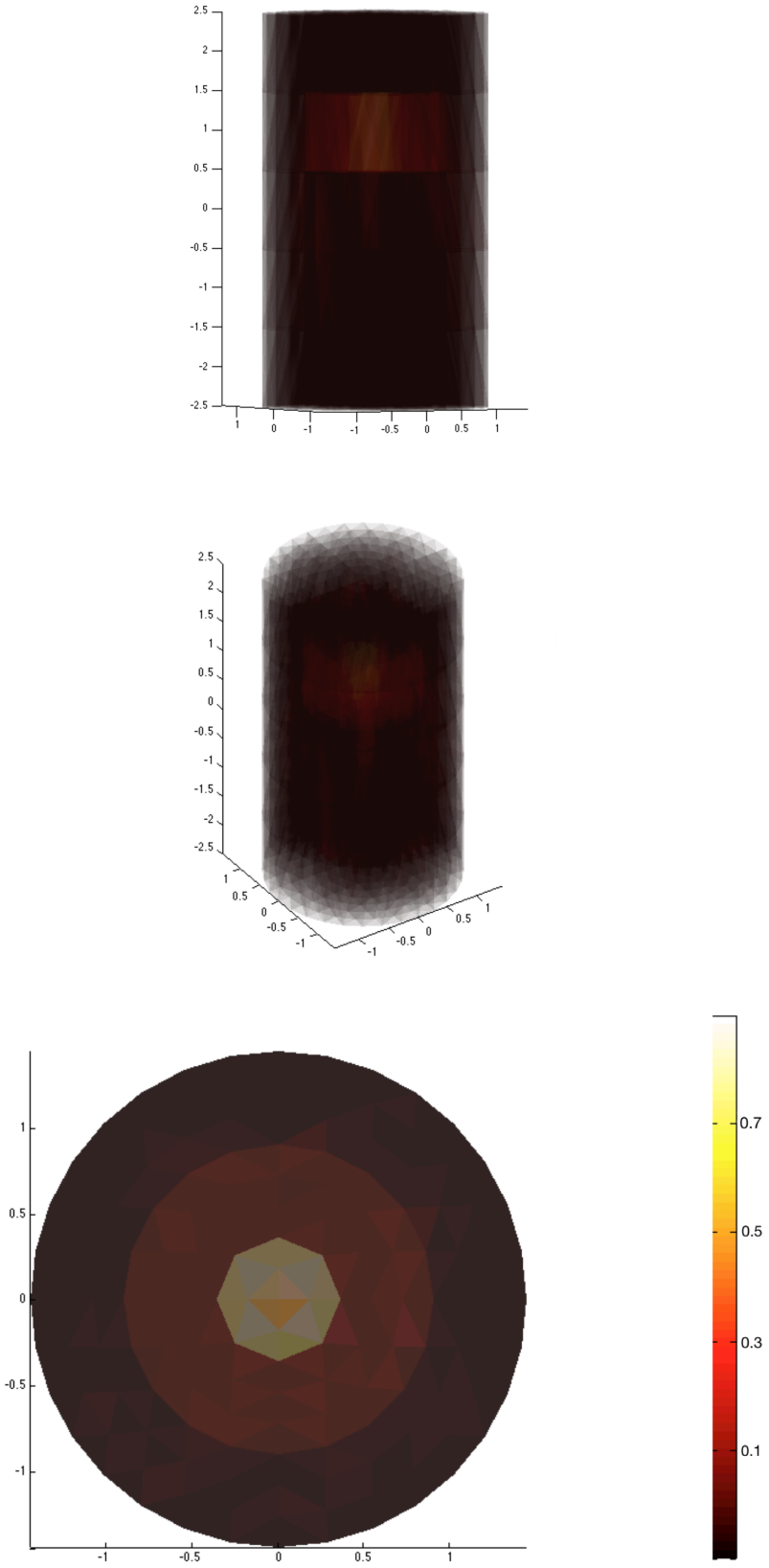

Figure 6.15 Nonlinear reconstruction of the conductivity map in 3D for a disk with the lesion at the center of ROI.

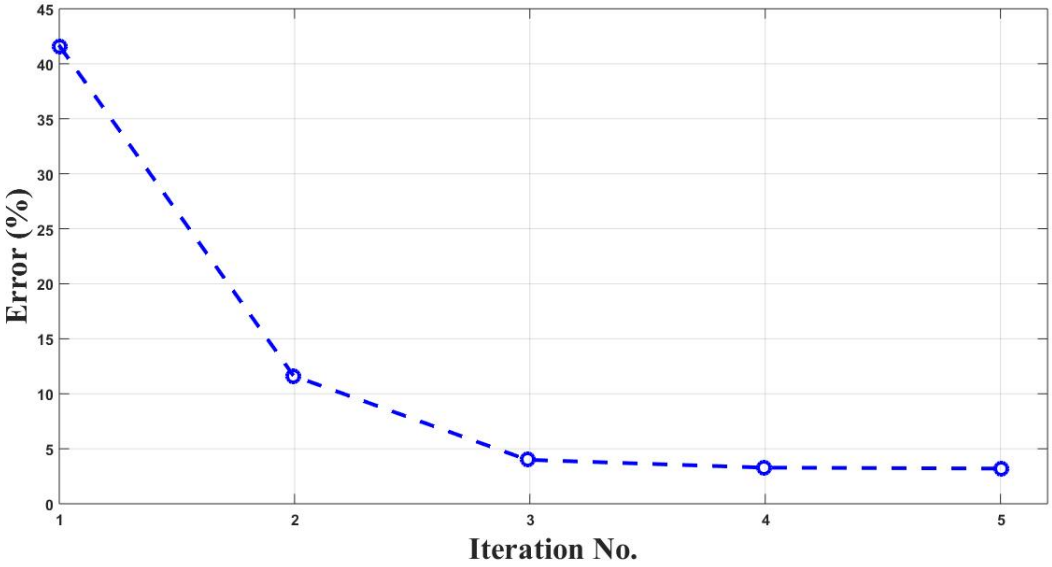

Figure 6.16 Error in the calculated conductivity value in each iteration step.

6.5.5 Calculation of the primary and secondary magnetic field

The values for the primary and secondary magnetic field measured in each sensor are shown in Fig.(6.17) and (6.18) at 50 kHz, while 1 A current is running in each excitation coil. The primary field (of order 10^{-5} Tesla) shown in Fig.(6.17) , for the case that all excitation coils are running. Even thought the primary field is stronger in the middle of the cylinder with its direction mainly along the cylinder axis, sensors located in the middle will read lower signals compared to the sensors at two ends of the cylinder, where the magnetic field is not uniform and have a noticeable flux inside the coils.

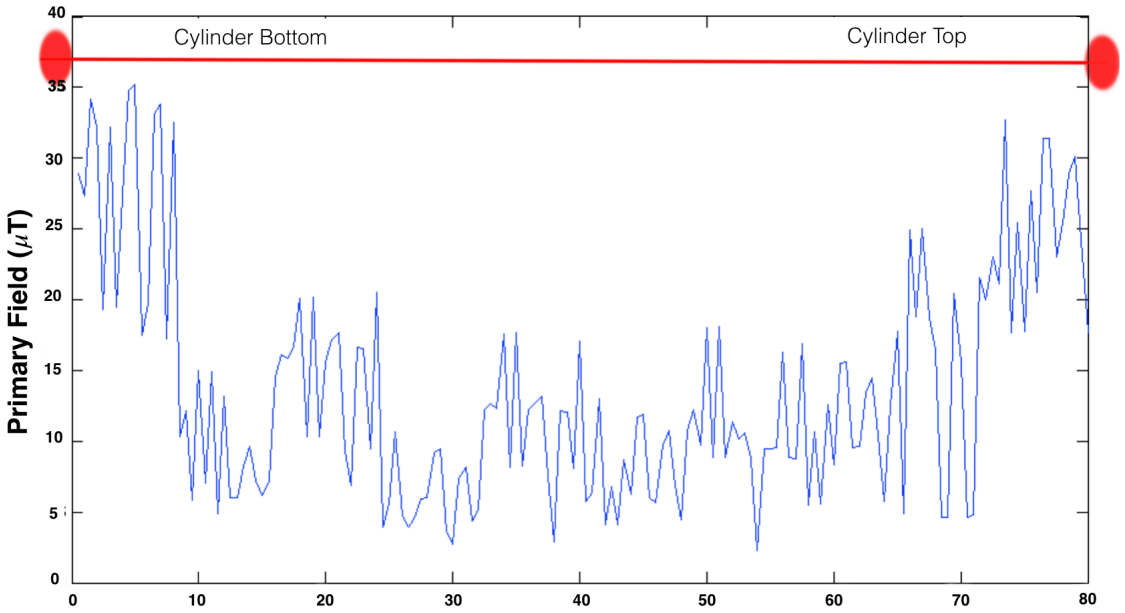

Figure 6.17 The primairy **B**-field value for each sensor (1 to 80) while all excitation coils are running.

In Fig.(6.18), the green cylinder shows the actual position of enumerated sensors around the ROI. The Secondary magnetic field is shown in Fig.(6.18) while the current is running in coil number 1, which is the farthest induction coil from the object and will produce the minimum values of the secondary magnetic field in all the sensors, as a result of its maximum distance from the disk. Sensors in the middle and the top row are the most effective sensors in the reconstruction.

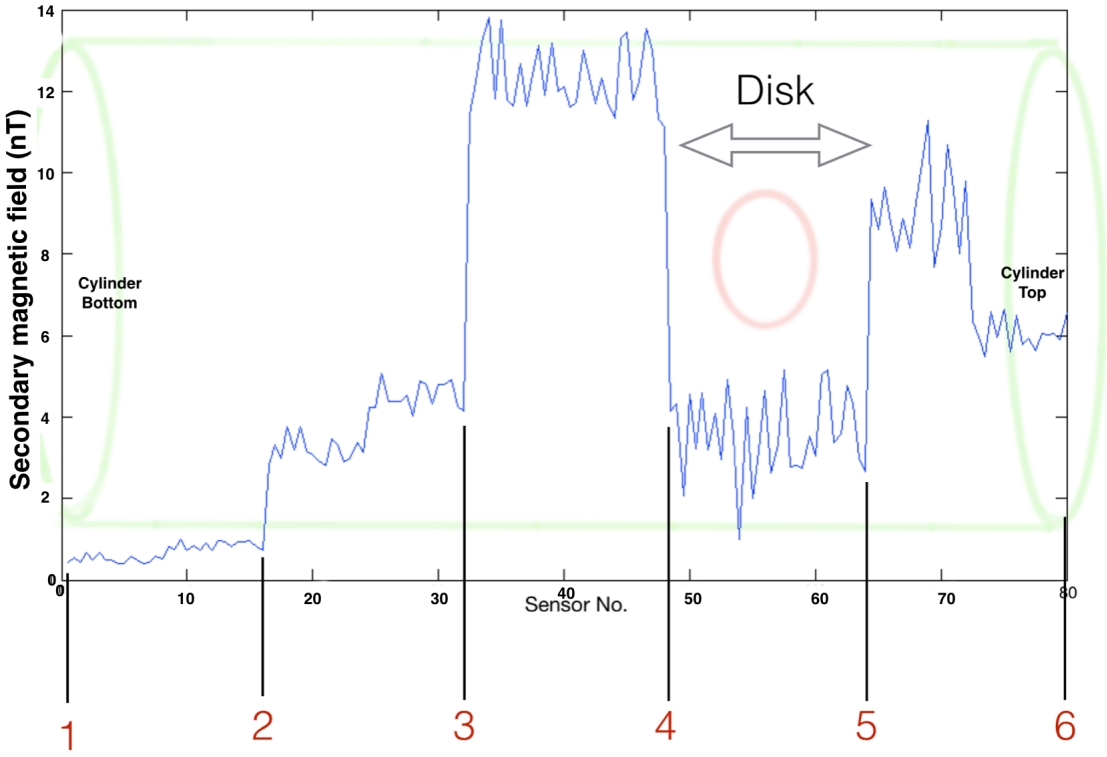

Figure 6.18 The secondary **B**-field in the presence of the disk without the lesion for each sensor (1 to 80) while current is running in coil number 1.

The signal which should be detected for conductivity reconstruction is the difference that the lesion causes in this secondary field. That difference field is shown in Fig.(6.19) using a 2D graph, and in Fig.(6.20) using the cylinder surface to represent the alteration of secondary magnetic field in each sensor. This field is in the pico-Tesla range.

Magnetic sensors used for this device should be able to detect magnetic field changes of the order of some pico-Tesla. GMI sensor with 100 μT field range and the noise level of 10 $\frac{pT}{\sqrt{Hz}}$ can be integrated with the device for such performance (Dufay *et al.*, 2013a). In addition their small form factor (microwires as the sensing element) could allow for a large density of sensors, possibly leading to much better spatial resolution.

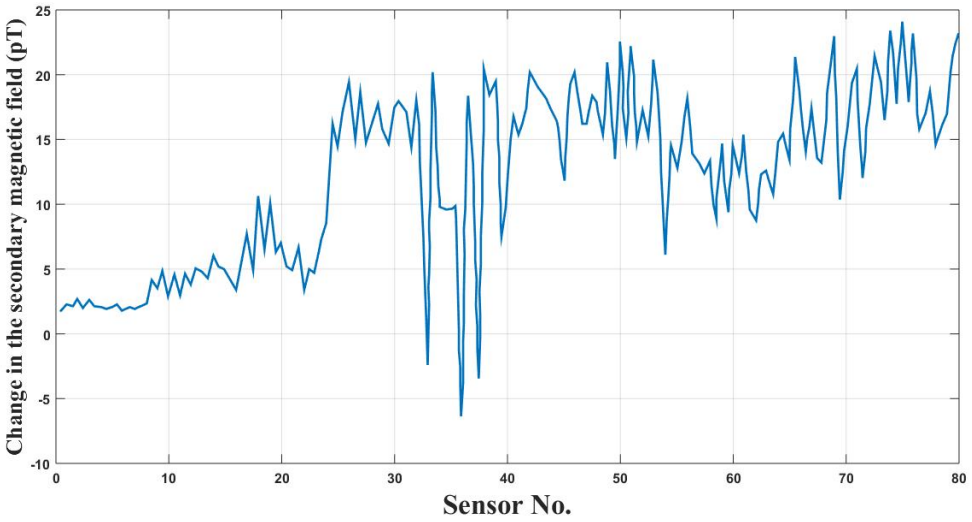

Figure 6.19 The change in the secondary field signal measured for each sensor produced by the lesion at the position *a*.

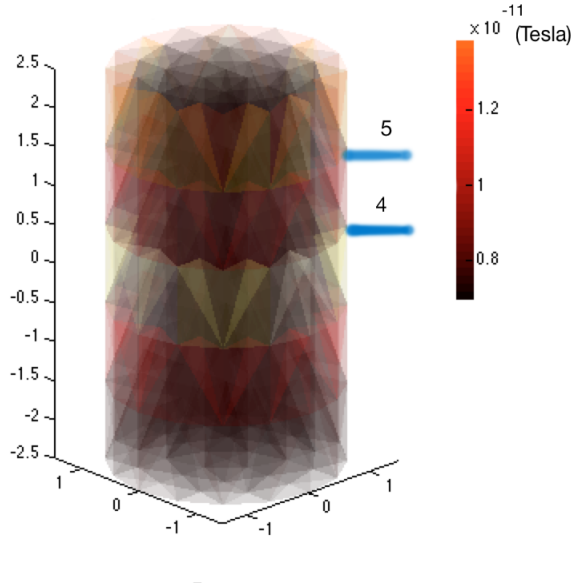

Figure 6.20 The change in the secondary field signal for each sensor, produced by the lesion at the position *c*. The cylindrical representation shows the location of the disk (between coils 4 and 5) and corresponding field difference at each sensor (the surface elements of the cylinder) when excitation coil 1 is running.

6.5.6 Signal absorption rate (SAR)

For safety reasons, it is important to calculate the amount of power absorbed by tissues from the electromagnetic field. Even though tissue heating is known to be negligible in MIT (Holder, 2004), we can use our forward model to calculate its value. The specific absorption rate SAR which can be calculated using wave-matter interaction theory for a material is given by

$$SAR(x) = \frac{\sigma(x)|E(x)|^2}{2\rho(x)} \tag{6.3}$$

where ρ_M is the mass density of the tissue and which is 1850 (kgm^{-3}) for skull and 1030 (kgm^{-3}) for the white or gray matter. In order to obtain a rough estimate of SAR and its dependency on the driving field amplitude and frequency, let us assume a long cylinder of radius a, characterized by a conductivity σ . It is submitted to a uniform longitudinal sinusoidal alternating field of amplitude H_0 and angular frequency ω, such as would be produce by a long solenoid around the cylinder. Using Faraday law, the electric field at the surface (where the field is maximum) is calculated to be

$$E = \imath\frac{\omega\mu_0 a}{2}H_0 \tag{6.4}$$

and the maximum average power density dissipated in Wkg^{-1} is

$$P = \frac{\sigma E^2}{2\rho_M} = \underbrace{(\frac{\omega\mu_0\sigma}{2})}_{\frac{1}{\delta^2}}(\frac{\omega\mu_0 a^2}{4\rho_M})H_0^2 = (\frac{\omega}{2\rho_M})(\frac{a^2}{\delta^2})(\frac{\mu_0 H_0^2}{2}) \tag{6.5}$$

This estimation hold for the quasistatic case ($\delta \gg a$), which is verified in our case and it assumes a uniform excitation field and conductive object, which could be justified in a rough estimation. Estimating the field by $H_0 = \frac{NI_0}{L}$, we have :

$$SAR = P = \frac{\sigma E^2}{2\rho_M} \simeq= (\frac{a^2}{L^2})\frac{\mu_0^2}{32\rho_M}\sigma\omega^2 N^2 I_0^2 \tag{6.6}$$

Therefore, the SAR is proportional to the square of the induction current, the number of turns in the excitation coil (N) and the frequency. For a fixed value of the frequency, one can increase the induction current or the number of turns to produce stronger secondary magnetic field until it gets limited by the electronics (for example the induction coil resis-

tance), provided that the SAR for tissues do not go above the safety limits. The International Electrotechnical Commission (IEC) requirement for MRI scanners, place a limit of 10 watt per kilograms for the head averaged over 6 min.

Using our full Maxwell's forward model, we can calculate the electric field anywhere in ROI (without any approximation) and use Eq. (6.3) to calculate the SAR. The computed SAR with exciter 4 activated with current of 1 A (excitation current) which is known to provide the strongest field in the disk has the maximum of 1.8×10^{-4} Wkg^{-1} (watts per kilogram) at the disk center for the gray matter (with the conductivity of 0.15 Sm^{-1}) and 5×10^{-5} Wkg^{-1} on the circumference of the disk for the skull (with the conductivity of 0.035 Sm^{-1}).

Thus the SAR calculated for MIT at this frequency is many orders of magnitude lower than this limit and therefore this MIT device will produce negligible heating and is safe to be applied for monitoring due to its low absorption rate. This result shows that we can increase the excitation current in our device to get stronger secondary magnetic field at 50 kHz and still be working in a safe SAR zone.

By considering the short term exposure limit of 10 W/kg, we could potentially increase the factor (NI) by a few hundreds (~ 300) and still be within the safe exposure limit (see Eq.(6.6)). Therefore, there is still room for improvement in the amplitude of the secondary magnetic field at 50 kHz using more number of turns in the excitation coils. If we chose to stay on the safe side and consider the long term environmental exposure for SAR which is 0.08 W/kg (Ahlbom *et al.*, 1998) for the whole body, we can still have a 20-fold increase in the primary field, which should result in a 20-fold increase in the secondary field.

Finally, if we increase the frequency from 50 kHz to 1 MHz, Eq.(6.6) shows a 20-fold increase in SAR. However, for a magnetometer such as GMI, the gain in SNR operating from 50 kHz to 1 MHz would be far less than that. This subject should be more investigated in future works.

6.6 Comparison between two methods of calculating the sensitivity matrix

The reconstruction result is directly influenced by the accuracy of the sensitivity matrix. Fig.(6.21) shows the reconstructed conductivity of the lesion located at position c (center of ROI) obtained using two different sensitivity matrix $\mathbf{S}_\sigma$ (direct method) and $\mathbf{GS}_\sigma$ (reciprocity theorem). The reconstruction error is calculated using Eq.(6.2) and an optimal regularization parameter is found for each method ($\lambda_S = 8 \times 10^{-8}$ and $\lambda_{GS} = 7 \times 10^{-13}$). As it can be seen in Fig.(6.22), the reconstruction error for the direct method is 63% and 68% for the reciprocity theorem. Therefore, the image reconstructed using the reciprocity theorem contains

more artifacts compared to the direct method.

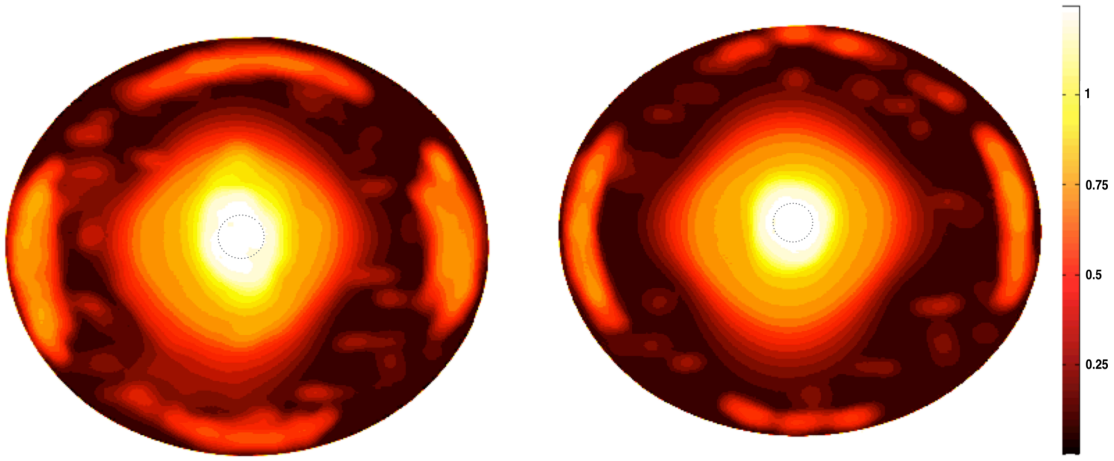

Figure 6.21 Reconstructed images of the conductivity distribution in Sm^{-1}, using $\mathbf{S}_\sigma$ calculated with the direct method on the right and $\mathbf{GS}_\sigma$ calculated using the reciprocity theorem on the left, for position c.

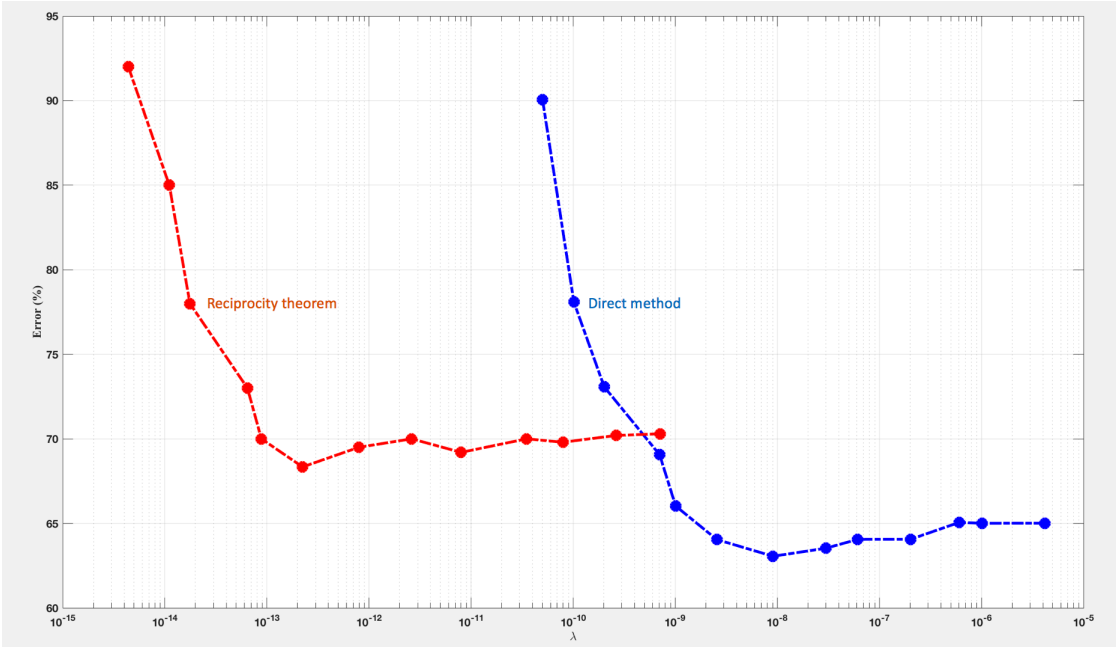

Figure 6.22 Error in reconstructed conductvity value with respect to the regularization parameter λ for reconstrctions using direct method and reciprocity theorem.

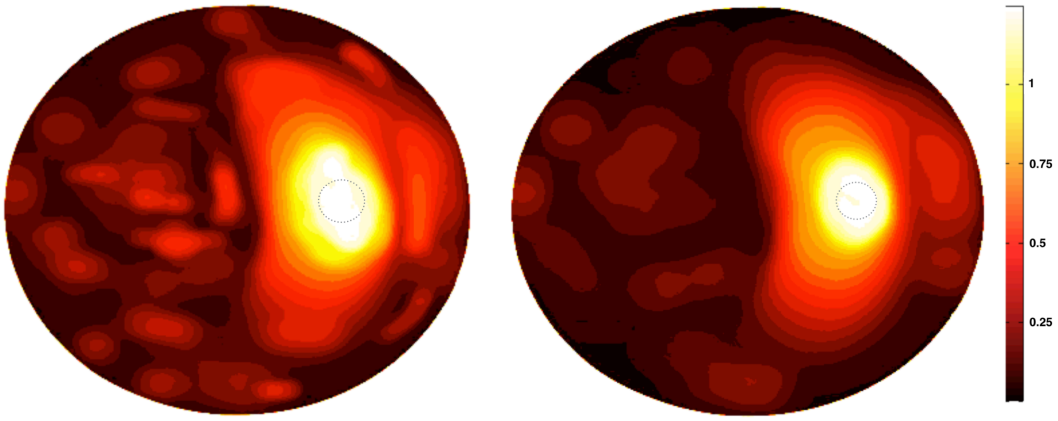

Figure 6.23 Reconstructed images of the conductivity distribution in Sm^{-1}, using $\mathbf{S}_\sigma$ calculated with the direct method on the left and $\mathbf{GS}_\sigma$ calculated using the reciprocity theorem on the right, for position b.

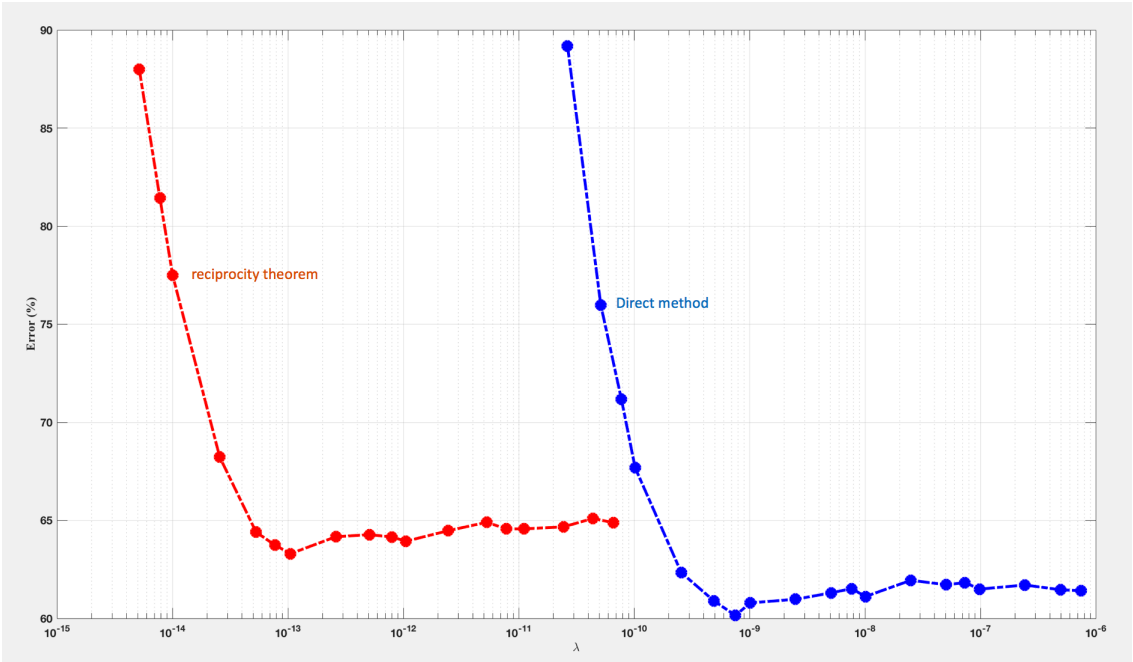

Figure 6.24 Error in reconstructed conductvity value with respect to the regularization parameter λ for reconstrctions using direct method and reciprocity theorem.

Fig.(6.23) shows the reconstructed lesion located at position b using two different sensitivity matrix $\mathbf{S}_\sigma$ (direct method) and $\mathbf{GS}_\sigma$ (reciprocity theorem). Fig.(6.24) shows their corresponding errors in conductivity calculation, while they are reconstructed using different re-

gularization parameter. At the value of the optimized parameter, the reconstruction error is minimum and in this case the error is 60% for the direct method and 64% for the reciprocity theorem. Therefore, the image reconstructed using the reciprocity theorem contains more artifacts compared to the direct method.

6.6.1 Comparison of point spread function (PSF) and spatial resolution

In order to provide a more quantitative comparison between the two methods we use the concept of the point spread function (PSF).The method for calculation of PSF is presented in Appendix (B). We can characterize the resolution of the MIT imaging with Raleigh criterion. Accordingly, two point shaped perturbation are still separable if their PSF overlaps in such a way that peak of the first one coincides with the first zero crossing of the second one. In the case of sinc-shaped PSF the lowest separable distance is equivalent to the 64% width of PSF (Scharfetter *et al.*, 2006).

We calculate the PSF using the sensitivity matrix used for each method rather than a graphical analysis. Therefore, the PSF in MIT depends on the location of the perturbation, the geometry of the object under investigation and the regularization factor used in calculating the inverse of the sensitivity matrix. Furthermore, in MIT the PSF is not isotropic function which varies the same in all directions and therefore the resolution is anisotropic. This will result in different spreading and resolution along X and Y direction.

The PSF and resolution for both direct and reciprocity theorem methods, which were calculated on this finite element model, were mapped to a cubic grid. Mapping is done by assigning the value in the respective finite element to the nearest cube (the distance between their center of gravity is minimal). The resolution for the particular voxel is calculated by the means of 64% width of the PSF (resolution = $1/\text{width}_{PSF}$) with the units (1/mm) as a function of the radial position within the cylinder. In short, the PSF reflects how much a point image is blurred and distorted and the width of the PSF is an indicator of the smallest feature that can be spatially resolved by the device operating in the simulated conditions.

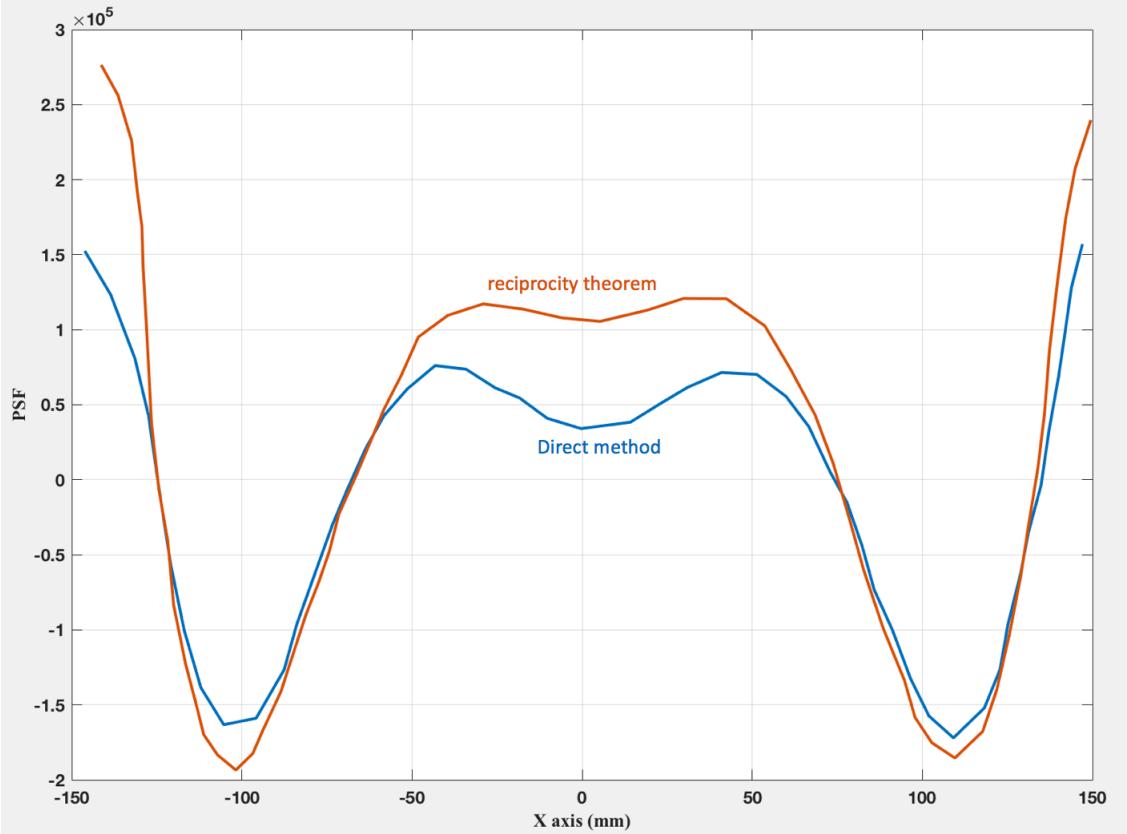

Figure 6.25 The PSF for the direct method and reciprocity theorem method for the point [0,0,0].

We calculate the PSF for all the cubic voxels at the position x=[-150 :5 :150] (x between -150 mm and 150 mm step 5 mm), y=[-150 :5 :150] and z=[-150 :5 :150] for each method. Then we evaluate PSF at position [0,0,0] which represent the location c and at position [5,0,0] which represent the location b for each method. Then we calculate the resolution for each method. The PSF for the direct method and reciprocity theorem method for the points [0,0,0] and [5,0,0] are shown in Fig. (6.25) and Fig. (6.26). These figure can be interpreted as follows : If there is a point perturbation at position [0,0,0] or position [5,0,0], how this point is going to spread in the ROI. Fig. (6.25) shows the spread of the point perturbation at position [0,0,0] toward the edge of ROI, which justifies the side artifacts appears in Fig.(6.21) at in that region. The same is true for Fig. (6.26) and the aritfacts in Fig.(6.23).

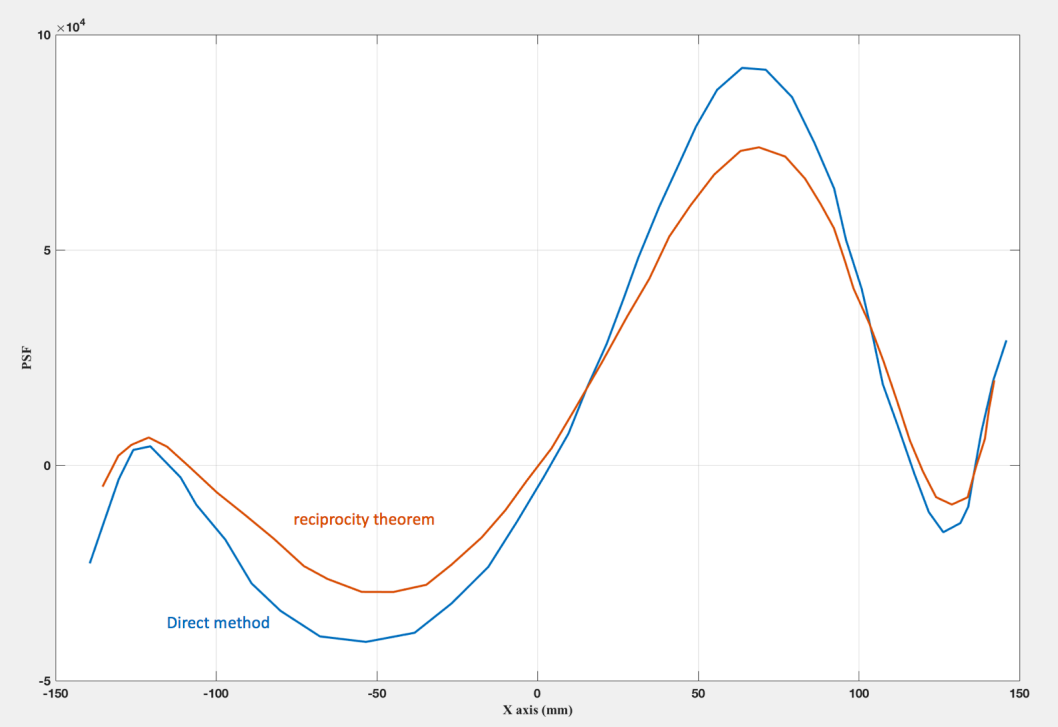

Figure 6.26 The PSF for the direct method and reciprocity theorem method for the point [5,0,0].

The resolution as a function of the radial position of a point object within the cylinder for both method is depicted in Fig. (6.27). The reciprocal of the resolution is around 40 mm in the center and 20 mm close to the surface. As it can be seen in the figure, the direct method shows better resolution overall and specifically at the center point [0,0,0] (location c) and also at [5,0,0] (location b), where the comparisons were made between the two methods.
Scharfetter (Scharfetter *et al.*, 2006) has calculated the normalized resolution (inverse of the ratio between the Raleigh-width and the cylinder radius) using reciprocity theorem method for a device (one array of 16 excitation coils and 32 detection coils arranged around a cylindrical ROI with a radius of 125 mm) simulated at 100 kHz for different regularization methods. Comparing the calculated resolution for the Tikhonov regularization method (same as ours) of the Scharfetter device at 100 kHz with our device, shows significant improvement of the resolution in the region between 50 mm radius and 100 mm radius region.
For instance, exactly at the center [0,0,0], the value of the resolution reported by (Scharfetter *et al.*, 2006) is 0.025 (1/mm), which is 0.03 (1/mm) in our device using the direct method and 0.0275 (1/mm) using the reciprocity theorem . The resolution value is 0.045 (1/mm) at the closest point to the sensors in Scharfetter device. In our device this value is 0.057 using

the direct method and 0.053 using the reciprocity theorem method (1/mm). At point [7.5,0,0] which is located in the middle distances from the sensors, our resolution is 0.0457 using direct method (1/mm) and 0.044 (1/mm) using reciprocity theorem method, while Scharfetter is 0.023 (1/mm). As expected, the uniform induction field has provided better resolution at some central regions of ROI.

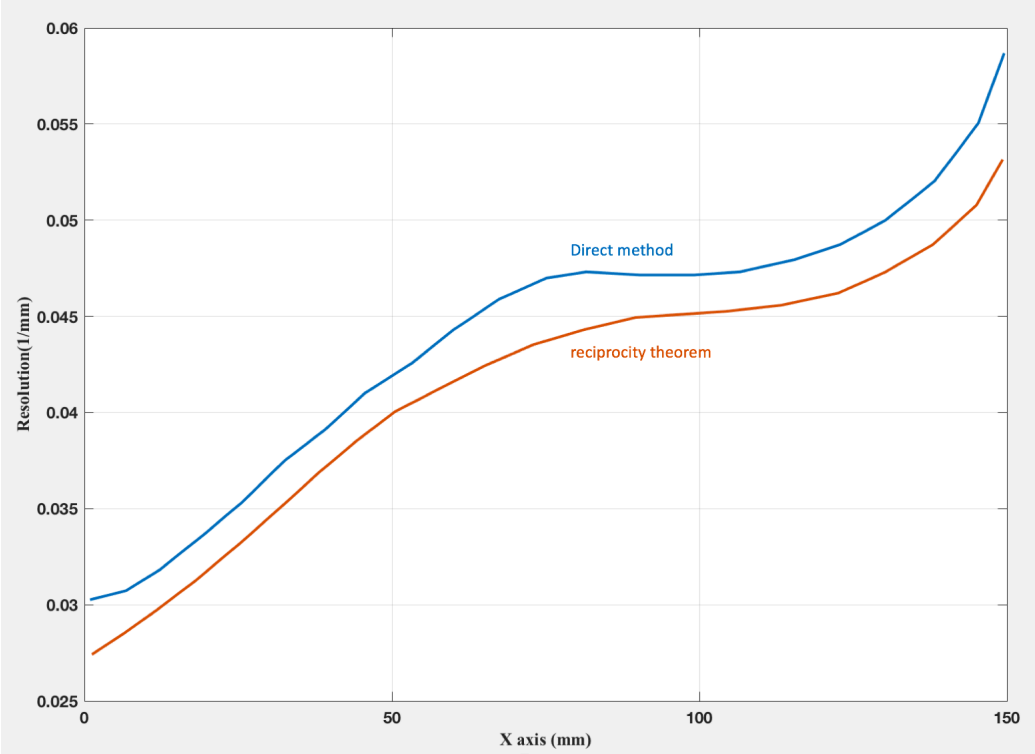

Figure 6.27 Resolution of the direct method and reciprocity theorem method calculated as a function of displacemnt in X direction.

It should also be noted that the device simulated by Scharfetter (Scharfetter *et al.*, 2006) has calculated the resolution for 4 different cases of SNR from noise free to 50 dB. The results presented in this dissertation has considered 40 dB SNR in all the calculations and the results taken for comparison from (Scharfetter *et al.*, 2006) were at 50 dB. In both cases, uncorrelated Gaussian noise was added to the data (provides a certain SNR) in order to simulate the noise of the receiver channels. This type of noise, although are commonly used in simulations of these kinds, is not completely true for real situation. In addition the noise of excitation coils is propagated to all of receiver coils, and result in certain amount of correlated noise in all the receiver channels. These kinds of correlated noise modeling needs more specifications

about the hardware used in the device. However we disregarded this fact in this simulation for simplicity at this stage. We considered one percent of the maximum signal as uncorrelated Gaussian noise which result in 40 dB of SNR. Other studies have also considered other noise in their model in MHz frequencies (Zolgharni *et al.*, 2009a) has resulted in a successful reconstruction. There is an agreement that MIT imaging that between 40 to 60 dB SNR is necessary for a successful reconstruction. However, the quality of such reconstruction depends on the regularization method which we tried to address by optimizing the regularization parameter.

The quality of the reconstruction also depends on accurate calculation of the sensitivity matrix which is the accuracy of the linear model. The reciprocity theorem in MIT provide a fast calculation method for calculation of the sensitivity, therefore is widely used in simulations. We showed a direct calculation method, even though considerably more time consuming can provide more accurate linear model. However, the calculation of the sensitivity for differential imaging only needs to be done once(one time training of the model).

The number of elements used for calculation is directly connected with the accuracy of the forward model, as more elements means more total number of eigenvectors to simulate a vector field in the ROI. This accuracy can also be increased by using higher order Whitney function such as second order Whitney functions which has 20 eigenvectors which are used in COMSOL simulators. However, as the goal was to calculate the sensitivity, avoiding more complex formulation to simulate the forward model is compensated with more number of elements.

This was not done only to simulate the forward problem. The sensitivity is the direct numerical derivative of the forward model and therefore its accuracy is dependent on the number of elements in the forward model. The model used for comparison of the results uses 80000 number of meshes.

The measurements made with our cylindrical MIT device demonstrate the feasibility of detection of the stroke in a simple disk model. However, within each tissue type in real head model, there are non-uniformities which will change the smoothness of the background. Moreover, non linear methods are not computationally efficient even in this simple model using the direct method of sensitivity calculation. Therefore, time difference imaging (after and before the lesion) where only the lesion itself is detected, is the only realistic application of the MIT device which uses the direct method for reconstruction. The use of various frequencies in order to define a frequency signature for the stroke and other head tissues is also be an advantages approach (Zolgharni *et al.*, 2009a).

CHAPTER 7 CONCLUSION AND FUTURE WORKS

7.1 Conclusion

A simulation tool has been developed to help designing a MIT device along with a methodology for improving the reconstruction result. We developed a general solution to the forward Helmholtz equation, considering both displacement and eddy current and implemented it in a numerical package using MATLAB to tackle the numerical calculations. For numerical calibration of the device, a new method of calculating the sensitivity matrix is introduced which improve the quality of the reconstructed image (less artifacts). We calculated the Jacobian matrix using the direct method by variation of the Helmholtz equation and reconstructed the conductivity map of the ROI using the calculated field at the sensors and applied it to investigate the possibility of monitoring the development of cerebral edema, an alteration in the conductivity of brain tissue.

Our device exhibits different location, size and orientation exciting coils and detectors as compared to most of the state of art MIT devices. A frequency of 50 kHz was chosen based on limitations from practical measurement constraints, so that capacitive crosstalk (electronics noise) would be smaller than the secondary magnetic field signal produced by the tissues. Moreover, another safety factor known as signal absorption rate (SAR) of biological tissue, makes lower frequencies better candidates for operation, as less energy and heat is transferred to the ROI. In fact, a preliminary analysis of SAR for the situation we have modelled shows that we could still increase the primary field excitation by a few hundreds, while keeping below the limit of 10 W/kg. However, the frequency should not be lowered to a value at which the secondary field signal is too weak to be detected, and therefore masked in the presence of the stronger background primary field.

The total number of independent measurement made with this device were 480 with 20% of the measurements above 20 m^0 in the case of the object at the center of ROI (worst case in terms of the phase difference values). Reconstruction of the lesion in this case tolerates less number of measurements (up to 40% of measurement less than 20 m^0 can be omitted) at the cost of a more blurry image.

The sensitivity analysis can be used in designing the detector configuration for improving the detection of the secondary signal. In our model, using the cylindrical symmetry, the sensors were arranged to receive minimum flux due to the primary signal. Therefore the sensors were placed perpendicular to the induction coil on the walls of the cylinder.

As an example, the detection of lesion within the head using a disk model has been investi-

gated, using the full Maxwell's equation for the forward problem approach and maximum a posteriori method along with Tikhonov regularization for the inverse problem. This investigation shows that the lesion produces the phase change of milli-degrees order of magnitude in this MIT device at the frequency of 50 kHz .

The amount detected signal is sufficient to confirm the presence of the lesion in three investigated locations. It was also demonstrated that the maximum detected phase change is dependent on the location of the lesion. The feasibility of the reconstruction from the detected signal is demonstrated in the presence of added Gaussian noise at the level of 1% of the maximum detected phase change. It will produce 40 dB SNR which is known to be achievable by GMI sensor with 100 μT field range and the noise level of 10 $\frac{pT}{\sqrt{Hz}}$.

The detection of the lesion in the disk model was confirmed for a large peripheral stroke of size 75 cm^3 for the conductivity contrast of 7 times at 50 kHz. Using an excitation current of 1 A (that is the number of turns in the coil times the excitation current), this perturbation perturbation caused signals between 2 to 25 pico-tesla as shown in Fig. (6.19) when it was located at the closest location to the sensors (position a). When the disk is shifted toward the center these fields fall between 8 to 13 pico-tesla as shown in Fig. (6.20). This signal is directly related to the exciting field, which can be increased by a factor of several hundreds before we reach the limit imposed by SAR, the volume of the perturbation as well as the conductivity contrast and the location of the implied perturbation. Therefore, answering questions such as what contrast size and volume can be reconstructed can only be answered in terms of a specific device. We have only investigated the feasibility of detection of a certain conductivity volume at a fixed frequency for three different locations of the ROI. Zolgharni (Zolgharni *et al.*, 2009a) have reported a successful reconstruction of a peripheral stroke of size 49 cm^3 at 10 MHz.

The absolute reconstructed values for the conductivity of the ROI using the detected magnetic field in this model were not the same as their true values (65% difference in the first iteration), due to the linear approximation. But it was demonstrated that the we can find the conductivity values more accurately, when non linear iterative inverse method were used. However, as the non linear method is not efficient computationally, the author believes that performing MIT, specifically with the direct sensitivity calculation method is not suitable for absolute detection of the conductivity values due to the computational cost.

Comparisons were made for two method of extraction the sensitivity matrix that is used for the image reconstruction. Results showed that the direct method produces images with higher resolution and less noise compared to that calculated with reciprocity theorem. However, the computational cost is higher for the direct method. As the calculation of the sensitivity matrix is done once for the specific configuration of an operating device, the method producing

more accurate results is advantages to the fastest method.
Real-time imaging is possible with the current MIT device, as each inverse problem takes around 10 seconds once the sensitivity is calculated and that can even be reduced by reduction in number of the measurements for a cross sectional image.
In a real model of the brain with a complex structure, there are challenges from the nonuniform conductivity of the background which will result in varying conductivity contrasts. This varying contrast will introduce extra noise in the conductivity reconstruction. Furthermore, MIT devices are very sensitive to the electronic noise and should be properly shielded to be functional.
For ischemic stroke treatment, the clot dissolving drug is effective if administered within three hours of the primary symptoms, but this can only be undertaken if a haemorrhagehas been definitely excluded. MIT offer a low-cost rapid imaging technique as an alternative to aid initial diagnose and provide continuous monitoring of the brain. This method can also be used for monitoring the lung ventilation (where EIT is now most being used) to provide a contactless measurements. Other biomedical applications can be proposed concerning tissue alterations which changes the passive electromagnetic properties.
Other than bio-medical prospective, this method provides us with a powerful tool for any kind of non-destructive testing involving materials with different electrical properties. For instance, this technique can be use in geology to study and detect fossils within the rock segments. However, the device should be tuned for the specific conductivity ranges to perform the best for its specific application.

7.2 Future Work

The model introduced here was developed as a first stage of designing a more complete MIT system, and used particularly to show the feasibility of differential MIT imaging of the lesion at 50 kHz. However, as structured mesh were used throughout the calculations, the model makes certain assumptions in terms of considering the head shape as a disk and its layers' properties are limited to skull and white matter. We did not consider the presence of the other biological tissues present in the head which could effect the measurement.
The first immediate step for further investigation of this subject is to use a real head mesh with different size and location of the lesion. After working with the proposed device and simulating various forward and inverse problem, the author believes that there might be certain advantages in using the excitation pattern introduced by (Tanguay *et al.*, 2007) which consists of 8 off axis excitation coils at each level (total of 48 excitation coils). In this excitation

pattern, the rows in sensitivity matrix were tested to be more independent from one another, which means the number of independent measurement can be increased in the cross section. The performance criteria suggested the integration of GMI sensors with the MIT device. Their small size allows for higher density of sensors around ROI without any cross-talk between these sensors, and therefore higher spatial resolution.

The effect of increasing the excitation current within the allowed SAR values should be investigated in our system to see if we can improve the system imaging performance by stronger primary field. However, this will need additional information on the electronic devices and the maximum current we can drive in a certain coil based on its size and resistance.

In order to provide investigate the optimal the sensor position and orientation, optimization algorithm are available to find the most influential sensors. There are criteria for checking the independence of the sensitivity matrix rows, which can be used to find the most efficient configuration of the sensors. The technique can be used for the sensitivity matrix calculated using the direct method to find the optimum configuration. With this optimization method, it is even possible to look at a specific place in ROI with more resolution using the weighed sensitivity concept. For an optimum practical device, sensitivity analysis provides valuable information which can be integrated in the design process.

The MAP method used for the inverse problem is among the most applied method for EIT and MIT for imaging materials of low conductivity. However, there are several regularization method that are commonly used along with MAP which are potentially capable of providing better images. The inverse problem should be solved using various regularization method and then the best method for our specific device can be picked. In literature, inverse problems of MIT devices has been solved using different regularization method (Scharfetter *et al.*, 2006) and comparison have been made for a specific device. However, the performance of the method is affected by the device properties and the results can not be generalized to other devices and should be investigated on the same system.

Overall, the system can still be subjected to various improvement for building a practical device capable of this specific application in MIT.

Postlude

The scientist has a lot of experience with ignorance and doubt and uncertainty, and this experience is of very great importance, I think. When a scientist doesn't know the answer to a problem, he is ignorant. When he has a hunch as to what the result is, he is uncertain. And when he is pretty damn sure of what the result is going to be, he is still in some doubt. We have found it of paramount importance that in order to progress, we must recognize our ignorance and leave room for doubt. Scientific knowledge is a body of statements of varying degrees of certainty some most unsure, some nearly sure, but none absolutely certain. Now, we scientists are used to this, and we take it for granted that it is perfectly consistent to be unsure, that it is possible to live and not know. But I don't know whether everyone realizes this is true. Our freedom to doubt was born out of a struggle against authority in the early days of science. It was a very deep and strong struggle : permit us to question to doubt to not be sure. I think that it is important that we do not forget this struggle and thus perhaps lose what we have gained.

Richard P. Feynman

REFERENCES

ADLER, A. et GUARDO, R. (1996). Electrical impedance tomography : regularized imaging and contrast detection. *IEEE transactions on medical imaging*, 15, 170–179.

ADLER, A., SHINOZUKA, N., BERTHIAUME, Y., GUARDO, R. et BATES, J. H. (1998). Electrical impedance tomography can monitor dynamic hyperinflation in dogs. *Journal of Applied Physiology*, 84, 726–732.

AGHASI, A. et MILLER, E. L. (2012). Sensitivity calculations for poisson's equation via the adjoint field method. *IEEE Geoscience and Remote Sensing Letters*, 9, 237–241.

AHLBOM, A., BERGQVIST, U., BERNHARDT, J., CESARINI, J., GRANDOLFO, M., HIETANEN, M., MCKINLAY, A., REPACHOLI, M., SLINEY, D. H., STOLWIJK, J. *ET AL.* (1998). Guidelines for limiting exposure to time-varying electric, magnetic, and electromagnetic fields (up to 300 ghz). *Health physics*, 74, 494–521.

BORCEA, L. (2002). Electrical impedance tomography. *Inverse problems*, 18, R99.

BORGES, A., DE OLIVEIRA, J., VELEZ, J., TAVARES, C., LINHARES, F. et PEYTON, A. (1999). Development of electromagnetic tomography (emt) for industrial applications. part 2 : Image reconstruction and software framework. *Proc. 1st World Congr. Industrial Process Tomography*. 219–225.

BROWN, B. (2009). Electrical impedance tomography (eit) : a review. *Journal of medical engineering & technology*.

CASANOVA, R., SILVA, A. et BORGES, A. (2004). Mit image reconstruction based on edge-preserving regularization. *Physiological measurement*, 25, 195.

CORSON, D. R. et LORRAIN, P. (1962). *Introduction to electromagnetic fields and waves*. San Francisco : WH Freeman.

COULOMBE, N., GAGNON, H., MARQUIS, F., SKROBIK, Y. et GUARDO, R. (2005). A parametric model of the relationship between eit and total lung volume. *Physiological measurement*, 26, 401.

DUFAY, B., SAEZ, S., DOLABDJIAN, C., YELON, A. et MÉNARD, D. (2013a). Development of a high sensitivity giant magneto-impedance magnetometer : Comparison with a commercial flux-gate. *IEEE Transactions on magnetics*, 49, 85–88.

DUFAY, B., SAEZ, S., DOLABDJIAN, C., YELON, A. et MÉNARD, D. (2013b). Development of a high sensitivity giant magneto-impedance magnetometer : comparison with a commercial flux-gate. *Magnetics, IEEE Transactions on*, 49, 85–88.

GABRIEL, C., GABRIEL, S. et CORTHOUT, E. (1996a). The dielectric properties of biological tissues : I. literature survey phys. *Physics in medicine and biology*, 41, 2231.

GABRIEL, S., LAU, R. et GABRIEL, C. (1996b). The dielectric properties of biological tissues : Ii. measurements in the frequency range 10 hz to 20 ghz. *Physics in medicine and biology*, 41, 2251.

GABRIEL, S., LAU, R. et GABRIEL, C. (1996c). The dielectric properties of biological tissues : Iii. parametric models for the dielectric spectrum of tissues. *Physics in medicine and biology*, 41, 2271.

GENCER, N. G. et TEK, M. N. (1999). Electrical conductivity imaging via contactless measurements. *Medical Imaging, IEEE Transactions on*, 18, 617–627.

GENÇER, N. G. et TEK, M. N. (2000). Imaging tissue conductivity via contactless measurements : a feasibility study. *TURKISH JOURNAL OF ELECTRICAL ENGINEERING & COMPUTER SCIENCES*, 6, 183–200.

GESELOWITZ, D. B. (1971). An application of electrocardiographic lead theory to impedance plethysmography. *IEEE Transactions on biomedical Engineering*, 38–41.

GÓMEZ-LABERGE, C. et ADLER, A. (2007). Direct calculation of the electrode movement jacobian for 3d eit. *13th International Conference on Electrical Bioimpedance and the 8th Conference on Electrical Impedance Tomography*. Springer, 364–367.

GRIFFITHS, D. J. (1999). Electrodynamics. *Introduction to Electrodynamics, 3rd ed., Prentice Hall, Upper Saddle River, New Jersey*, 301–306.

GRIFFITHS, H. (2001). Magnetic induction tomography. *Measurement science and technology*, 12, 1126.

GRIFFITHS, H., STEWART, W. et GOUGH, W. (1999). Magnetic induction tomography : a measuring system for biological tissues. *Annals Of The New York Academy Of Sciences*, 873, 335–345.

GUARDO, R. (2013). *Design and characterization of a signal conditioning module for GMI-based magnetic field sensor.* Internal report.

GURSOY, D. et SCHARFETTER, H. (2009). Optimum receiver array design for magnetic induction tomography. *IEEE Transactions on Biomedical Engineering*, 56, 1435–1441.

HAIRER, E., NRSETT, S. P. et WANNER, G. (2010). *Solving Ordinary Differential Equations : Nonstiff problems. v. 2 : Stiff and differential-algebraic problems*. Springer Verlag.

HOLDER, D. (1992). Detection of cerebral ischaemia in the anaesthetised rat by impedance measurement with scalp electrodes : implications for non-invasive imaging of stroke

by electrical impedance tomography. *Clinical Physics and Physiological Measurement*, 13, 63.

HOLDER, D. S. (2004). *Electrical impedance tomography : methods, history and applications*. CRC Press.

HOLLAUS, K., MAGELE, C., MERWA, R. et SCHARFETTER, H. (2004a). Fast calculation of the sensitivity matrix in magnetic induction tomography by tetrahedral edge finite elements and the reciprocity theorem. *Physiological measurement*, 25, 159.

HOLLAUS, K., MAGELE, C., MERWA, R. et SCHARFETTER, H. (2004b). Numerical simulation of the eddy current problem in magnetic induction tomography for biomedical applications by edge elements. *Magnetics, IEEE Transactions on*, 40, 623–626.

HORESH, L., GILAD, O., ROMSAUEROVA, A., MCEWAN, A., ARRIDGE, S. et HOLDER, D. (2005). Stroke type differentiation by multi-frequency electrical impedance tomographya feasibility study. *Proc IFMBE*, 11.

IGNEY, C., WATSON, S., WILLIAMS, R., GRIFFITHS, H. et DÖSSEL, O. (2005). Design and performance of a planar-array mit system with normal sensor alignment. *Physiological measurement*, 26, S263.

KABANIKHIN, S. I. (2008). Definitions and examples of inverse and ill-posed problems. *Journal of Inverse and Ill-Posed Problems*, 16, 317–357.

KOBYLIANSKII, J., MURRAY, A., BRACE, D., GOLIGHER, E. et FAN, E. (2016). Electrical impedance tomography in adult patients undergoing mechanical ventilation : A systematic review. *Journal of Critical Care*, 35, 33–50.

KORJENEVSKY, A., CHEREPENIN, V. et SAPETSKY, S. (2000). Magnetic induction tomography : experimental realization. *Physiological Measurement*, 21, 89.

LIU, A. K., DALE, A. M. et BELLIVEAU, J. W. (2002). Monte carlo simulation studies of eeg and meg localization accuracy. *Human brain mapping*, 16, 47–62.

MERWA, R., HOLLAUS, K., BIRÓ, O. et SCHARFETTER, H. (2004). Detection of brain oedema using magnetic induction tomography : a feasibility study of the likely sensitivity and detectability. *Physiological measurement*, 25, 347.

MERWA, R. et SCHARFETTER, H. (2008). Magnetic induction tomography : comparison of the image quality using different types of receivers. *Physiological measurement*, 29, S417.

MORTARELLI, J. R. (1980). A generalization of the geselowitz relationship useful in impedance plethysmographic field calculations. *IEEE Transactions on Biomedical Engineering*, 11, 665–667.

OSTERMANN, A. (2005). Sensitivity analysis. *Analyzing Uncertainty in Civil Engineering*, Springer. 101–114.

PEYTON, A., YU, Z., LYON, G., AL-ZEIBAK, S., FERREIRA, J., VELEZ, J., LINHARES, F., BORGES, A., XIONG, H., SAUNDERS, N. *ET AL.* (1996). An overview of electromagnetic inductance tomography : description of three different systems. *Measurement Science and Technology*, 7, 261.

POLYDORIDES, N. et LIONHEART, W. (2003). Adjoint formulations in impedance imaging. *Proc. 3rd World Congress on Industrial Process Tomography, The Rockies, Alberta, Canada Tuesday 2nd-Friday 5th September*. Citeseer, p689–694.

REDDY, C., DESHPANDE, M. D., COCKRELL, C. et BECK, F. B. (1994). Finite element method for eigenvalue problems in electromagnetics.

ROSELL-FERRER, J., MERWA, R., BRUNNER, P. et SCHARFETTER, H. (2006). A multifrequency magnetic induction tomography system using planar gradiometers : data collection and calibration. *Physiological Measurement*, 27, S271.

SCHARFETTER, H., HOLLAUS, K., ROSELL-FERRER, J. et MERWA, R. (2006). Single-step 3-d image reconstruction in magnetic induction tomography : theoretical limits of spatial resolution and contrast to noise ratio. *Annals of biomedical engineering*, 34, 1786–1798.

SCHARFETTER, H., KÖSTINGER, A. et ISSA, S. (2008). Hardware for quasi-single-shot multifrequency magnetic induction tomography (mit) : the graz mk2 system. *Physiological measurement*, 29, S431.

SCHARFETTER, H., LACKNER, H. K. et ROSELL, J. (2001). Magnetic induction tomography : hardware for multi-frequency measurements in biological tissues. *Physiological Measurement*, 22, 131.

SOLEIMANI, M. et LIONHEART, W. R. (2006). Absolute conductivity reconstruction in magnetic induction tomography using a nonlinear method. *Medical Imaging, IEEE Transactions on*, 25, 1521–1530.

SOMERSALO, E., ISAACSON, D. et CHENEY, M. (1992). A linearized inverse boundary value problem for maxwell's equations. *Journal of computational and applied mathematics*, 42, 123–136.

STANLEY, L. G. et STEWART, D. L. (2002). *Design sensitivity analysis : computational issues of sensitivity equation methods*, vol. 25. SIAM.

TANGUAY, L.-F., GAGNON, H. et GUARDO, R. (2007). Comparison of applied and induced current electrical impedance tomography. *Biomedical Engineering, IEEE Transactions on*, 54, 1643–1649.

VAUHKONEN, M., HAMSCH, M. et IGNEY, C. (2008). A measurement system and image reconstruction in magnetic induction tomography. *Physiological measurement*, 29, S445.

WATSON, S., IGNEY, C., DÖSSEL, O., WILLIAMS, R. et GRIFFITHS, H. (2005). A comparison of sensors for minimizing the primary signal in planar-array magnetic induction tomography. *Physiological measurement*, 26, S319.

WATSON, S., MORRIS, A., WILLIAMS, R., GRIFFITHS, H. et GOUGH, W. (2004). A primary field compensation scheme for planar array magnetic induction tomography. *Physiological measurement*, 25, 271.

WATSON, S., WILLIAMS, R., GOUGH, W. et GRIFFITHS, H. (2008). A magnetic induction tomography system for samples with conductivities below 10 s m- 1. *Measurement Science and Technology*, 19, 045501.

WEI, H.-Y., MA, L. et SOLEIMANI, M. (2012). Volumetric magnetic induction tomography. *Measurement Science and Technology*, 23, 055401.

YANG, W. et PENG, L. (2002). Image reconstruction algorithms for electrical capacitance tomography. *Measurement Science and Technology*, 14, R1.

ZOLGHARNI, M., GRIFFITHS, H. et LEDGER, P. (2010). Frequency-difference mit imaging of cerebral haemorrhage with a hemispherical coil array : numerical modelling. *Physiological measurement*, 31, S111.

ZOLGHARNI, M., LEDGER, P., ARMITAGE, D., HOLDER, D. et GRIFFITHS, H. (2009a). Imaging cerebral haemorrhage with magnetic induction tomography : numerical modelling. *Physiological measurement*, 30, S187.

ZOLGHARNI, M., LEDGER, P. et GRIFFITHS, H. (2009b). Forward modelling of magnetic induction tomography : a sensitivity study for detecting haemorrhagic cerebral stroke. *Medical & biological engineering & computing*, 47, 1301–1313.

APPENDIX A Resolution criteria

The main idea of EIT or MIT is relatively simple and is depicted in Fig.(A.1). Consider a two dimensional conductive plane with unknown conductance values of its' surface. One way to find a conductivity map of such plane is to apply a current between two different nodes (points on the edge) and measurement of the voltage at the two other different locations. We need a certain number of measurements in order to map the conductance of the surface for a desired resolution. As it can be seen in Fig.(A.1), the problem equivalently can be modeled as series of parallel and orthogonal resistors, with unknown and unequal resistances, that map the whole surface.

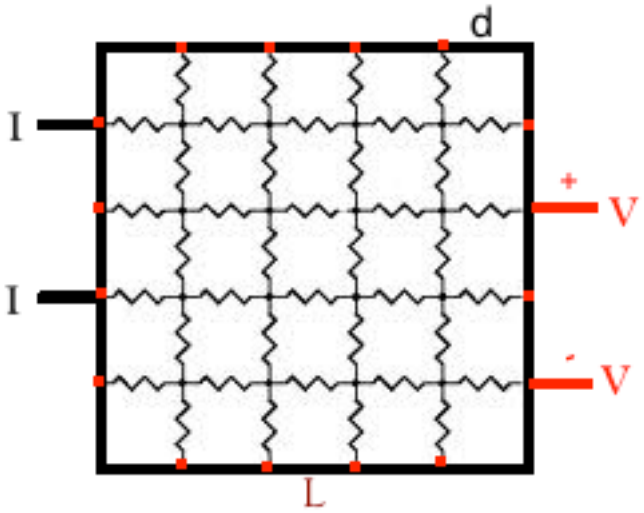

Figure A.1 Modelling the conductivity of a surface with a series of resistors

The current is applied on different locations around the perimeter and the voltage is measured at different sites for the applied current. Increasing the number of nodes will increase the number of independent measurements (different nodes' combination leads to independent measurements) and therefore the resolution is increased.
In this example, we can say as the number of resistors increases, in other words, as the number of white squares go up, we are going higher in the resolution. This implies that for a conducting surface, the number of measurements uniquely determines the resolution in the case of ideal measurements. In Fig.(A.1), if we switch the connections, which is to apply the current from red labeled lines and measure the voltage from the black labeled lines, the

measurement is not an independent measurement. This reduces the number of independent measurements by a factor of 2 for all the possible four point measurement permutations.
Quantitatively speaking, for a square of side L, and spacing d between the nodes, there exist $2\frac{L}{d}(\frac{L}{d}-1)$ numbers of resistors which map the surface and $4\frac{L}{d}$ numbers of nodes which will result in $\frac{1}{2}\frac{(\frac{4L}{d})!}{4!\times(\frac{4L}{d}-4)!}$ numbers of independent measurements.
As shown by (Tanguay *et al.*, 2007), more than 100 measurements is required to obtain desired resolution in 2D. For example a 2D medium discretize into 10×10 pixels, we will need at least 100 linearly independent measurements to obtain a solution. With 10×10 pixels the spatial resolution is around 10 % of the object's diameter.
In MIT measurements, we need a combination of coils for inducing eddy currents in the body tissues (similar to the applied current) and magnetic field sensors for recording their responses (similar to the voltage pick ups). In the case of N inducting coils and M pick up coils, $\frac{N\times M}{2}$ independent measurements could be made (The factor of 2 appears for the same reason). However, in practice, theoretically independent measurements might be not completely independent in practice as they might produce almost the same sets of equations. This is a result of the amount of symmetry in the ROI. Our simulations have suggested that the less symmetrical the induction method is, the more number of practically independent measurements result in (See Chapter (6)).

APPENDIX B Point spread function

The point spread function (PSF) is calculated by mapping the true parameter (conductivity) value $\boldsymbol{\sigma}^*$ to the reconstructed ones $\boldsymbol{\sigma}$ using the reconstruction equation (Scharfetter *et al.*, 2006) :

$$\Delta \mathbf{B} = \mathbf{S}_\sigma \Delta \boldsymbol{\sigma}^* \tag{B.1}$$

Eq. (B.1) is the linear model of the forward problem. In the inverse problem we use the calculated $\Delta \mathbf{B}$ and multiply it by the pseudo inverse of the sensitivity matrix $\mathbf{S}_{inv}$ to get the reconstructed conductivity using following equation :

$$\Delta \boldsymbol{\sigma} = \mathbf{S}_{inv} \Delta \mathbf{B} = \mathbf{S}_{inv} \mathbf{S}_\sigma \Delta \boldsymbol{\sigma}^* = \mathbf{M} \Delta \boldsymbol{\sigma}^* \tag{B.2}$$

and $\mathbf{S}_{inv}$ is given by

$$\mathbf{S}_{inv} = ((\mathbf{S}_\sigma^T \Gamma_n^{-1} \mathbf{S}_\sigma + \Gamma_\gamma^{-1}))^{-1} \mathbf{S}_\sigma^T \Gamma_n^{-1} \tag{B.3}$$

Where Γ_N is the variance of added noise and Γ_γ is the variance of conductivity. The matrix $\mathbf{M}$ is the multiplication of the inverse and the pseudo inverse.
Considering the following equation which is the last step made in Eq.(B.2)

$$\Delta \boldsymbol{\sigma} = \mathbf{M} \Delta \boldsymbol{\sigma}^* \tag{B.4}$$

If we assume $\mathbf{M}$ as the identity matrix, which is ideal result of multiplication of a matrix and its inverse, we should get the same values of actual and reconstructed conductivity. However, $\mathbf{M}$ deviate from the identity in the case $\mathbf{S}_{inv}$ $\mathbf{S}_\sigma$ and this deviation shows smearing of the available information (conductivity of a voxel) over the imaging plane and provides the typical diffuse images in MIT. The ith column of M is then the shifted PSF for the ith voxel (Liu *et al.*, 2002).